Quantitative Analysis of Inelastic Scattering in Two-Crystal and Three-Crystal Neutron Spectrometry; Critical Scattering from RbMnF$_3$ †

A. Tucciarone, H. Y. Lau,* L. M. Corliss, A. Delapalme, ‡ and J. M. Hastings

Chemistry Department, Brookhaven National Laboratory, Upton, New York 11973

(Received 17 May 1971)

The use of the neutron spectrometer in the quantitative determination of neutron scattering cross sections is discussed in detail. The explicit analytical dependence of the total detection efficiency of the three-crystal spectrometer on incident and scattered neutron energies as well as on instrumental parameters is presented, and measurement of the energy sensitivity of the analyzer-detector system is described. A comprehensive treatment of two-crystal inelastic scattering is given, and a practical method is developed for carrying out the inelastic analysis of two-crystal data using the experimental *elastic* resolution function. The quasielastic approximation is discussed, several mechanisms which extend its range of validity are described, and its applicability is shown to depend on a parameter which is a dimensionless combination of the variables in the problem. These techniques are applied to the measurement of the spin-pair correlation function, in the neighborhood of the critical point, for the ideal Heisenberg antiferromagnet RbMnF$_3$. The predictions of dynamic-scaling theory, recently proposed by Halperin and Hohenberg, are extensively tested and find strong support in experiment. The energy widths of the scattering, measured in the region $T \geq T_N$, are compared with theoretical calculations for the Heisenberg antiferromagnet by Résibois and Piette and by Huber and Krueger. The measurement, by means of the two-crystal diffractometer, of the static correlation function at the critical point is discussed in detail, and direct evidence is presented for departure from the classical Ornstein-Zernike behavior. The parameter η, which measures this departure, is determined by means of three independent experiments and, after the inelasticity of the scattering is taken into full account, is found to be 0.055 ± 0.010. Measurement of the critical indices above T_N gives $\gamma = 1.366 \pm 0.024$ and $\nu = 0.701 \pm 0.011$, and the static scaling relation $\gamma = (2 - \eta)\nu$ is verified. Below T_N, we find $\beta = 0.32 \pm 0.02$ and $\nu' = 0.54 \pm 0.03$; these values are consistent with the static scaling relation $2\beta = (1 + \eta)\nu'$, whereas the symmetry relation $\nu = \nu'$ is violated.

OUTLINE

I. INTRODUCTION

The magnetic scattering of neutrons as a function of energy and momentum transfer determines, in principle, the complete space-time spin pair-correlation function, from which, in turn, all intrinsic magnetic properties can be obtained. While it is difficult to carry out this determination directly, one can fit the observed scattering to theoretical or empirical forms for the correlation function and, by evaluating the associated parameters, obtain a detailed description of static and dynamic properties. Even this simpler procedure is far from straightforward, inasmuch as sizable corrections for instrumental resolution and energy sensitivity are often required. We discuss these corrections in detail and indicate how, building on earlier work of Cooper and Nathans,[1] they can be applied in *quantitative* fashion. Spatial correlations, which are ordinarily obtained from two-crystal experiments by invoking the quasielastic approximation, may be seriously in error because of the inelasticity of the scattering. In view of the importance of the two-crystal method, we have carried out a comprehensive analysis of the quasielastic approximation and have obtained estimates of the corrections involved.

We have used both two- and three-crystal techniques to study spin correlations in rubidium manganese fluoride $RbMnF_3$ in the vicinity of its magnetic critical point. This compound is an ideal magnetic system in many respects. It is simple cubic in the paramagnetic phase and undergoes an antiferromagnetic transition at 83 °K in which the unit cell is doubled ($a_0 = 8.453$ at 83 °K) and the spins order by alternating in sign along each cube edge, as shown by Pickart, Alperin, and Nathans.[2] The x-ray studies by Teaney, Moruzzi, and Argyle[3] indicate essentially no detectable departure from cubic symmetry in passing through the Néel point. Windsor and Stevenson[4] have demonstrated that $RbMnF_3$ is well described by an isotropic, nearest-neighbor Heisenberg Hamiltonian. Their spin-wave dispersion measurements indicate a nearest-neighbor exchange constant of 0.29 ± 0.03 meV, a second-neighbor constant of less than 0.02 meV, and very little anisotropy. The antiferromagnetic resonance experiments of Teaney, Freiser, and Stevenson[5] indicate, in fact, that the magnetic anisotropy is only 4.5 G. Critical scattering from $RbMnF_3$ was first investigated by Nathans, Menzinger, and Pickart,[6] who reported the existence of magnonlike excitations above the Néel point and, using high-resolution techniques, observed the critical slowing down of spin fluctuations that had been predicted by Van Hove and previously reported for terbium by Als-Nielsen, Dietrich, Marshall, and Lindgård.[7] This slowing down in the neighbor-

hood of the critical point had not been found previously since, as Marshall[8] pointed out in discussing the earlier measurements, the experiments were performed with relatively low resolution and were thus insensitive to the long-range fluctuations, whose detection requires small wave-vector transfer. Preliminary accounts[9] of some aspects of the present work have also been published. We note that some of the previously quoted numerical values have been recomputed on the basis of more complete analyses of inelasticity corrections and of experimental errors.

The many similarities exhibited by dissimilar physical systems undergoing second-order phase transitions have led to a search for general principles underlying all such transitions. One such idea is that of scaling, which has been generalized recently by Halperin and Hohenberg[10] to include dynamic as well as static phenomena. The central concept here is that the behavior of the space-time correlation function is determined essentially by the ratio of the wavelength of the spin fluctuations to a *single* range parameter characteristic of the system. We have tested the theory of dynamic scaling by measurement of the energy and momentum dependence of the critical scattering from $RbMnF_3$. Our results strongly support the concept of dynamic scaling and confirm specific predictions of the theory. We have obtained analytical expressions for the full correlation function at the Néel point, and for the characteristic frequencies, or energy widths of the scattering, above the transition. These frequencies are in good agreement with those calculated for the Heisenberg antiferromagnet by Résibois and Piette[11] and by Huber and Krueger.[12]

Critical indices γ and ν, describing the limiting behavior of the susceptibility and range parameter respectively for $T > T_N$, have been obtained from our two-crystal experiments after applying the necessary corrections for inelasticity. The data have been analyzed in terms of the simple Fisher and Burford[13] approximant for the scattering and direct measurements have been made of the parameter η, giving the departure from Ornstein-Zernike behavior. The static scaling relationship $\gamma = (2 - \eta)\nu$ is well obeyed, but ν is found to differ significantly from the corresponding index ν' determined from inelastic measurements below T_N. The indices γ and ν agree well with those obtained by Jasnow and Wortis[14] for the Heisenberg antiferromagnet by high-temperature series expansions.

The plan of the paper is as follows: In Sec. II, we give cross sections and a general description of the experimental arrangements for the two- and three-crystal experiments. In Sec. III, the measurement and use of the two-crystal elastic resolution function is discussed. Experimental determi-

nation of mosaic spread and collimation parameters is described. In Sec. IV, we give the results of two-crystal measurements. Use of the simple Fisher-Burford approximant for the scattering is justified and several independent determinations of η are described. Values of the inverse range parameter κ as a function of temperature, as well as the critical indices ν, γ, and β are presented and certain static scaling relations are tested. Section V treats the determination of the three-crystal resolution function from measured instrumental parameters and its use in quantitative intensity calculations. Detailed analytical expressions are presented for the dependence of the total detection efficiency on incident and scattered neutron energies and on instrumental parameters. Measurement of the energy sensitivity of the analyzer-detector system is described. In Sec. VI, the results of three-crystal measurements are presented within the context of dynamic-scaling theory. The correlation function is described in the "critical" region, where momentum transfers q are large compared to κ, and in the "hydrodynamic" region above T_N where $q \ll \kappa$. An analytic expression for the characteristic frequency is given for general values of q and κ. These measurements are discussed in relation to dynamic scaling and to calculations for the Heisenberg model. A determination of the critical index ν' from inelastic measurements in the hydrodynamic region below T_N is described in this section. In Sec. VII, we present a comprehensive analysis of the quasielastic approximation and discuss several general mechanisms which extend its range of usefulness. Corrections arising from inelasticity are evaluated for κ and ν and a method is proposed for determining ν with minimal error from this source. Corrections are discussed for the case of finite resolution and a practical method is developed for carrying out the inelastic analysis of two-crystal data using the experimental *elastic* resolution function. This method is applied to an independent determination of η. In the Appendix, we derive the two-crystal resolution function for the case of *inelastic* scattering and discuss its use in determining "constant-angle" cross sections.

II. CROSS SECTIONS AND EXPERIMENTAL ARRANGEMENT

The scattering of neutrons from a magnetic crystal is closely related to the spin-correlation function. Assuming that, over the crystal as a whole, the spin directions are randomly distributed, the "diffuse" cross section for the case of exchange coupling only, is given by

$$\frac{d^2\sigma}{d\Omega\, dE_f} \propto \frac{k_f}{k_i} \left| f(\vec{Q}) \right|^2 \sum_{\vec{r}} \int_{-\infty}^{\infty} dt\, e^{i(\vec{Q}\cdot\vec{r}-\omega t)} \langle \delta\vec{S}_0(0)\cdot\delta\vec{S}_{\vec{r}}(t)\rangle .$$

$$(2.1)$$

Here $\hbar\vec{Q}=\hbar\vec{k}_i-\hbar\vec{k}_f$ is the neutron momentum change; $f(\vec{Q})$ is the neutron scattering form factor; $\hbar\omega = E_i - E_f$ is the neutron energy loss; $\delta\vec{S}_{\vec{r}}(t)=\vec{S}_{\vec{r}}(t)-\langle\vec{S}_{\vec{r}}\rangle$ is the deviation of a spin from its average value, and $\langle\delta\vec{S}_0(0)\cdot\delta\vec{S}_{\vec{r}}(t)\rangle$ gives the correlation of the spin deviation at position $\vec{r}$ and time t with that at the origin at $t=0$. With a suitable experimental arrangement, the scattering corresponding to a given change of neutron momentum $\hbar\vec{Q}$ and energy $\hbar\omega$ measures the (Q, ω) component of the space-time Fourier transform of the correlation function. The experimental results reported here for inelastic scattering were obtained using a three-crystal neutron spectrometer in the "constant-$\vec{Q}$" mode. Such an instrument is shown schematically in Fig. 1. In operation, a neutron beam from the reactor is monochromatized by reflection from a germanium crystal M scattered from the sample crystal S and reflected by a germanium analyzing crystal A into a BF$_3$ detector.

The total scattering in a given direction, regardless of energy transfer, is a quantity that can be relatively easily obtained experimentally by replacing the analyzing crystal of Fig. 1 by a detector. The cross section for this so-called two-crystal case is given by the line integral of Eq. (2.1) with respect to energy, along the path of the scattered beam. It is to be noted that $\vec{Q}$ (and therefore $\vec{k}_f$) is not constant along the path, but rather a function of the energy transfer $\hbar\omega$. For $\hbar\omega$ sufficiently small compared to the incident energy E_i, deviations from the elastic values can be ignored and the constant-angle experiment is equivalent to one at
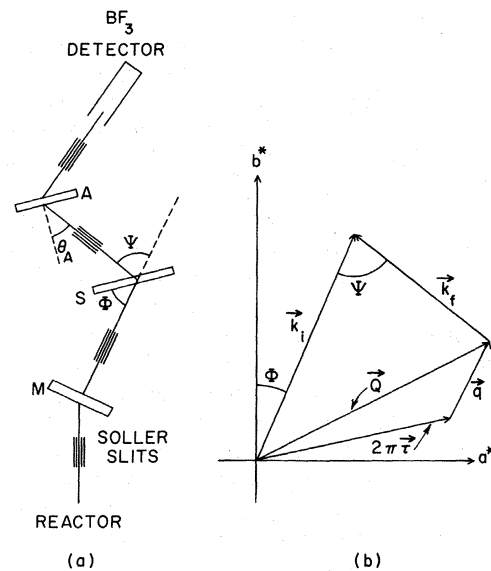

FIG. 1. (a) Schematic representation of the three-crystal spectrometer. (b) Vector diagram of the scattering process in reciprocal space.

constant $\vec{Q}$. Equation (2.1) can then be integrated over energy to give

$$\frac{d\sigma}{d\Omega} \propto |f(\vec{Q})|^2 \sum_{\vec{r}} e^{i\vec{Q}\cdot\vec{r}} \langle \delta\vec{S}_0(0) \cdot \delta\vec{S}_{\vec{r}}(0) \rangle,$$

relating the scattering at fixed angle to the static spin-correlation function. For $\hbar\omega \ll kT$, this expression can be shown[8] to reduce to the "quasielastic" cross section

$$\frac{d\sigma}{d\Omega} \propto |f(\vec{Q})|^2 \, T \, \chi(\vec{Q}), \tag{2.2}$$

where $\chi(\vec{Q})$ is the wavelength-dependent susceptibility.

In the three-crystal experiments, the collimators shown in Fig. 1 were of the Soller type with a nominal horizontal divergence, given by the ratio of the distance between vertical septa to the length of the collimator, of approximately 20 min of arc. No vertical collimation was used other than that provided by the 2-in. vertical opening of the slit system and the 3.5 in. diam of the reactor beam tube which extended approximately 9 ft beyond the in-Pile collimator. The monochromator and analyzer were germanium crystals cut parallel to (110) and reflecting from (111) in transmission geometry. They had been plastically deformed[15] to give rocking curves with a "full width at half-maximum" of ~ 12 min. The incident beam intensity was monitored by a fission counter. Angular settings were made to an accuracy of $0.01°$ using optical encoders controlled by an on-line computer.[16] Measurements were made at approximately 6.6, 13.0, and 47.0 meV, the last being close to the maximum of the Pile spectrum. The lower energies are subject to severe contamination by higher-order neutrons, particularly those of third order, since the second order is eliminated by the vanishing of the (222) structure factor in germanium. Higher-order neutrons were removed by a filter consisting of a 2-in. block of oriented pyrolytic graphite inserted into the beam before the sample.[17] At the lowest incoming energy, the response of the analyzer as a function of energy change in the sample was found to be appreciably distorted by additional Bragg scattering from reciprocal lattice points which are simultaneously present on the sphere of reflection. A decrease in scattering by the analyzer is in fact expected at an energy for which such simultaneous Bragg scattering can occur since these neutrons do not enter the counter. To minimize this effect, the analyzing crystal was rotated about its scattering vector so that simultaneous Bragg scattering occurred only for energy changes that were larger than about 7 meV.

To achieve horizontal resolution in the two-crystal experiment that is as good as that obtainable with a three-crystal spectrometer, it turns out to

be necessary to decrease the horizontal collimator divergences. The increased intensity available in the two-crystal experiment makes this feasible and also permits an improvement in the vertical resolution. Thus, in the two-crystal case, the following arrangement was used: 10-min horizontal collimation in the in-Pile region, 10-min vertical collimation between the monochromator and the sample, and 10-min horizontal and 10-min vertical collimation in front of the counter. The germanium monochromator in this case had a rocking-curve width of 6 min and all measurements were carried out at an incident energy of approximately 48 meV ($\lambda \simeq 1.3$ Å).

The single crystal of $RbMnF_3$, approximately 4 cm^3 in volume, was grown from the melt by Linz.[18] The full width at half-maximum of the rocking curve was 4 min, with some additional mosaic structure in the wings. The crystal was mounted with a $\langle 1\bar{1}0 \rangle$ axis vertical. Both the two- and three-crystal measurements were made in the vicinity of the (111) magnetic reflection. The sample was contained in a sealed aluminum can filled with helium exchange gas. A platinum resistance thermometer was placed inside a hole drilled into the bottom wall of the aluminum container. A resistance heater was attached to the bottom surface of the can. This assembly was connected by a suitably adjusted thermal resistance to a large copper block tail-piece of a variable temperature Dewar. The temperature of the copper block was regulated to $\pm 0.2°$K. The sample assembly, in turn, was regulated by means of an ac resistance bridge[19] and the platinum resistance thermometer to $\pm 0.005°$K.

III. TWO-CRYSTAL ELASTIC RESOLUTION FUNCTION

In the conventional elastic two-crystal measurement[20] the intensity of scattering is given by the convolution of the cross section with an effective resolution function $R_e(\vec{q} - \vec{q}_o)$, where $\vec{q}$ is a vector drawn from $2\pi\vec{\tau}$, a reference reciprocal lattice point, to a general point in reciprocal space and $\vec{q}_o$ extends from $2\pi\vec{\tau}$ to the center of the resolution function (see Fig. 2). R_e is itself a convolution of the true instrumental resolution function with the mosaic distribution of the sample. For a nominal instrumental setting corresponding to a displacement $\vec{q}_o$ from the reciprocal lattice point, and a cross section $(d\sigma/d\Omega)\,(\vec{q})$, the intensity is thus

$$I(\vec{q}_o) = \int \frac{d\sigma}{d\Omega} \, (\vec{q}) \, R_e(\vec{q} - \vec{q}_o) d\vec{q} \,. \tag{3.1}$$

R_e can be obtained experimentally in the usual way using the magnetic Bragg reflection as a probe. It is important to observe that the resolution function obtained in this way is entirely elastic and not necessarily appropriate to an experiment which integrates over energy. It will be shown in the Appen-
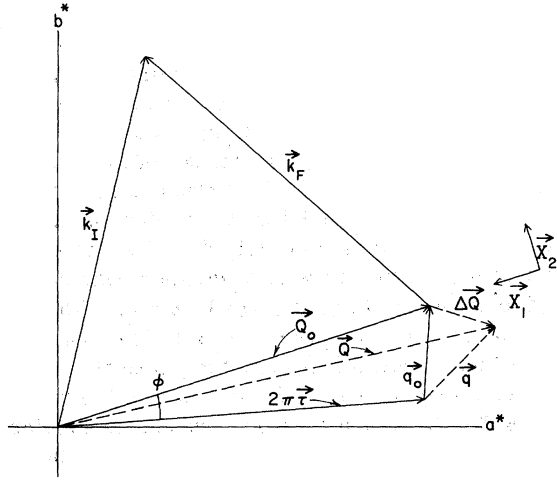
FIG. 2. Diagram of the scattering geometry in recipro-
cal space for elastic scattering. $\vec{k}_I$ and $\vec{k}_F$ are the inci-
dent and scattered wave vectors corresponding to the most
probable process and define the most probable wave vec-
tor transfer $\vec{Q}_o$. Vector $\vec{Q}$ refers to a general elastic
scattering process. Reference reciprocal lattice point
is given by $2\pi\vec{\tau}$. Components of $\Delta\vec{Q}$ in the scattering plane
are referred to axes X_1 and X_2.

dix, however, that its use is proper whenever the
energy changes are small enough to justify using the
"quasielastic" expression for the cross section.

In the experimental determination of the resolu-
tion function by means of the Bragg peak, it is con-
venient to use a nonorthogonal coordinate system
centered at the reciprocal lattice point $2\pi\vec{\tau}$, with
axes $\hat{u}_\phi$, $\hat{u}_\theta$, and $\hat{u}_\chi$ defined in reciprocal space by
the angle of rotation ϕ of the sample about the verti-
cal axis, the counter angle 2θ, and the angle of
rotation χ of the crystal about an axis in the horizon-
tal plane and perpendicular to $2\pi\vec{\tau}$. The resolu-
tion function R_e was obtained on a three-dimension-
al grid by making a series of ϕ scans for different
settings of 2θ and χ. The angular increments in 2θ
and χ were $0.02°$ and $0.1°$, respectively, whereas
the interval in ϕ was $0.02°$ in the central region
($\pm 0.2°$) and $0.05°$ outside this region. Scans were
terminated when the intensity dropped to 0.5% of
that at the center. The maximum number of grid
points covered were 45 along $\hat{u}_\phi$, 31 along $\hat{u}_\theta$, and
25 along $\hat{u}_\chi$.

The effective resolution function was obtained at
$54°K$ using the (111) magnetic reflection. The mag-
netic scattering at this temperature is intense and
only slowly varying with temperature. The data
taken at this temperature are, however, subject to
a small error arising from extinction. If the angu-
lar distribution of mosaic blocks in the sample is
correlated with size (as would be the case, for ex-
ample, if blocks in the wings of the mosaic distri-
bution were actually smaller in size), then the con-

volution with the mosaic distribution would contain
a weighting factor arising from the variation of ex-
tinction with angle. This weighting factor should
not be included in the effective resolution function
used to analyze data in the critical region where ex-
tinction is absent. ϕ scans taken as a function of
temperature did in fact show a small variation in
shape, whereas no effect was observed in the $\hat{u}_\theta$
and $\hat{u}_\chi$ directions. (This is understandable inas-
much as the mosaic distribution does not change in
the $\hat{u}_\theta$ direction, and along $\hat{u}_\chi$ the resolution is too
poor to see the effect.) The variation of shape with
temperature disappeared several degrees below the
Néel point (83 °K) and the data at 81 °K, which ap-
peared to be unaffected either by extinction or crit-
ical scattering, were used to correct the low-tem-
perature resolution function. The intensity in the
wings of the 81 °K profiles, normalized to that in
the center, was approximately 25% lower than that
in the 54 °K scans, but the half-width was decreased
by only about 5%. The final values for the half-half
widths of the resolution function along $\hat{u}_\phi$, $\hat{u}_\theta$, and
$\hat{u}_\chi$ were 0.07°, 0.10°, and 0.48°, respectively, or
expressed as lengths in reciprocal space, 0.0016,
0.0083, and 0.0107 Å^{-1}.

Analytical expressions of the resolution function
for the three-crystal spectrometer and for elastic
scattering by the two-crystal spectrometer have
been obtained by Cooper and Nathans.[1] They as-
sume a Gaussian shape for the collimator trans-
mission function and for the monochromator (and
analyzer in the three-crystal case) mosaic block
angular distribution. The two-crystal elastic reso-
lution function depends on the setting Q_o, the most
probable wave-vector transfer, and is given by

$$R(\vec{q} - \vec{q}_o) = R(\Delta\vec{Q})$$

$$= R_o \exp[-\tfrac{1}{2}(M_{11}X_1^2 + M_{12}X_1X_2 + M_{22}X_2^2 + M_{33}X_3^2)],$$

(3. 2)

where $\vec{Q}$ is a general wave-vector transfer and X_i
are the components of $\Delta\vec{Q} = \vec{Q} - \vec{Q}_o$ with respect to the
following set of orthogonal axes: the X_1 axis is
antiparallel to the scattering vector $\vec{Q}_o$, the X_2 axis
is contained in the scattering plane and is directed
towards the inside of the sphere of reflection, and
the X_3 axis is vertical.[21] The connection between
the vectors $\vec{q}$ and $\vec{Q}$ is shown in Fig. 2. The M_{ij}
are involved algebraic expressions containing, be-
sides k_I and Q_o, the standard deviations of the
Gaussian monochromator mosaic block distribution
(η_M) and of the horizontal and vertical collimator
transmission functions (α and β). The mosaic
spread parameter of the monochromator η_M was ob-
tained from a rocking curve (ϕ scan) of the mono-
chromator placed in the sample position, with a
perfect crystal, reflecting at the same angle, em-
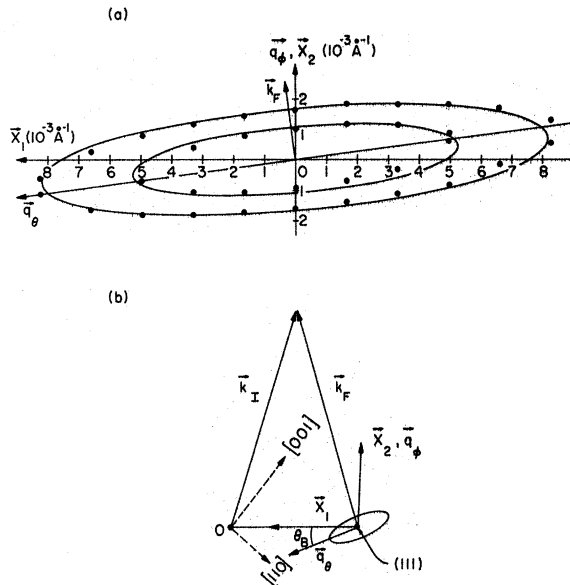ployed as monochromator and with the monochro-

(a)

(b)

FIG. 3. (a) Comparison of theoretical and experimental horizontal two-crystal elastic resolution functions. Solid curves represent the 75 and 50% contours of the resolution function and the points are experimental values. Reciprocal axes X_1 and X_2 are in units of 10^{-3} Å^{-1}. (b) Diagram showing the relative orientation of the resolution ellipsoid with respect to the scattering geometry.

mator-to-sample collimator removed. Under these conditions the rocking curve gives η_M directly.[22] (Note that the same result could have been obtained by rocking a perfect crystal in the sample position with the monochromator fixed in its usual position.) The collimation parameter α was obtained from a detector (i.e., 2θ) scan with the crystal held fixed. The theoretical expression for such a scan is given by Eq. (35) of part III of Ref. 1 for the case of a perfect sample. In the case where the sample has finite mosaic spread, one can obtain the equation for the detector scan by convoluting the general expression for $I(\phi, 2\theta)$, given in Eq. (41) of this reference, with the mosaic spread of the sample. The result is

$$I(2\theta) = I_0 \exp\left[-\tfrac{1}{2} N^2(\Delta 2\theta)^2 \left(1 - \frac{L_S^2}{(F^2 + k_I^2 H_S^2)N^2}\right)\right] \quad ,$$

where the notation is that of Ref. 1. The term containing L_S goes to zero for the case in which $\theta_B = \theta_M$ (focusing condition) and the monochromator-to-sample collimator is removed; it is negligibly small under the conditions of actual measurement, where the sample was RbMnF$_3$ ($\theta_B \approx 7.8°$) and the monochromator was germanium ($\theta_M \approx 11.7°$).

For a Gaussian distribution, the standard deviation is given by $0.425 w$, where w is the full width at half-maximum. In the determination of the collimation parameter α, a somewhat better fit of the

experimental detector scan was obtained with $\alpha = 0.446 \alpha'$, where α' is the geometrical aperture of the slit, given by the slit opening divided by its length. (Ideally, the collimator transmission function should be triangular, but imperfections in the slit system and scattering from the walls make it more nearly Gaussian.[23] If the Gaussian is fitted to a triangular distribution at the center and at the half-width, one finds $\alpha = 0.425 \alpha'$.) The resolution function for the two-crystal experiment was calculated using $\eta_M = 2.7$ min and $\alpha = 4.46$ min. The vertical collimators were geometrically identical to the horizontal collimators and the parameter β was assumed to be related to the aperture in the same way as α. The vertical mosaic spread parameter of the monochromator was assumed equal to the measured horizontal value. Figure 3 shows good agreement between experimental and calculated values of the 50 and 75% resolution function contours in the horizontal plane. The observed and calculated vertical resolution functions agree well, as can be seen in Fig. 4. The effect of sample mosaic ($\eta_S = 1.6$ min) on these curves is small and has not been included in the calculations.

IV. RESULTS OF TWO-CRYSTAL MEASUREMENTS

This section deals with the results of two-crystal measurements in the critical region above and below T_N in the vicinity of the (111) magnetic reciprocal lattice point. The data above T_N are analyzed in terms of the quasielastic approximation. The question of the range of validity of this approximation together with appropriate corrections for inelasticity are covered in detail in Sec. VII and will not be discussed here.

Measurement of the angular distribution of diffusely scattered neutrons can be used to determine the (static) staggered susceptibility, χ, as well as
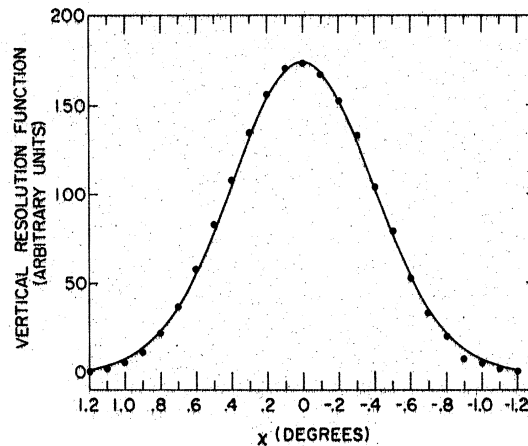

FIG. 4. Comparison of theoretical and experimental vertical resolution functions.

the inverse correlation range parameter κ, using the quasielastic approximation given in Eq. (2.2) for the cross section. Data have been analyzed using an expression for the wavelength-dependent susceptibility given by Fisher and Burford,[13] who have evaluated the Fourier transform of the reduced static spin pair correlation. Their first-order approximant for this Fourier transform, which represents an improvement over the classical Ornstein-Zernike approximation, is

$$\chi(q_o, T)T = \left(\frac{A(T)}{\kappa^2 + q_o^2}\right)^{1-\eta/2} . \quad (4.1)$$

Here A is a very slowly varying function of the temperature T and η is a small positive quantity which is calculated to be 0.056 for the Ising model[13] and 0.02-0.03 for the Heisenberg antiferromagnet,[14] but which is precisely zero in the Ornstein-Zernike approximation. On approaching the critical temperature T_N, both the staggered susceptibility and the correlation range diverge. The critical exponents γ and ν, which characterize the nature of the divergence, are defined by

$$\chi T = \left(\frac{A(T)}{\kappa^2}\right)^{1-\eta/2} \sim \left(\frac{T-T_N}{T}\right)^{-\gamma} \quad (T \rightarrow T_N^+) \quad (4.2)$$

and

$$\kappa \sim \left(\frac{T-T_N}{T_N}\right)^\nu \quad (T \rightarrow T_N^+). \quad (4.3)$$

These definitions lead to the relation

$$\gamma = (2 - \eta)\nu, \quad (4.4)$$

which is a generalization of the Ornstein-Zernike result ($\gamma = 2\nu$).

A. Determination of κ and η

Diffuse scattering data, obtained from ϕ scans using a two-crystal spectrometer, were collected at a number of temperatures above T_N and a non-linear least-squares analysis was used to determine the parameters κ, η, and A. The expression for the observed intensity is, using the coordinate system described in Sec. III,

$$I(q_o) = \iiint \left(\frac{A}{\kappa^2 + (q_\theta\cos\theta_B)^2 + (q_\phi - q_\theta\sin\theta_B - q_o - s_z)^2 + q_\chi^2}\right)^{1-\eta/2} R_e(q_\theta, q_\phi, q_\chi) J\left(\frac{q_x, q_y, q_z}{q_\theta, q_\phi, q_\chi}\right) dq_\theta dq_\phi dq_\chi + B.$$

$$(4.5)$$

Here s_z represents a possible error in the orientation of the crystal in the q_ϕ direction and B is the background. The background, consisting of a q_o-independent component and higher-order nuclear Bragg scattering contributions, was obtained from a run at $T - T_N \approx 50°$, which had been previously corrected for residual magnetic scattering computed on the basis of preliminary estimates of the parameters. The constant component was consistent with values obtained in the critical region by missetting crystal and counter. The background was held fixed in the least-squares analysis. The results of this analysis are listed in Table I. The only weighting applied to the input data was that due to the statistical counting error of the individual points. Since the fit to the data becomes progressively more insensitive to the value of η as the temperature is raised, η was held fixed beginning at 84.50 °K at its average value of 0.067 obtained from the lower temperature data. The over-all agreement is good, although the residue σ is somewhat larger close to the Néel temperature. This probably arises from a combination of several factors: (a) the larger resolution correction; (b) greater sensitivity to temperature fluctuations and temperature gradients over the sample; (c) progressive failure with in-

TABLE I. Least-squares fit of two-crystal data above T_N. Quoted errors are one standard deviation.

T(°K)	$10^2 A$ [a]	$10^6\kappa^2$(Å^{-2})	η	s_z(deg)	Residue
83.055	2.014 ± 0.016	2.436 ± 0.133	0.082 ± 0.004	0.027 ± 0.001	4.14
83.074	1.990 ± 0.014	6.780 ± 0.205	0.070 ± 0.004	0.008 ± 0.001	2.75
83.12	1.991 ± 0.016	18.26 ± 0.47	0.064 ± 0.005	0.009 ± 0.001	3.20
83.166	1.964 ± 0.012	26.92 ± 0.62	0.070 ± 0.005	0.008 ± 0.001	1.39
83.24	2.006 ± 0.015	52.85 ± 1.02	0.063 ± 0.006	0.003 ± 0.001	2.24
83.301	1.972 ± 0.018	68.43 ± 1.98	0.065 ± 0.009	0.028 ± 0.002	2.57
83.60	2.028 ± 0.020	212.6 ± 4.5	0.058 ± 0.010	0.014 ± 0.002	2.41
84.50	2.074 ± 0.013	756.7 ± 8.1	0.067	0.014 ± 0.005	3.05
86.031	2.100 ± 0.024	2088 ± 41.0	0.067	0.064 ± 0.015	0.72
89.695	2.234 ± 0.033	8460 ± 183	0.067	0.025 ± 0.010	1.50
97.956	2.566 ± 0.074	21800 ± 830	0.067	−0.014 ± 0.065	1.59

[a]Note that the quantity A defined in Eq. (4.5) contains an instrumental normalization parameter.
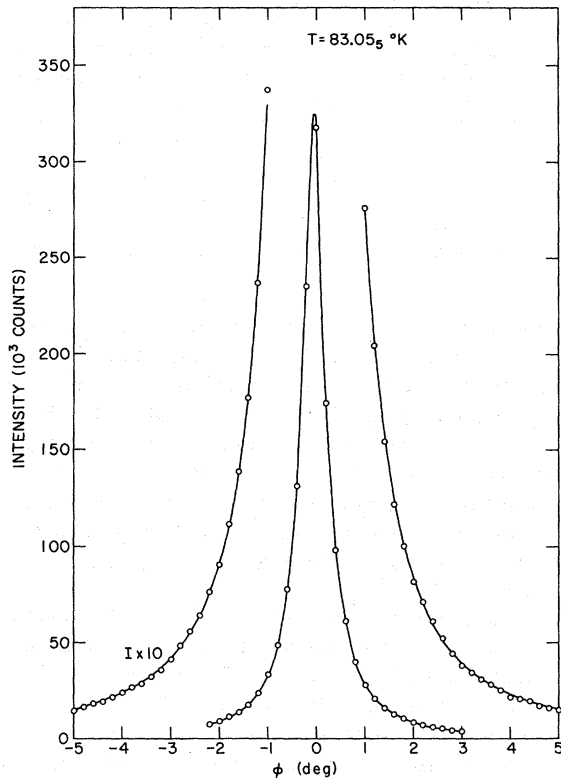
FIG. 5. Least-squares fit of two-crystal data at T = 83.055 °K with $\kappa = 0.00156 \pm 0.00005$ Å^{-1} and $\eta = 0.082 \pm 0.004$. Quoted error is evaluated solely on the basis of the counting statistics. Counting interval is six minutes of time. ($\phi = 5°$ corresponds to a q of 0.11 Å^{-1}.)

the cross section and, ultimately, obtain a second determination of η totally independent of the one described above. These measurements can be characterized as, effectively, a *Néel-temperature* determination of η, making use exclusively of data at large angles which are: (i) large enough so that the resolution correction can be neglected, but nevertheless (ii) well within the range in which the quasielastic approximation is valid. The advantage of a Néel-temperature measurement is that the cross section has the simple form

$$(A/q_o^2)^{1-\eta/2} , \tag{4.7}$$

so that η is the only shape parameter. The advantage of excluding the small-angle data from the analysis is that the resolution correction strongly affects the shape of the experimental intensity pattern and may be a possible source of error in determining η. We shall refer to this set of measurements as the "Néel-temperature high-q" determination of η. The expression actually used in fitting the observed intensity is

$$I = \left(\frac{A}{K^2(q_o)}\right)^{1-\eta/2} + B, \tag{4.8}$$

where

$$K^2 = \frac{6}{a^2}\left(1 - \frac{1}{6}\sum_{\rho=a} e^{i\vec{q}_o \cdot \vec{\rho}}\right) , \tag{4.9}$$

in which $\vec{\rho}$ is the vector coordinate of a lattice site and a is the nearest-neighbor distance. K^2 is the

creasing counting rate of a weighting scheme based solely on counting statistics. Even in the worst case, however, the fit to the data is good in an absolute sense as can be seen in Fig. 5.

The existence or nonexistence of η, i.e., the deviation, if any, from Lorentzian behavior of the diffuse scattering cross section is a matter of some interest. From Table I, one notes that η remains sensibly constant over the temperature range in which it was treated as a free parameter. The best value, over this range, is

$$\eta = 0.067 \pm 0.010 . \tag{4.6}$$

Figure 6 clearly demonstrates the departure of the observed intensity from a Lorentzian shape. In that figure the two solid curves are obtained using Lorentzian cross sections ($\eta = 0$), one of which has been chosen to match the data in the center and the other in the wings. Both have been normalized to the observed intensity at $\phi = -1.0°$. The dashed curve is the one obtained using Eq. (4.5) with $\kappa = 0.00156$ and $\eta = 0.082$.

Another series of measurements was performed in order to verify this non-Lorentzian behavior of

FIG. 6. Illustration of a typical attempt to represent the two-crystal diffuse scattering in terms of a Lorentzian behavior of the cross section. Two solid curves are obtained using Lorentzian cross sections one of which has been chosen to match the data in the center and the other in the wings. Both have been normalized to the observed intensity at $\phi = -1.0°$. The dashed curve is the one obtained using Eq. (4.5) with $\kappa = 0.00156$ and $\eta = 0.082$.

TABLE II. Results of least-squares analyses of Néel temperature two-crystal data taken over the indicated angular range. Note that the different analyses associated with the angular range $(-3°$ to $-9°)$ refer to the same set of data.

ϕ range	B	η	A	Residue	Inelasticity correction	Resolution correction	Counting time	Angular step
$-3°$ to $-30°$	108 ± 9	0.054 ± 0.013	157 ± 4	1.37	no	no	15 min	0.5°
$-3°$ to $-9°$	43	0.053 ± 0.010	62 ± 1	1.30	no	no	6 min	0.1°
	43	0.053 ± 0.010	62 ± 1	1.30	no	yes		
	43	0.053 ± 0.012	60 ± 2	1.33	yes	no		

variable that generalizes the $\vec{q}_o$ dependence of the cross section (4.7) to larger values of $\vec{q}_o$.[13]

The measurements were made at the temperature 83.028 °K $(\kappa < 0.001$ Å$^{-1})$ and the range of angles chosen to satisfy the above requirements (i) and (ii) goes from $-3°$ to $-9°$ $(q_o$ range: 0.067–0.202 Å$^{-1})$.[24] The range of q_o chosen will be justified shortly _a posteriori_ in discussing the results of this analysis that are displayed in Table II. In fitting the data between $-3°$ and $-9°$ the background B is _not_ a free parameter. B is a quantity which was determined independently by means of the following procedure. Data were collected over the angular range $-3°$ to $-30°$ and represented by a function of the form

$$B + f(\vec{q}_o), \qquad (4.10)$$

where $f(\vec{q}_o)$ stands for the magnetic scattering cross section. The assumption is then made that one can use $(A/K^2)^{1-\eta/2}$ with A and η adjustable parameters, as a "model" for $f(\vec{q}_o)$ in the following sense: _even if_ the quasielastic approximation should break down over such a wide angular range (but this is probably untrue as we shall see shortly) the function $(A/K^2)^{1-\eta/2}$ is still a close enough representation of $f(\vec{q}_o)$ so that by means of an adequate distortion of the parameters A and η, it can adjust itself to reproduce the $\vec{q}_o$ dependence of f over the angular range $-3°$ to $-30°$. In fact the statistical accuracy is sufficiently good and the angular range sufficiently large so that, if one is misrepresenting the function f in Eq. (4.10), the failure can hardly be compensated by a change in the constant background. Therefore, because of this decoupling, the residue resulting from the three-parameter fit obtained using the interpolation function (4.8) provides a measure of the reliability of the "model" and hence of B. The results obtained from the least-squares fit described above, over the angular range $-3°$ to $-30°$, are displayed on the first line of Table II. The corresponding data, together with the least-squares curve of the form (4.8), are shown in Fig. 7 in a log-log plot of $(I-B)K^2$ vs K. Note that in such a plot a horizontal straight line would represent the $\eta = 0$ case. The magnitude of the experimental error varies considerably over the range covered by the data, however, the over-all distribution of the ex-

perimental points is consistent with a linear trend as given, in such a log-log plot, by a function of the form (4.8). Quantitatively, the quality of the agreement is given by the residue 1.37 (Table II). Note that the _only result_ being retained from this fit is the value of the background B (108 counts in 15 min) in order to allow for the possibility that the value of η has been distorted so as to reproduce effectively, as explained above, the magnetic scattering function $f(\vec{q}_o)$.

Having determined the value of the background B by means of the above procedure, the analysis of the data in the range $-3°$ to $-9°$ was carried out in order to determine the best value of η. Three separate least-squares fits of the data, corresponding to three different choices for the magnetic scattering intensity functions, were performed using the normalization and the exponent η as free parameters. The first choice, as shown in Table II, corresponds to the function given by Eq. (4.8) which makes no correction for the effect of resolution or inelasticity; the second and third choices use forms for the magnetic scattering intensity in which first resolution and then inelasticity are separately corrected for. The resolution-corrected intensity is obtained, as usual, using Eq. (4.5). (Here, of course, we put $\kappa = 0$; furthermore, the correction s_Z is set equal to zero because the intensity, at angles greater than 3°, is unsenstive to it.) The
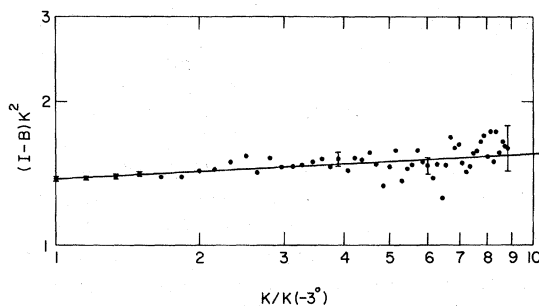

FIG. 7. Log-log plot of $(I-B) K^2$ vs K, for the range $-3°$ to $-30°$. I is the total intensity, B is the background, and K is the generalization of the q_o variable defined in Eq. (4.9). Straight line represents the least-squares fit to the data and corresponds to $\eta = 0.054$.

FIG. 8. Plot of $\ln[(I-B)K^2]$ vs $\ln K$ for the range $-3°$ to $-9°$. I is the total intensity, B is the background and K is the generalization of the q_0 variable defined in Eq. (4.9). Straight line represents the leas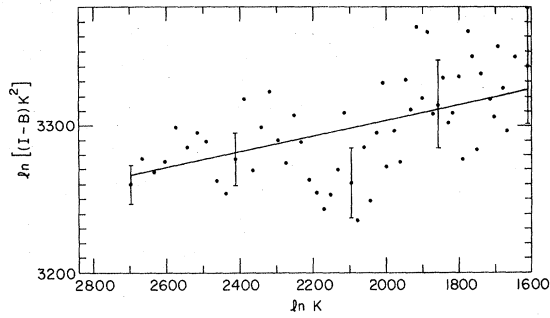t-squares fit to the data and corresponds to $\eta = 0.053$. Note that the case $\eta = 0$ corresponds to a horizontal line in this plot.

inelasticity is accounted for by using, in place of the two-crystal cross section, the expression for the full line integral of the differential scattering cross section (2.1), with respect to energy, along the path of the scattered beam. These line integrals can be computed, as explained in detail in Sec. VII, by using, for the ω dependence of the cross section, the results of the three-crystal measurements; normalization and η are left as free parameters in the expression for the line integral. Such an analysis of two-crystal data, done in terms of line integrals of the inelastic scattering cross section, we call "inelastic analysis" of two-crystal data. Comparison of the results of the three fits shows the following: (i) The resolution correction can surely be neglected, at angles greater than $3°$ and (ii) the inelasticity is certainly negligible over the angular range $-3°$ to $-9°$. The result of the analysis is

$$\eta = 0.053 \pm 0.010. \qquad (4.11)$$

In Fig. 8, we plot $\ln[(I-B)K^2]$ vs $\ln K$. The data are shown along with the best-fit straight line given by the equation

$$\ln[(I-B)K^2] = 0.053 \ln K + 0.9735 \ln 69. \qquad (4.12)$$

The statistics on the individual points are not as good as in the scan between $-3°$ and $-30°$, but the angular step is 5 times finer, thus accounting for the final small statistical error on η. We note the surprising result that the two independent fits over the ranges $-3°$ to $-30°$ and $-3°$ to $-9°$ give practically identical values for η. This seems to indicate that the quasielastic approximation may well hold far beyond the range of angles where it can be directly tested by using the results of the inelastic measurements (see Sec. VII). In any case, by looking at either set of data shown in Figs. 7 and 8, it is clear that *a horizontal, i.e., $\eta = 0$, straight line*

cannot be drawn through the data, without, on one hand, impairing quantitatively the goodness of the fit and giving rise, on the other hand, to local systematic trends of the deviations from experiment.

The value of η given in Eq. (4.11) is the final result of the "Néel-temperature high-q" measurement. It is consistent with the value given in Eq. (4.6), which was the result of a quasielastic analysis of the full scattering curve carried out over a range of temperatures $0.0042 < (T-T_N)/T_N < 0.00700$. This consistency is noteworthy because the latter analysis relies heavily on a proper resolution correction plus a proper evaluation of κ, to which η is correlated, and these constitute possible sources of error quite different from those in the analysis resulting in the value (4.11) where, on the contrary, the evaluation of the background plays a major role. In addition to the above, we have carried out still another evaluation of η, which is described in detail in Sec. VII B 2. It is the result of an inelastic analysis of two-crystal data at $(T-T_N)/T_N = 0.00042$ over an "intermediate" angular range in which the background is no longer important but where a resolution correction is required. We quote here the result of that analysis:

$$\eta = 0.044 \pm 0.010. \qquad (4.13)$$

From the three independent evaluations of η referred to above we obtain, by averaging, our final value:

$$\eta = 0.055 \pm 0.010. \qquad (4.14)$$

B. Determination of ν, γ, and β; Static Scaling

The values of the inverse correlation range κ tabulated in Table I were used to determine the critical exponent ν defined in Eq. (4.3). A least-squares analysis in which the Néel temperature T_N is treated as a free parameter gives $\nu = 0.707$
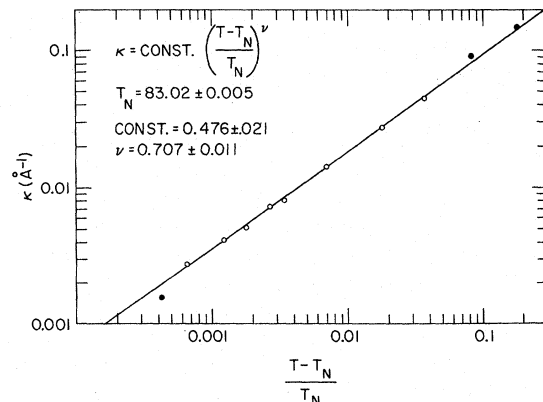

FIG. 9. Log-log plot of κ vs $(T-T_N)/T_N$. Line is the best fit to the data using Eq. (4.3). Closed circles were omitted in the fit for reasons explained in the text.
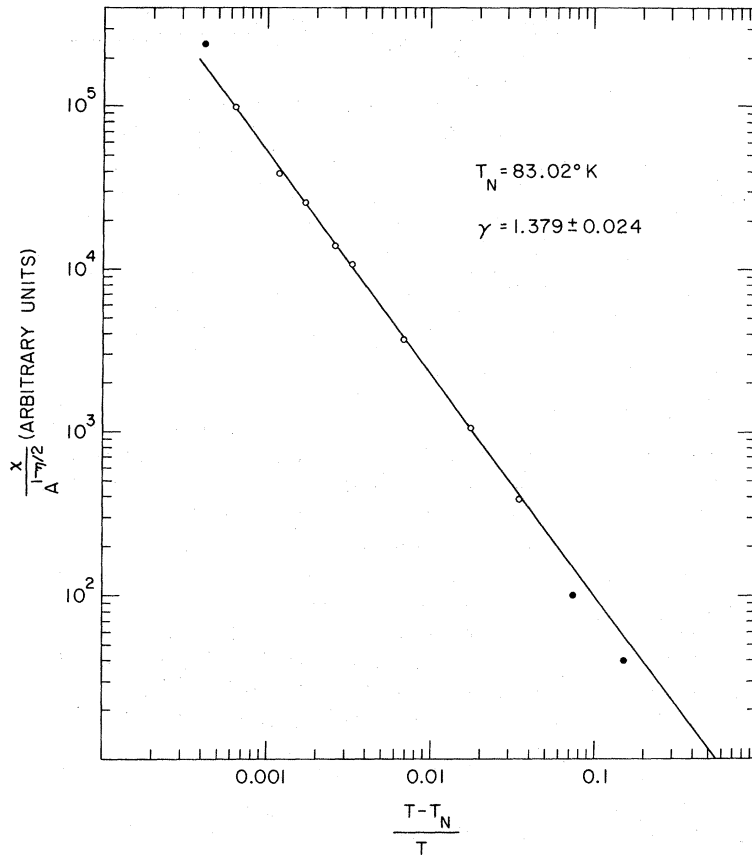
FIG. 10.   Log-log plot of $\chi/A^{1-\eta/2}$ vs $(T-T_N)/T$.   Straight line is the best fit to the data.   Closed circle was omitted in the fit for reasons explained in the text.

± 0.011 and $T_N = (83.02 \pm 0.01)°$K.   Figure 9 is a log-log plot of κ against $(T - T_N)/T_N$ together with the best fit obtained from the least-squares analysis. Similar treatment of the data from Table I can be used to evaluate γ, the critical exponent associated with the divergence of the staggered susceptibility. χT is given by $[A(T)/\kappa^2]^{1-\eta/2}$.   If $A(T)$ is well behaved in the sense that $\ln A/\ln[(T - T_N)/T] \to 0$ as $T \to T_N^+$, χT can be written in the form $[A(T)]^{1-\eta/2}$ $\times [(T - T_N)/T]^{-\gamma}$, where γ is the exponent defined in (4.2). $A(T)$ is essentially constant as shown in Table I and thus the exponent γ is the slope of a straight line in a plot of $\ln\{\chi T/[A(T)]^{1-\eta/2}\}$ vs $\ln[(T - T_N)/T]$.   A least-squares treatment gives $\gamma = 1.379 \pm 0.024$ and $T_N = (83.02 \pm 0.01)°$K and the fit using these values is shown in Fig. 10.   In the analyses leading to the determination of γ and ν, the lowest temperature point and the two highest temperature points of Table I were omitted, the latter because of significant inelasticity corrections as calculated in Sec. VII and the former for reasons given in the beginning of Sec. IV A.   The analysis of these inelasticity effects carried out in Sec. VII can be used to correct the "quasielastic" values of γ and ν and the results are listed in Table III.   Jasnow and Wortis,[14] using a series expansion for the pair-correlation function, have calculated values for ν and γ

of 0.70 and 1.38, respectively, which they consider good to 1%.   These values may be compared with our final values of 0.701 ± 0.011 and 1.366 ± 0.024.

The three critical indices we have measured are related by the static-scaling law, $\gamma = (2 - \eta)\nu$.   This relationship is implied in Eq. (4.1) provided η is temperature independent and $A(T)$ is well behaved in the sense noted above.   The data of Table I show that these requirements are indeed satisfied and thus the scaling law is confirmed.   The data for $A(T)$ given in Table I were corrected for inelasticity and then fitted with an expression of the form $A[1 + C(T - T_N)/T]$.   Our best estimate of the slope C is 0.6 ± 0.3.   This may be compared to the value 0.49 calculated by Fisher and Burford[13] for the Ising model.   The agreement between the last two columns of Table III, that is, between the experimental values of γ and $(2 - \eta)\nu$, is simply an indication of the constancy of the experimental values of η.

The coherent magnetic scattering just below T_N was also measured in order to determine the critical exponent β which is defined by the expression

$$M \sim (T_N - T)^\beta ,$$

where M is the sublattice magnetization.   The coherent magnetic scattering cross section is directly

TABLE III. Critical indices for $T \geq T_N$.

Origin of quoted values		η	ν	γ	$(2-\eta)\nu$
Quasielastic analysis	Fit of full scattering curve $T > T_N$	0.067 ± 0.010	0.707 ± 0.011	1.379 ± 0.024	1.367
Inelastic analysis	"Néel temperature high-q" measurement	0.053 ± 0.010			
	"Néel temperature intermediate-q" measurement	0.044 ± 0.010			
	Corrected exponents		0.694 ± 0.011	1.354 ± 0.024	1.354^a
Final value (average)		0.055 ± 0.010	0.701 ± 0.011	1.366 ± 0.024	1.363

^{a}Calculated using the average value of η obtained from the inelastic analysis.

proportional to the square of M. There are, however, several experimental difficulties which preclude the measurement of M, and thus β, over a wide temperature range. As one approaches T_N, the Bragg scattering rapidly decreases while the diffuse critical scattering becomes strongly peaked about the Bragg reciprocal lattice point so that it becomes increasingly difficult to make a correction for the diffuse component. This sets an upper limit to the temperature range over which M can be measured. The lower limit is set at the point where extinction causes the measured cross section to deviate significantly from proportionality to M^2. The temperature limits were set experimentally as follows. The lower limit was fixed by making measurements on the (111), (333), and (555) reflections and utilizing the fact that the ratios of the cross sections remain constant, as a function of temperature, in the absence of extinction. The onset of extinction can then be observed by noting the departure of the measured intensities from these ratios. The fixing of the upper limit is somewhat more arbitrary. The form of the cross section for critical scattering is known only in the hydrodynamic regime, and so there is no good basis for estimating the diffuse scattering. In addition, the single crystal of RbMnF$_3$ used in these experiments had a mosaic distribution which produced a small Bragg contamination in the wings of the diffuse peak, thus making it difficult to reconstruct the diffuse scattering at the center from its value in the wings. The procedure finally adopted was the following. We assumed that the convolution with the resolution function of $1/(\kappa^2+q^2)$ provides, as κ is varied, a set of curves one of which would represent a fair approximation to the *shape* of the magnetic critical scattering at a given temperature below T_N. The shape of the magnetic coherent scattering is given directly by the experimental resolution function and its intensity is proportional to the unknown scale factor M^2. We determined M^2 by assuming trial values and subtracting the corresponding coherent scattering from the observed intensity and refining

this value until the remainder had a shape similar to one of the "critical scattering curves" described above. The upper temperature limit was then set rather arbitrarily by using, in the least-squares analysis, only those data for which the estimated critical scattering was no greater than 5% of the total scattering. Furthermore, only the (333) and (555) reflections were used in determining β because the (111) data are most affected by extinction. Assuming the Néel temperature derived from the data above T_N, the average value of β determined from the least-squares analysis is 0.32 ± 0.02. The data together with the least-squares results are shown in a log-log plot of coherent magnetic scattering intensity against $(T_N - T)$ in Fig. 11. In addition, a line using the above value of β, is drawn through the
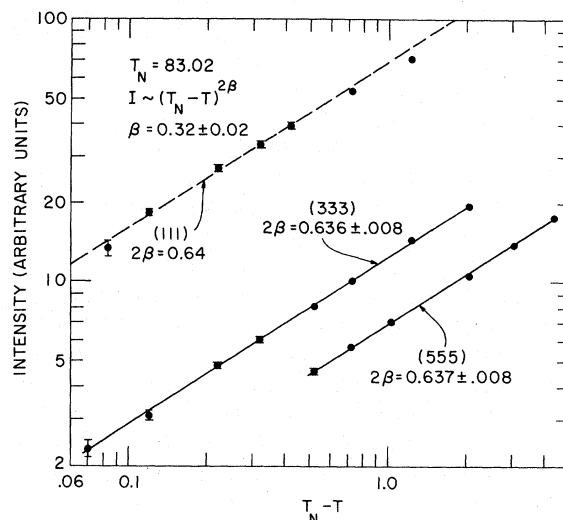
FIG. 11. Log-log plot of coherent scattering intensities vs $T_N - T$ for the (111), (333), and (555) magnetic reflections. Solid lines are the results of the least-squares analyses. Dotted line drawn through the (111) data, using the best value of β, indicates the consistency of these results with this value as well as the effect of extinction on the lowest temperature points. Intensity scales for the three sets of data are individually normalized.

(111) data to indicate the consistency of these results with β as well as the effect of extinction on the lowest temperature points.

The measurement of β and that of ν' (reported in Sec. VIE) provide another test of static scaling. From the scaling relations

$$(2 - \eta) \nu' = \gamma'$$

and

$$\gamma' = 3\nu' - 2\beta,$$

where the primes indicate that these exponents refer to $T < T_N$, one finds that

$$2\beta = (1 + \eta) \nu'.$$

The measured value for ν' is 0.54 ± 0.03 which yields β equal to 0.285 ± 0.015 which is to be compared with the observed value of 0.32 ± 0.02.

V. THREE-CRYSTAL RESOLUTION FUNCTION

Whereas the resolution function can be determined experimentally in the two-crystal case using the coherent Bragg reflection, there is no suitable probe for determining the three-crystal resolution function for arbitrary energy and momentum transfers. We have, instead, calculated the resolution function using the result of Cooper and Nathans[1] who show

that for an energy change $\hbar\omega = (\hbar^2/2m)\ (k_i^2 - k_f^2)$, a wave-vector transfer $\vec{Q} = \vec{k}_i - \vec{k}_f$, and an instrumental setting $(\omega_o, \vec{Q}_o)$, defined in terms of the most probable values of the wave vectors $\vec{k}_F$ and $\vec{k}_I$, the resolution function can be written

$$R(\omega_o + \Delta\omega, \ \vec{Q}_o + \Delta\vec{Q}) = R_o \exp\left(-\frac{1}{2} \sum_{k,l=1}^{4} M_{kl}\, X_k X_l\right),$$

$$(5.1)$$

where $X_4 = \Delta\omega$ and X_1, X_2, X_3 are the components of the vector $\Delta\vec{Q}$ with respect to the following set of orthogonal axes: the X_1 axis is antiparallel to $\vec{Q}_o$, the X_2 axis is contained in the scattering plane and is directed towards the inside of the sphere of reflection, and the X_3 axis is vertical.[21] R_o depends on the setting $(\omega_o, \vec{Q}_o)$ and its explicit form will be derived later in this section [see Eq. (5.11)].

We shall be concerned with making quantitative comparisons of intensities at different points in $\vec{Q}$-ω space and therefore consider in some detail the dependence of intensity on resolution and cross section. For a spectrometer set for an incident wave vector $\vec{k}_I$ and a scattered wave vector $\vec{k}_F$, the probability of detecting neutrons whose wave vectors deviate in magnitude and direction from these most probable values, is given by the expression[1]

$$P(\Delta k_i, \ \Delta k_f, \ \gamma_1, \gamma_2, \ \delta_1, \ \delta_2)$$

$$= \epsilon P_M P_A P_o \exp\left\{-\frac{1}{2}\left[\left(\frac{(\Delta k_i/k_I)\tan\theta_M + \gamma_1}{\eta_M}\right)^2 + \left(\frac{(\Delta k_f/k_F)\tan\theta_A - \gamma_2}{\eta_A}\right)^2 + \left(\frac{2(\Delta k_i/k_I)\tan\theta_M + \gamma_1}{\alpha_0}\right)^2 + \frac{\gamma_1^2}{\alpha_1^2} + \frac{\gamma_2^2}{\alpha_2^2}\right.\right.$$

$$\left.\left. + \left(\frac{2(\Delta k_f/k_F)\tan\theta_A - \gamma_2}{\alpha_3}\right)^2 + \left(\frac{\delta_1^2}{4\sin^2\theta_M\, \eta_M'^2 + \beta_0^2}\right) + \frac{\delta_1^2}{\beta_1^2} + \frac{\delta_2^2}{\beta_2^2} + \left(\frac{\delta_2^2}{4\sin^2\theta_A\, \eta_A'^2 + \beta_3^2}\right)\right]\right\} , \quad (5.2)$$

where Δk_i and Δk_f are the deviations of k_i and k_f from the nominal values k_I and k_F; η_M and η_M' are the mosaic spread parameters of the monochromator in the horizontal and vertical planes, with similar definitions for the analyzer parameters η_A and η_A'; γ_n and δ_n are horizontal and vertical divergence angles; α_n and β_n are the horizontal and vertical Gaussian collimation parameters (standard deviations); and the subscripts 0, 1, 2, 3, refer to the in-Pile region, the monochromator-to-sample region, the sample-to-analyzer region, and the analyzer-to-counter region, respectively. P_M and P_A are the reflectivities of the monochromator and analyzer for wave vectors k_I and k_F, ϵ is the BF$_3$ counter efficiency, and P_o is given by[25]

$$P_o = \frac{2\pi}{4\sin\theta_M \sin\theta_A}$$

$$\times\left(\frac{1}{\beta_0^2} + \frac{1}{4\sin^2\theta_M \eta_M'^2}\right)^{-1/2}\left(\frac{1}{\beta_3^2} + \frac{1}{4\sin^2\theta_A\, \eta_A'^2}\right)^{-1/2}. \quad (5.3)$$

The intensity of scattering is

$$\mathscr{I} = \epsilon\Phi_0 \int P(\Delta k_i, \ \Delta k_f, \ \gamma_1, \ \gamma_2, \ \delta_1, \ \delta_2)$$

$$\times\left(\frac{d\sigma}{d(\Delta k_f)d\gamma_2 d\,\delta_2}\right) d(\Delta k_i)\, d(\Delta k_f)\, d\gamma_1 d\gamma_2 d\,\delta_1 d\,\delta_2,$$

$$(5.4)$$

where Φ_0 is the flux per unit of solid angle and per unit of incident wave vector. ϵ and Φ_0 are slowly varying functions of k_F and k_I, respectively, and essentially constant over the volume of integration. For the usual case in which the cross section, except for slowly varying factors, can be taken to be a function of $\vec{Q}$ and ω only, it is convenient to transform coordinates from the set Δk_i, Δk_f, γ_1, γ_2, δ_1, δ_2 to a set such as X_1, X_2, X_3, X_4, Δk_i, δ_1. The intensity expression can then be simplified by integrating over the variables Δk_i and δ_1, since the cross section depends only on the X_n. Thus, we can rewrite (5.4) as

$$I = \frac{\mathcal{J}}{\Phi_0} = \epsilon \int \left[J\left(\frac{\Delta k_f, \gamma_1, \gamma_2, \delta_2, \Delta k_i, \delta_1}{X_1, X_2, X_3, X_4, \Delta k_i, \delta_1}\right) \right.$$

$$\left. \times \int P(\Delta k_i, \Delta k_f, \gamma_1, \gamma_2, \delta_1, \delta_2) d(\Delta k_i) d\delta_1 \right]$$

$$\times \sigma (X_1, X_2, X_3, X_4) dX_1 dX_2 dX_3 dX_4, \quad (5.5)$$

where J is the Jacobian of the transformation, $'m/(\hbar k_I k_F^3 \sin 2\theta_s)$, and σ is an abbreviation for the differential cross section in (5.4). The resolution function is defined by the expression

$$R(X_1, X_2, X_3, X_4) = J\left(\frac{\Delta k_f, \gamma_1, \gamma_2, \delta_2, \Delta k_i, \delta_1}{X_1, X_2, X_3, X_4, \Delta k_i, \delta_1}\right)$$

$$\times \int P(\Delta k_i, \Delta k_f, \gamma_1, \gamma_2, \delta_1, \delta_2) d(\Delta k_i) d\delta_1, \quad (5.6)$$

and represents the probability of detection in a scattering process corresponding to given values of $\vec{Q}$ and ω when the nominal spectrometer setting is $\vec{Q}_o$, ω_o. The *total detection efficiency*, that is, the intensity that would be observed for unit scattering cross section, is given by

$$D_0 = \epsilon \int R(X_1, X_2, X_3, X_4) dX_1 dX_2 dX_3 dX_4, \quad (5.7)$$

and measures the size and efficiency of the instrumental "window" in $\vec{Q}$-ω space. To exhibit this factor explicitly, we write the intensity in terms of a normalized resolution function, so that

$$I = D_0 \int R'(X_1, X_2, X_3, X_4)$$

$$\times \sigma (X_1, X_2, X_3, X_4) dX_1 dX_2 dX_3 dX_4, \quad (5.8)$$

where

$$R'(X_1, X_2, X_3, X_4) = \frac{R(X_1, X_2, X_3, X_4)}{\int R(X_1, X_2, X_3, X_4) dX_1 dX_2 dX_3 dX_4}.$$

$$(5.9)$$

Thus, if σ is slowly varying, that is, if it is essentially constant over the region of $\vec{Q}$-ω space where the resolution function is nonzero, the intensity is given simply by $D_0 \sigma$. Equation (5.7) can in principle be integrated to obtain D_0 using the expressions for M_{ki} given in Ref. 1 together with Eq. (5.11) for R_o. A simple and more direct procedure, however, is to integrate the probability expression in (5.2) over the indicated variables. In this way one finds, for α_n, β_n, and η_n small compared to $\frac{1}{2}\pi$,

$$D_0 = \frac{\pi \epsilon P_M P_A}{2 \sin\theta_M \sin\theta_A} \left(\frac{1}{\beta_0^2} + \frac{1}{4\sin^2\theta_M \eta_M'^2}\right)^{-1/2} \left(\frac{1}{\beta_3^2} + \frac{1}{4\sin^2\theta_A \eta_A'^2}\right)^{-1/2}$$

$$\times 2\pi k_I \cot\theta_M \left[\left(\frac{1}{\eta_M^2} + \frac{4}{\alpha_0^2}\right)\left(\frac{1}{\eta_M^2} + \frac{1}{\alpha_0^2} + \frac{1}{\alpha_1^2}\right) - \left(\frac{1}{\eta_M} + \frac{2}{\alpha_0}\right)^2 \right]^{-1/2} 2\pi k_F \cot\theta_A \left[\left(\frac{1}{\eta_A^2} + \frac{1}{\alpha_3^2}\right)\left(\frac{1}{\eta_A^2} + \frac{1}{\alpha_3^2} + \frac{1}{\alpha_2^2}\right) - \left(\frac{1}{\eta_A} + \frac{2}{\alpha_3}\right)^2 \right]^{-1/2}$$

$$\times 2\pi \left(\frac{1}{4\sin^2\theta_M \eta_M'^2 + \beta_0^2} + \frac{1}{\beta_1^2}\right)^{-1/2} \left(\frac{1}{4\sin^2\theta_A \eta_A'^2 + \beta_3^2} + \frac{1}{\beta_2^2}\right)^{-1/2}. \quad (5.10)$$

This expression is symmetrical in the monochromator and analyzer terms and, apart from the instrumental parameters, depends only on k_I and k_F. In the usual case of loose vertical collimation, one has $\beta_3 \gg 2\sin\theta_A \eta_A'$ and $\beta_0 \gg 2\sin\theta_M \eta_M'$, and thus $D_0 \propto \epsilon P_M P_A k_I k_F \cot\theta_M \cot\theta_A$. For the important practical case of an energy scan at constant k_I, $\cot\theta_A$ is generally essentially proportional to k_F and, apart from the energy dependence of the counter efficiency and the analyzer reflectivity, $D_0 \approx \text{const} \times k_F^2$. If the cross section $d\sigma/d(\Delta k_f) d\gamma_2 d\delta_2$ is replaced by $(\hbar k_f/m)(d^2\sigma/d\Omega \, d\omega)$ and if we include the factor k_f coming from the "density of final states" term in the cross section, the intensity is seen to be proportional to k_F^4. (k_f is essentially constant over the volume of $\vec{Q}$-ω space where the resolution function is nonzero and can be replaced by k_F.) The analytical expression (5.10) is particularly convenient for calculating the effect on the intensity of varying the instrumental parameters. Referring to Eq. (5.1), D_0 can be written as the product $\epsilon R_o \Delta V$, where ΔV is proportional to the product of the half-widths of the resolution ellipsoid along its principal axes and measures the volume occupied by the resolution function in $\vec{Q}$-ω space. Using the notation of Ref. 1, we find that R_o and ΔV are given by the following expressions:

$$R_o = \frac{\pi P_M P_A}{2 \sin\theta_M \sin\theta_A \, k_I^2 k_F^3 \sin(2\theta_S)(a_{11}^2 + a_{12}^2)^{1/2}(A')^{1/2}}$$

$$\times \left(\frac{1}{\beta_0^2} + \frac{1}{4\sin^2\theta_M \eta_M'^2}\right)^{-1/2} \left(\frac{1}{\beta_3^2} + \frac{1}{4\sin^2\theta_A \eta_A'^2}\right)^{-1/2},$$

$$(5.11)$$

$$\Delta V = (2\pi)^3 k_I^2 k_F^3 \sin(2\theta_S)(A')^{1/2} \frac{(a_{11}^2 + a_{12}^2)^{1/2}}{a_{11} a_{12}}$$

$$\times \cot\theta_M \left[\left(\frac{1}{\eta_M^2} + \frac{1}{\alpha_0^2}\right)\left(\frac{1}{\eta_M^2} + \frac{1}{\alpha_0^2} + \frac{1}{\alpha_1^2}\right) - \left(\frac{1}{\eta_M} + \frac{2}{\alpha_0}\right)^2 \right]^{-1/2}$$

$$\times \cot\theta_A \left[\left(\frac{1}{\eta_A^2} + \frac{4}{\alpha_3^2}\right)\left(\frac{1}{\eta_A^2} + \frac{1}{\alpha_3^2} + \frac{1}{\alpha_2^2}\right) - \left(\frac{1}{\eta_A} + \frac{2}{\alpha_3}\right)^2 \right]^{-1/2}.$$

$$(5.12)$$

Note that R_0 and ΔV depend on $\vec{Q}_o$, whereas the product D_0 does not. While D_0 varies approximately as k_I^4 for small ω, inspection of Eq. (5.12) shows that the volume of the resolution ellipsoid increases approximately as k_I^5 [since, for $k_F = k_I$, $(A')^{1/2}$ $\approx 1/k_I^2$]. For the experimental arrangement used in the present work, the calculated value of ΔV increases by a factor of about 160 in going from an incident energy of 6.6 to 47 meV.

The instrumental parameters required for computing the resolution function were all determined experimentally. The horizontal collimation parameters and the mosaic spread parameters were obtained from suitable rocking curves as explained in Sec. III in discussing the two-crystal resolution function. For the case of loose vertical collimation, the vertical parameters β_n cannot be measured directly, nor can they be calculated on the basis of the geometrical aperture since other geometrical features of the instrument may limit the vertical divergence. Effective vertical parameters were computed from the observed vertical resolution obtained by rocking the sample about a horizontal axis perpendicular to the scattering vector of the Bragg magnetic peak. In this case where the geometrical contribution to the vertical divergence is large compared to that produced by the vertical mosaic distributions of monochromator and analyzer, the vertical part of the resolution function is proportional to $\exp(-\frac{1}{2}M_{33}X_3^2)$ with

$$M_{33} \approx \frac{1}{k_I^2}\left(\frac{1}{\beta_0^2} + \frac{1}{\beta_1^2}\right)\left(\frac{1}{\beta_2^2} + \frac{1}{\beta_3^2}\right) \Big/ \left(\frac{1}{\beta_0^2} + \frac{1}{\beta_1^2} + \frac{1}{\beta_2^2} + \frac{1}{\beta_3^2}\right).$$

(5.13)

Effective values of β_n were obtained by setting $\beta_n = C\beta_n'$, where β_n' is the geometrical vertical aperture of the nth collimator. The constant C is readily determined from Eq. (5.13) using the experimental value of M_{33} and the nominal values β_n'.

The resolution function was calculated using values of the instrumental parameters determined experimentally as indicated above. The result was checked below the Néel point using the coherent magnetic reflection of the sample as a probe, by observing the intensity as the Bragg spot was moved relative to the resolution function along all four axes of $\vec{Q}$-ω space for $\vec{Q}_o = 2\pi\vec{\tau}$ and $\omega_o = 0$. Small adjustments in the mosaic spread parameters were made to obtain the best agreement between the calculated and observed traverses. These adjustments were assumed to compensate for the effect of sample mosaic spread, which was very small and had not been specifically taken into account. Final experimental values of the parameters are listed in Table IV. Vertical mosaic spread parameters for both the monochromator and analyzer were assumed to be the same as the horizontal parameters.

Observed and calculated half-widths for the resolution function centered at $\vec{Q}_o = 2\pi\vec{\tau}$ and $\omega_o = 0$ [that is, at the Bragg magnetic (111) reflection and in the neighborhood of zero-energy transfer] are given in Table V for incoming neutron energies of 6.6, 13.0, and 47.0 meV. On the left-hand side of the table, widths are referred to the four-dimensional orthogonal laboratory coordinate system X_1, X_2, X_3, X_4, where the energy axis X_4 is in units of Å^{-2} (1 Å^{-2} = 2.07 meV). The resolution ellipsoid can be transformed to principal axes X_n' by diagonalizing the 4×4 resolution matrix M of Eq. (5.1). For typical experimental parameters, X_1' is almost along X_1; X_2' and X_4' lie nearly in the X_2-X_4 plane, making small angles with X_2 and X_4, respectively; and X_3' coincides with X_3. Widths referred to the principal axes are given on the right-hand side of Table V. The slope of the principal axis X_4' with respect to the X_1-X_2 plane is given approximately by $2k_I$ Å^{-1}.

The "detection" system, consisting of the analyzing crystal and the counter, has an energy-dependent sensitivity which is the product of the counter sensitivity ϵ and the analyzer reflectivity P_A. This product was measured directly for the energy ranges of interest and for the actual configuration of the "detection" system used in the normal operation of the spectrometer. A well-collimated monoenergetic incident beam, provided by the monochromating part of the spectrometer and monitored by passing through a BF$_3$ detector whose sensitivity was accurately proportional to $1/v$, was counted in the "detection" system for varying values of the incident energy. For each setting of the incident energy, the positions of analyzing crystal and counter were adjusted for maximum intensity. The energy sensitivity, which is the fraction of the incident neutron flux detected, is proportional to the number of counts recorded per unit monitor count, multiplied by $1/v$. In this measurement it is essential that all neutrons passing through the monitor be capable, after reflection by the analyzer, of passing through the counter collimator and entering the

TABLE IV. Experimental resolution parameters.

Parameter[a]	Description	Value (radians)
α_0, α_1, α_2, α_3	horizontal collimator angle	0.00274
β_0		0.00909
β_1	vertical collimator angle	0.01527
β_2		0.01976
β_3		0.01976
η_M	horizontal mosaic spread (monochromator)	0.00198
η_A	horizontal mosaic spread (analyzer)	0.00198

[a]Subscripts 0, 1, 2, 3 refer to the in-Pile region, the monochromator-to-sample region, the sample-to-analyzer region, and the analyzer-to-counter region, respectively. The collimator lengths in these regions are 36, 24, 16, and 16 in., respectively.

TABLE V. Observed and calculated resolution function widths. Tabulated values are half-widths at half-maximum.

E_i (meV)	Laboratory coordinates								Principal axes (calculated)			
	Observed				Calculated							
	X_1(Å⁻¹)	X_2(Å⁻¹)	X_4(Å⁻²)ᵃ	X_3(Å⁻¹)	X_1(Å⁻¹)	X_2(Å⁻¹)	X_4(Å⁻²)	X_3(Å⁻¹)	X_1'	X_2'	X_4'	X_3'
6.6	0.0043	0.0017	0.0048	0.034	0.0044	0.0014	0.0046	0.034	0.0044	0.0014	0.034	0.034
13.0	0.0056	0.0016	0.0077	0.047	0.0060	0.0014	0.0068	0.047	0.0063	0.0015	0.099	0.047
47.0	0.010	0.0014	0.0140	0.090	0.012	0.0014	0.0135	0.090	0.012	0.0015	0.716	0.090

ᵃ1 Å⁻² = 2.07 meV.

counter. This was ensured by placing the monitor just before the analyzing crystal and reducing the collimation before and after the monochromator to one-half the angular aperture of the counter collimator. The sensitivity is a slowly varying function of the energy, but the experimental curve exhibits dips produced by the occurrence of simultaneous reflections in the analyzing crystal. These dips can be minimized for a given range of neutron energies by rotating the analyzing crystal around its scattering vector, but they cannot, in general, be eliminated entirely. In an actual experiment, the dips are less serious since the finite resolution of the instrument effectively averages the sensitivity over a range of energies. In most cases it is sufficient to use an average sensitivity obtained by convoluting the measured sensitivity with the resolution function.

The integrations indicated in Eq. (5.8) were performed as summations over 10^4 points defined by a four-dimensional grid in the principal-axis coordinate system. The grid was constructed by subdividing each axis, from the origin of the resolution function to the point where it reached 0.5% of its value at the origin, into five equal intervals. For points selected in this way, the computations are simplified since the values of the exponential factor in the resolution function [Eq. (5.1)] at these points are fixed and do not vary with the setting ($\vec{Q}_0$, ω_0).

VI. RESULTS OF THREE-CRYSTAL MEASUREMENTS

We have measured the neutron scattering from RbMnF$_3$ in the vicinity of the Néel point and have obtained the cross section as a function of wavevector and energy transfer. The data have been analyzed quantitatively, including resolution and sensitivity effects.

Our results strongly support the concept of dynamic scaling and agree well with specific predictions of the theory. With this in mind, the experimental data will be presented and analyzed within the framework of dynamic scaling theory.

A. Dynamic Scaling

In a recent paper, [10] Halperin and Hohenberg proposed a generalization of the static-scaling laws to dynamic phenomena by making assumptions about

the behavior of time-dependent correlation functions near the critical point. Their theory leads to specific predictions for the case of the "isotropic" antiferromagnet, which is well represented in nature by RbMnF$_3$. They define a symmetrized space-time correlation function for the Hermitian operator $A(\vec{r}, t)$:

$$C^A(\vec{r}, t)$$
$$= \tfrac{1}{2} \langle \{[A(\vec{r}, t) - \langle A(\vec{r}, t) \rangle], \; [A(0, 0) - \langle A(0, 0) \rangle]\} \rangle, \quad (6.1)$$

where the angular bracket is an equilibrium expectation value and the curly bracket is an anticommutator. The Fourier transform is then written for wave vector $\vec{q}$, frequency ω, and inverse range parameter κ, in the general form

$$C_\kappa^A(\vec{q}, \omega) = \frac{2\pi}{\omega_\kappa^A(\vec{q})} \; C_\kappa^A(\vec{q}) f_{\vec{q},\kappa}^A (\omega/\omega_\kappa^A(\vec{q})), \quad (6.2)$$

where

$$C_\kappa^A(\vec{q}) = \frac{1}{2\pi} \int_{-\infty}^{\infty} d\omega \, C_\kappa^A(\vec{q}, \omega) \quad (6.3)$$

and

$$\frac{1}{\omega_\kappa^A(\vec{q})} \int_{-\omega_\kappa^A(\vec{q})}^{\omega_\kappa^A(\vec{q})} d\omega f_{\vec{q},\kappa}^A (\omega/\omega_\kappa^A(\vec{q})) = \tfrac{1}{2}. \quad (6.4)$$

The dynamic-scaling assumptions are the following: (i) that the characteristic frequency[26] $\omega_\kappa(\vec{q})$ is a homogeneous function of q and κ,

$$\omega_\kappa(\vec{q}) = q^E \Omega(q/\kappa), \quad (6.5)$$

and (ii) that the form of the frequency-dependent function $f_{\vec{q},\kappa}$ depends only on the ratio q/κ and not on $\vec{q}$ and κ separately.

Note that $C_\kappa(\vec{q}, \omega)$ is related to the wavelength-dependent susceptibility by the expression[27]

$$\chi(\vec{q}) T = \text{const} \times \int d\omega \, \frac{2kT}{\hbar\omega} \, \coth\left(\frac{\hbar\omega}{2kT}\right) C_\kappa(\vec{q}, \omega), \quad (6.6)$$

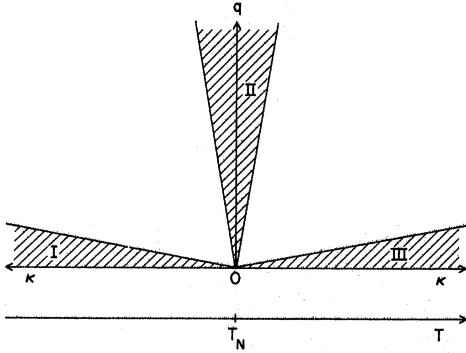which becomes, on expanding up to second order in $\hbar\omega/kT$,

FIG. 12. Representation of limiting regions in the q-κ plane where the correlation functions have different characteristic behaviors.

$$\chi(\vec{q})T = \text{const} \times \int d\omega \, C_\kappa(\vec{q}, \omega)\left[1 - \frac{1}{12}\left(\frac{\hbar\omega}{kT}\right)^2\!\!/4 \dots\right].$$

$$(6.7)$$

Therefore, owing to the fact that the condition $\hbar\omega/kT \ll 1$ is well satisfied by all our observed inelasticities, we shall make use throughout the paper of the identification

$$\chi(\vec{q})T \approx \text{const} \times C_\kappa(\vec{q}).$$ $$(6.8)$$

The scattering is conveniently discussed in terms of three limiting regions of the q-κ plane (Fig. 12). Following Halperin and Hohenberg we designate by region I the macroscopic region of the ordered phase, for which $q \ll \kappa$ and $T < T_N$. The corresponding macroscopic region for $T > T_N$ in which $q \ll \kappa$ is denoted by III. These regions refer to phenomena occurring over distances large compared to the correlation length κ^{-1}. The region in which $q \gg \kappa$ and either $T \lesssim T_N$ or $T \gtrsim T_N$ is labelled II and has been referred to by these authors, in a restricted sense, as the "critical" region to distinguish it from the macroscopic or "hydrodynamic" regions I and III. Region II is the domain of phenomena with which are associated distances or wavelengths that are small compared with the correlation length κ^{-1} but large compared to all the other relevant lengths such as the lattice parameters. For values of q and κ located on an arbitrary line passing through the origin in the q-κ plane, $f_{q,\kappa}$ is a fixed function of the normalized frequency $\omega/\omega_\kappa(\vec{q})$. Thus, except for scale, the energy-dependent cross sections for such points should all have the same shape.

The dynamic-scaling assumptions can be used to relate the behavior of the correlation function in the "critical" region to that in the "hydrodynamic" regions above and below the critical point. The characteristic frequency in the "hydrodynamic" region below T_N (region I) can be shown[28] to have the

behavior

$$\omega_\kappa(\vec{q}) = cq \propto \kappa^{1/2}q.$$ $$(6.9)$$

The exponent E in Eq. (6.5) is thus 1.5. In region II, where $\Omega(q/\kappa)$ is a finite nonzero constant, the characteristic frequency must therefore be proportional to $q^{1.5}$. In region III, the correlation function is peaked about $\omega = 0$ with an energy width which is nonzero at $q = 0$ since the staggered magnetization is not a constant of the motion. The characteristic frequency in this region, which can be rewritten in the form $\kappa^{1.5} \Omega'(q/\kappa)$, is then expected to vary as $\kappa^{1.5}$ for $q = 0$ since, from the foregoing, $\Omega'(q/\kappa)$ has a nonzero limit for $q \to 0$.

The use of a symmetrized space-time correlation function introduces the thermal factor $2(1 + e^{-\hbar\omega/kT})^{-1}$ in the equation for the cross section.[27] In terms of this form of the correlation function, Eq. (2.1) becomes

$$\frac{d^2\sigma}{d\Omega dE_f}(\vec{q}, \omega) \propto \frac{k_f}{k_i}\,|f(\vec{Q})|^2\,\frac{2}{1 + e^{-\hbar\omega/kT}}\,C_\kappa(\vec{q}, \omega).$$

$$(6.10)$$

B. "Critical" Region

At $T = T_N$ and for values of q greater than about 0.1 Å^{-1}, where resolution corrections are small, the observed uncorrected energy spectra of scattered neutrons exhibit three unresolved peaks. We have chosen, therefore, to analyze the data at T_N for all q in terms of the dynamic correlation function

$$C_{\kappa=0}(\vec{q}, \omega)$$

$$\propto \frac{A}{q^{2-\eta}}\left(\frac{\Gamma_1}{\Gamma_1^2 + \omega^2} + \frac{B\Gamma_2}{\Gamma_2^2 + (\omega + \omega_s)^2} + \frac{B\Gamma_2}{\Gamma_2^2 + (\omega - \omega_s)^2}\right),$$

$$(6.11)$$

where $A/q^{2-\eta}$ is the static part, B is a constant which determines the ratio of the central peak height to that of the sideband, Γ_1 and Γ_2 are the widths of the central peak and sideband, respectively, and ω_s is the displacement of the sideband peak from the center. In order to satisfy the assumption of dynamic scaling, the widths Γ_1, Γ_2, and ω_s are taken to be proportional to the characteristic frequency $\omega_\kappa(\vec{q})$, which in region II is given by q^E, with proportionality constants C, G, and D, respectively. (All frequencies are expressed in units of meV.)

We have performed measurements at an incoming neutron energy of 13.0 meV over a range of q extending from 0.05 to 0.25 Å^{-1}. Inserting the form (6.11) for the correlation function into the expression for the cross section, and using $\eta = 0.055$ as determined from two-crystal data, we have performed least-squares fits of the convoluted cross section to the data collected over the *restricted*

TABLE VI. Least-squares fit of data at T_N with $D = 16.0$[a] and $E = 1.4$.

q (Å^{-1})	t^b (min)	A	A/t	B	G[a]	C[a]	Residue
0.11	7.0	1.50 ± 0.20	0.214	1.62 ± 0.28	9.90 ± 0.28	5.56 ± 1.08	1.18
0.15	7.0	1.38 ± 0.19	0.197	2.05 ± 0.34	10.37 ± 0.42	4.73 ± 0.92	1.24
0.20	14.0	2.90 ± 0.42	0.207	1.90 ± 0.35	9.79 ± 0.46	5.15 ± 0.98	1.50
0.25	28.0	6.20 ± 0.92	0.221	1.81 ± 0.35	9.19 ± 0.65	4.44 ± 0.84	2.84

[a]In units of meV Å$^{1.4}$.   [b]Counting time.

range, $0.11 \le q \le 0.25$. The observational error used in the program was that given by counting statistics. To increase sensitivity in the fit, D and E were held fixed and the other parameters A, B, C, and G were allowed to vary. The procedure was

FIG. 13. Calculated and observed intensities as a function of energy transfer at T_N for different momentum transfers q. Observed data taken with incoming neutron energy of 13 meV.

repeated over a range of D and E giving, as best values, the set $D = 16.0 \pm 2.0$ and $E = 1.4 \pm 0.1$. The exponent E agrees well with the value 1.5 predicted by dynamic-scaling theory. Table VI shows the fit obtained for the remaining parameters. The results suggest that a single set of parameters will represent the data quite well although the progressive increase of the residue appears to be a manifestation of the small-q limit of the dynamic-scaling hypothesis. The best values of the parameters are $B = 1.82$, $C = 5.00$, $G = 9.66$, $D = 16.0$, and $E = 1.4$. These values correspond to a characteristic frequency law in region II given by the expression

$$\omega_{K=0}(\vec{q}) = 16.0\, q^{1.4}\,. \tag{6.12}$$

The success of dynamic scaling can be seen most clearly in Fig. 13 which shows the full set of observed data taken at 13.0 meV together with calculated curves based on the best set of parameters. As can be seen from the scale in Fig. 13, there is a factor of 100 between the peak intensities for $q = 0.05$ and 0.25 Å^{-1}. This agreement has been obtained using a *single* normalization constant for *all* the calculated curves. The effect of resolution can be seen in Fig. 14 which shows both the cross section and the cross section convoluted with the resolution function for $q = 0.075$ Å^{-1}. The three-peaked

FIG. 14. Comparison of raw data for $q = 0.075$ Å^{-1} with the convoluted and unconvoluted cross section.

INCOMING ENERGY $E_i = 6.6$ meV

$q = 0.075$ Å^{-1}

$q = 0.05$ Å^{-1}

$q = 0.025$ Å^{-1}

NEUTRONS/6 min

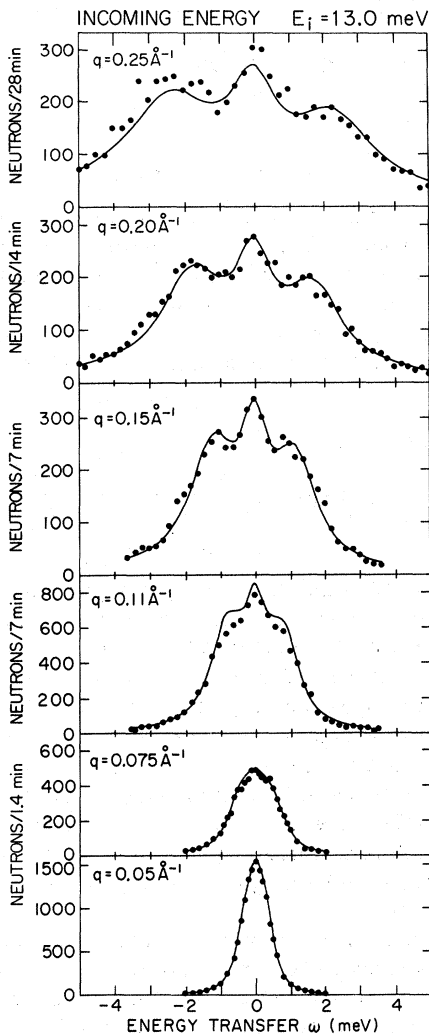ENERGY TRANSFER ω (meV)

FIG. 15. Calculated and observed intensities as a function of energy transfer at T_N for different momentum transfers q. Observed data taken with incoming neutron energy of 6.6 meV.
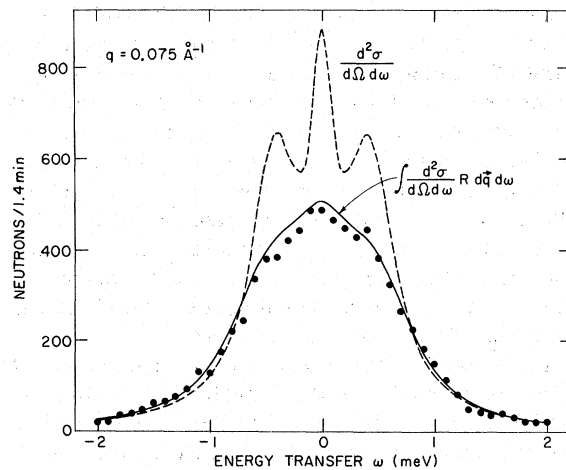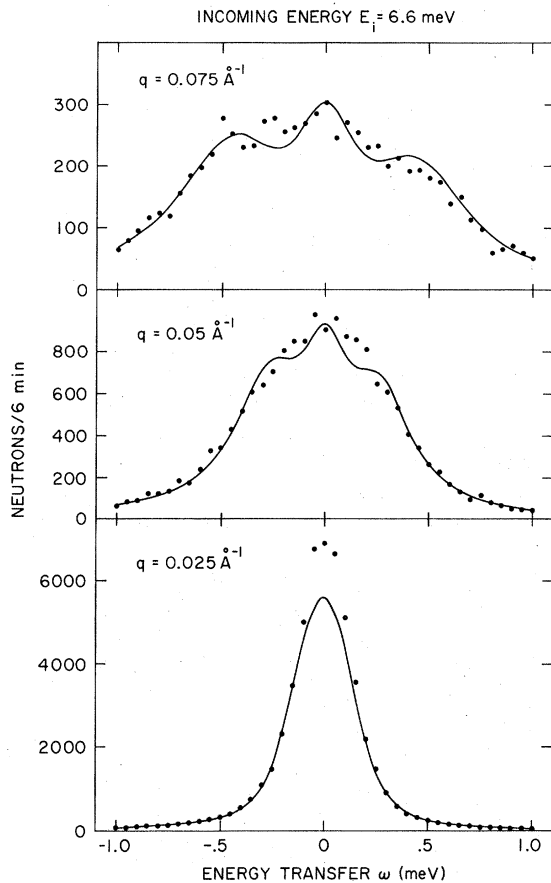
structure is largely obscured by the instrumental broadening at this low value of q; the characteristic frequency, however, is not greatly changed.

Comparisons of calculated and experimental curves have also been made, using the same values of the parameters except for the normalization contained in A, for high-resolution data (incoming neutron energy of 6.6 meV, Fig. 15) and for low-resolution data (incoming neutron energy of 47 meV, Fig. 16). The disagreement at zero energy transfer in the $q = 0.025$ data for $E_i = 6.6$ meV probably results from the difficulty of making precise resolution corrections when the cross section varies extremely rapidly with q and ω. Otherwise, the agreement is quite satisfactory and lends confidence to the method of treating resolution effects. The data taken at 47 meV have been extended further out in q since the available intensity is higher at this energy. Because of the low resolution it is impossible to detect structure in the peak at $q = 0.20$ whereas in the corresponding curve, taken at 13.0 meV, it is unmistakable. This structure becomes

more evident with increasing q in the case of the low-resolution data but at the same time the data depart progressively from the calculated curves. This disagreement at high q suggests that dynamic scaling fails beyond $q \sim 0.3$ Å^{-1}. This is not surprising inasmuch as the theory is expected to hold for q small compared to the magnetic zone-boundary value, which in this case is 0.64 Å^{-1}.

C. Hydrodynamic Region; $T > T_N$

A second test of dynamic scaling was made in the hydrodynamic region $(q \ll \kappa)$ above T_N, where $C_\kappa(\vec{q}, \omega)$ is assumed to have the "diffusion" form

$$C_\kappa(\vec{q}, \omega) \propto \frac{1}{(\kappa^2 + q^2)^{1 - \eta/2}} \quad \frac{\Gamma(\vec{q}, \kappa)}{\Gamma(\vec{q}, \kappa)^2 + \omega^2} \, . \quad (6.13)$$

As noted earlier, dynamic-scaling theory predicts that $\Gamma(\vec{q}, \kappa)$, the characteristic frequency, should vary as $\kappa^{1.5}$ for $q = 0$. In making a measurement at

INCOMING ENERGY $E_i = 47$ meV

$q = 0.5$ Å^{-1}

$q = 0.4$ Å^{-1}

$q = 0.3$ Å^{-1}

$q = 0.2$ Å^{-1}
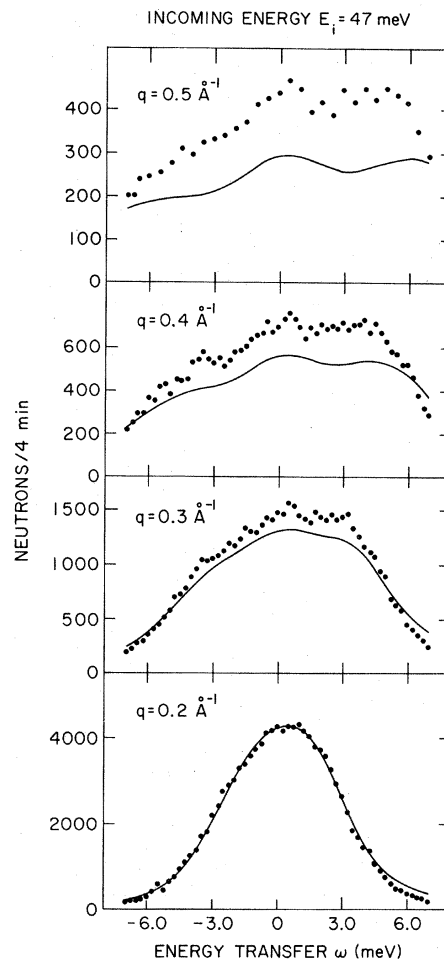
NEUTRONS/4 min

ENERGY TRANSFER ω (meV)

FIG. 16. Calculated and observed intensities as a function of energy transfer at T_N for different momentum transfers q. Observed intensities taken with incoming neutron energy of 47 meV.

a nominal setting of $q = 0$, nonzero values of q are simultaneously sampled because of finite instrumental resolution and hence the dependence of Γ on q is required in order to perform the convolution with the resolution function. To accord with the theory of dynamic scaling and the expected analyticity for $q = 0$, $\Gamma(\vec{q}, \kappa)$ has been taken to have the form

$$\Gamma(\vec{q}, \kappa) = \Gamma_0(\kappa) \, [1 + c\,(q/\kappa)^2], \qquad (6.14)$$

where $\Gamma_0(\kappa)$ is the characteristic frequency for $q = 0$. Least-squares analyses were performed using values of κ and η determined from two-crystal measurements. The procedure is relatively insensitive to the constant c and so this quantity was fixed in advance at 0.6 on the basis of a study of the dependence of the characteristic frequency on both q and κ outside the strictly hydrodynamic region, as explained below in Sec. VID. Figure 17 shows a typical least-squares fit from which $\Gamma_0(\kappa)$ is obtained at a given value of κ. The values so obtained were then fitted by weighted least squares using the expression

$$\Gamma_0 = d\kappa^E. \qquad (6.15)$$

Figure 18 gives the observed $\Gamma_0(\kappa)$ in meV as a function of $\kappa^{1.46}$ together with the line drawn for the best values of d and E which are 12.8 ± 0.9 and 1.46 ± 0.13, respectively. The exponent E agrees well, within the estimated error, with the predicted

FIG. 18. Plot of $\Gamma_0(\kappa)$, the characteristic frequency at $q = 0$, as a function of $\kappa^{1.46}$. Line corresponds to $\Gamma_0(\kappa) = d\kappa^E$ for the best values of d and E, which are 12.8 and 1.46.

value of 1.5. As the Néel point is approached, κ decreases and the q values sampled by the instrument no longer satisfy the hydrodynamic condition $q \ll \kappa$. This introduces a limitation on the range of temperatures in which useful data can be collected and explains the absence of data points in Fig. 18 between $T_N = 83\,°$K and the first point shown, which was obtained at $87\,°$K.

Theoretical estimates of $\Gamma(\vec{q}, \kappa)$ in the hydrodynamic region have been made by Huber and Krueger, [12] who have computed the coefficients in Eqs. (6.14) and (6.15) with exponent E equal to 1.5. They find $c = 0.91$ and give values for the parameter d in Eq. (6.15) ranging from 13.0 to 14.3. These may be compared with our values, $c = 0.6 \pm 0.3$, which is the result of our analysis of general frequencies in the q-κ plane, discussed in Sec. VID, and $d = 12.8 \pm 0.9$, coming from the treatment of the hydrodynamic data.

D. Characteristic Frequency for General Values of q and κ

According to dynamic-scaling theory the shape of the frequency spectrum is completely determined by the ratio q/κ. In Secs. VIB and VIC, we have considered the behavior in the q-κ plane along the $\kappa = 0$ axis (region II) and the $q = 0$ axis (region III). The latter case is characterized by a single-peaked frequency spectrum, whereas the former exhibits a three-peaked function. In between these two extremes, the shape changes slowly as the ratio of q
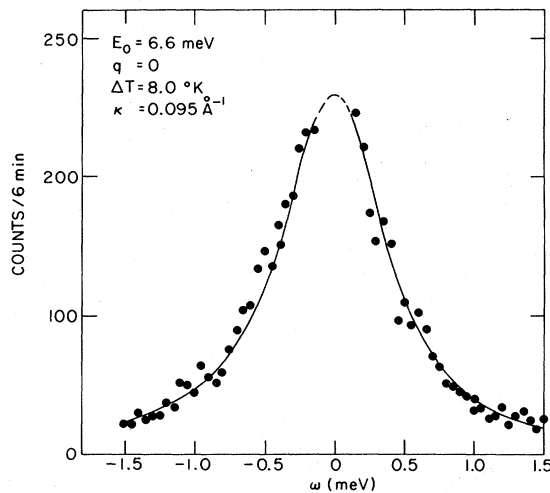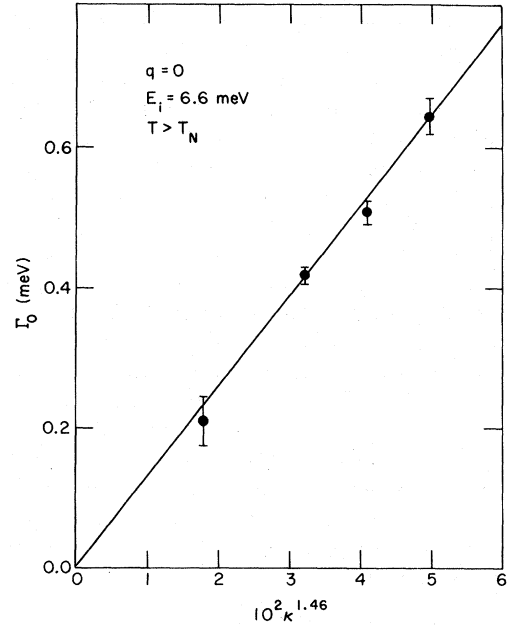

FIG. 17. Typical fit of calculated and observed intensities, for $q = 0$ and $\Delta T = 8\,°$K. Data have been corrected for the energy dependence of the analyzer reflectivity and counter sensitivity and the solid curve is a convolution of the cross section [Eq. (6.10)] with the resolution function, using Eq. (6.13) and the best value of Γ_0. Central points have been deleted because of the interference of a weak nuclear reflection coming from a higher-order contamination.

to κ is changed. We have not attempted to determine the shape of the frequency spectrum as a function of the ratio q/κ, but have obtained characteristic frequencies for general points in the q-κ plane. These have been used to test directly the first assumption of dynamic scaling; namely, that the characteristic frequency is a homogeneous function of q and κ [Eq. (6.5)].

Characteristic frequencies, as defined by Eq. (6.4), have been calculated from uncorrected data by direct integration. The data used consisted of 43 points for which the resolution corrections were negligible. (All the $q = 0$ data, for example, were thus excluded.) In this connection, it should be noted that whereas the resolution function may greatly alter the shape of a given frequency spectrum, the characteristic frequency is much less affected. Following Halperin and Hohenberg, [10] we assumed a simple homogeneous form for the characteristic frequency

$$\omega_\kappa(\vec{q}) = (aq^6 + bq^4\kappa^2 + c'q^2\kappa^4 + d'\kappa^6)^{E/6}, \qquad (6.16)$$

where a, b, c', d', and E are constants. The fit to experimental data is very insensitive to the value of d' because of the omission of the $q = 0$ data. Hence the fit of data points to Eq. (6.16) was carried out by the iterative procedure explained below, involving values d' obtained from an analysis of the $q = 0$ intensities by the method Sec. VIC.

For small q/κ, Eq. (6.16) has the expansion

$$\omega_\kappa(\vec{q}) = d'^{E/6}\kappa^E \left[1 + \frac{E}{6} \frac{c'}{d'} \left(\frac{q}{\kappa}\right)^2 + \cdots \right], \qquad (6.17)$$

where, referring to Eqs. (6.14) and (6.15), $d'^{E/6} = d$ and $\frac{1}{6}Ec'/d' = c$. Estimating a value of c from the q dependence of the uncorrected frequency spectra, a preliminary value of d was obtained from the analysis of the $q = 0$ intensities. The constant d' was obtained from d and inserted in Eq. (6.16). The remaining four constants in Eq. (6.16) were evaluated by least squares and a new value of c was thus obtained for insertion into Eq. (6.14) for the $q = 0$ analysis. This procedure was repeated and found to converge satisfactorily with values of $c = 0.6$ and $d = 12.8$ ($d' = 3.47 \times 10^4$). With $d' = 3.47 \times 10^4$, the least-squares values for the remaining constants in Eq. (6.15) are: $E = 1.37 \pm 0.03$, $a = (6.4 \pm 0.5) \times 10^4$, $b = -(0.95 \pm 0.38) \times 10^5$, $c' = (0.86 \pm 0.46) \times 10^5$, where the errors are based solely on counting statistics and do not take into account the neglect of resolution corrections. Figure 19 shows calculated and observed characteristic frequencies. The four uncorrected characteristic frequencies at $q = 0.10$ Å^{-1} and 6.6 meV which were thought to be subject to larger errors because of incomplete data in the wings, were omitted from the least-squares fit but have been added to the figure. In addition, we have added the resolution-corrected $q = 0$ data, making

a total of 51 characteristic frequencies.

Expanding Eq. (6.16) for $q \gg \kappa$, gives the expression $\omega_\kappa(q) = a' q^{1.37} + \cdots$ for region II, with $a' = a^{1.37/6} = 12.5$ from the above analysis. This may be compared with the result of the Néel point analysis discussed in Sec. VIB. To make the comparison we adjust the proportionality constant in (6.12) to take into account the small change in exponent from 1.4 to 1.37 and obtain $a' = 15.0$.

The zero-degree homogeneous function $f(\kappa/q) = \omega_\kappa(q)/\omega_0(\vec{q})$ has been calculated by Résibois and Piette[11] starting from the kinetic equations obtained by De Leener and Résibois.[29] In Fig. 20, we compare their result directly with our experimental values for f. For larger values of κ/q we have included points (open circles) obtained from the $q = 0.025\,\text{Å}^{-1}$ data, in spite of the relatively large uncertainty arising from contamination by higher-order neutrons as indicated in Sec. VIB. The agreement between theory and experiment is excellent over the entire range and even at large values of κ/q there is no discrepancy within the errors. The experimental points $\omega_\kappa(\vec{q})/\omega_0(\vec{q})$ were obtained from the observed values shown in Fig. 19, using pairs of frequencies corresponding to the same neutron incoming energy. The $q = 0.025\,\text{Å}^{-1}$ data for smaller κ/q have been omitted because the uncertainty in f becomes progressively worse as κ/q decreases. The $q = 0.10$ Å^{-1} data were also omitted for reasons given previously in the discussion of Fig. 19.
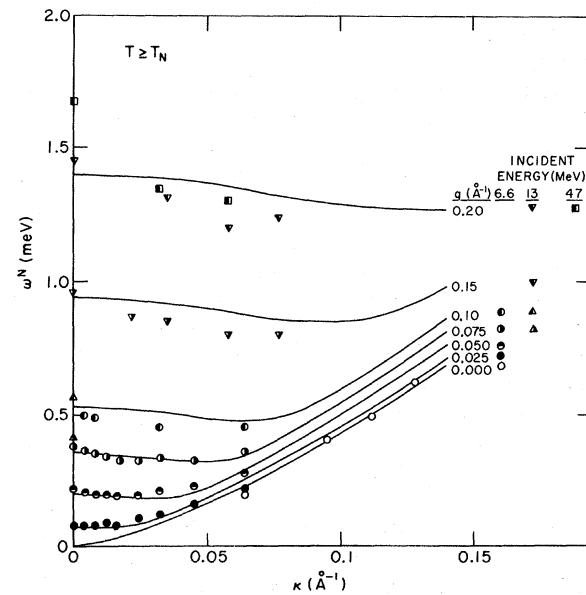

FIG. 19. Comparison of observed and calculated characteristic frequencies $\omega_\kappa(\vec{q})$ for $T \geq T_N$. Observed frequencies are half-area values, uncorrected for resolution, and are labeled by different symbols according to momentum transfer and incident neutron energy. Calculated curves are labeled according to the value of q.
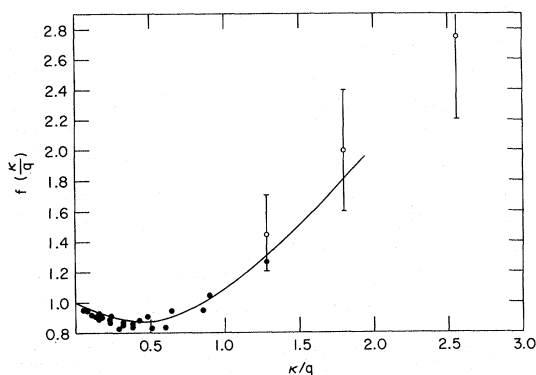
FIG. 20. Plot of the dependence of $\omega_\kappa(\vec{q})/\omega_0(\vec{q})$ on κ/q. Solid line represents the calculation of Résibois and Piette (Ref. 22). Open circles are derived from the $q = 0.025$ Å^{-1} data and have relatively large uncertainties (see text) compared to the solid points obtained from data at higher q values.

The results of this section can be used to investigate the progressive breakdown of the hydrodynamic (Lorentzian) form for the cross section above T_N with increase in the ratio q/κ. In the case of a Lorentzian distribution, the half-half-width is by definition the characteristic frequency and thus the correlation function (6.13) can be computed for general values of q and κ using the $\omega_\kappa(\vec{q})$ values given by Eq. (6.16). The suitability of the Lorentzian form for the energy dependence can thus be tested without at the same time treating the half-width as an adjustable parameter which can artificially improve the agreement. Figure 21 shows a comparison of computed curves and experimental data for $q = 0$ at different temperatures. In comparing with experiment, Eq. (6.13) has been convoluted with the resolution function. The agreement is entirely satisfactory and is to be expected on the basis of the discussion in Sec. VI C. Figure 22, on the other hand, shows the gradual failure of the agreement for increasing values of q/κ. In Fig. 21, the central points have been deleted because of the interference of a weak nuclear reflection coming from a higher-order wavelength contamination. This interference is not present in the data of Fig. 22 where q is different from zero.

E. Inverse Range Parameter for $T < T_N$

Two-crystal data can be satisfactorily interpreted, as we have seen, to give the inverse range parameter κ and temperature index ν above T_N. The corresponding analysis for $T < T_N$ is difficult to carry out, largely because of the interference of the Bragg magnetic peak. The index ν' for $T < T_N$ can, however, be determined indirectly from three-crystal data using the hydrodynamic analysis of Halperin and Hohenberg.[28] They find, in the long-wavelength

limit, that the characteristic frequency, which is one-half the energy separating the spin-wave peaks, is given by Eq. (6.9). The constant c appearing in this equation was determined directly from the uncorrected dispersion curve inasmuch as trial convolutions of the spin-wave cross section with the resolution function did not appreciably alter the position of the spin-wave peaks. A log-log plot of c against $T_N - T$ gives ν' as shown in Fig. 23. The least-squares value for the slope ν', determined for the range $0 < T_N - T < 6°$ is 0.54 ± 0.03. The line drawn in Fig. 23 corresponds to this fit but passes through the remaining points as well. The fit for the entire range $0 < T_N - T < 21°$ gives, in fact, $\nu' = 0.534 \pm 0.014$. The value $\nu' = 0.54 \pm 0.03$ appears to be significantly lower than the value $\nu = 0.701$
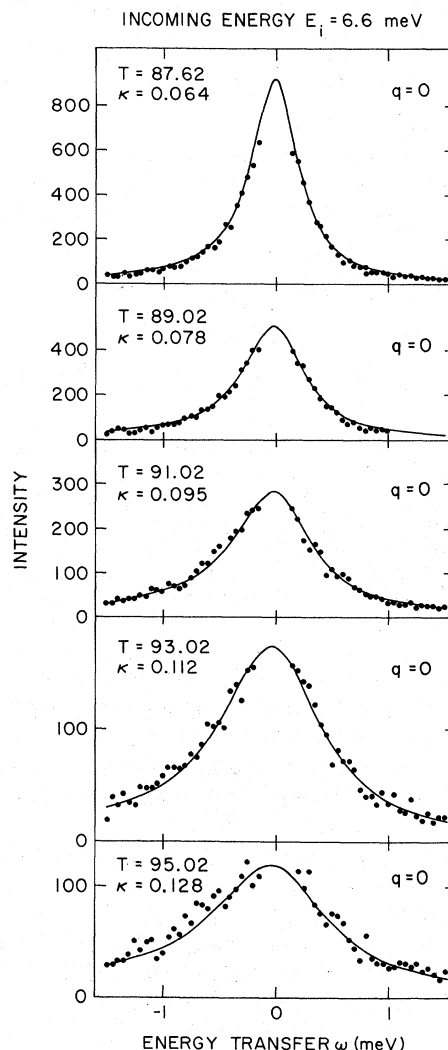
INCOMING ENERGY E$_i$ = 6.6 meV

FIG. 21. Calculated and observed intensities as a function of energy transfer at $q = 0$ for different temperatures above T_N. Observed intensities are in counts per 6 min of time and refer to an incoming neutron energy of 6.6 meV.
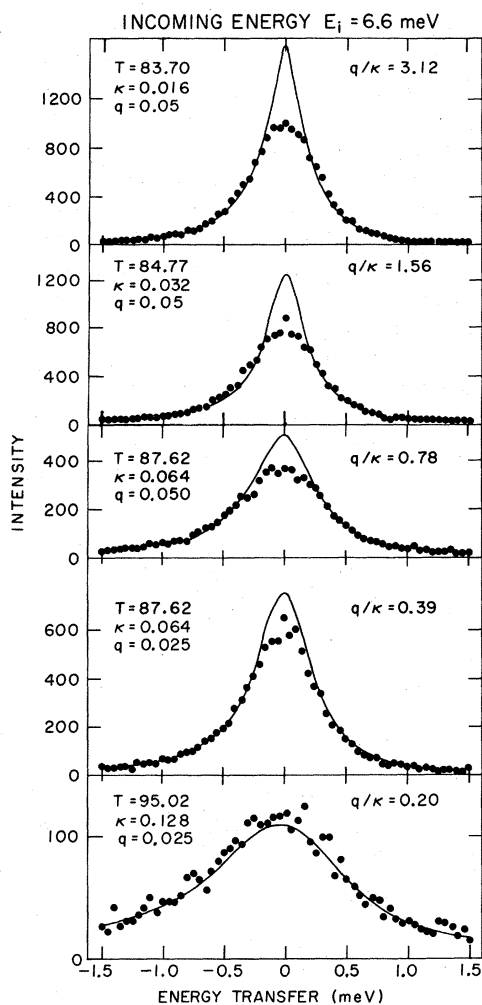
FIG. 22. Calculated and observed intensities as a function of energy transfer showing progressive failure of the hydrodynamic (Lorentzian) form for the cross section with increasing q/κ. Incoming neutron energy 6.6 meV; intensities in counts per six minutes of time.

± 0.011 obtained for $T > T_N$. A recent calculation by Helm[30] for the Ising model and the simple cubic lattice gives $\nu' = 0.50$ and $\nu = 0.78$.

VII. APPROXIMATION METHODS FOR TWO-CRYSTAL INELASTIC SCATTERING; ANALYSIS OF QUASIELASTIC APPROXIMATION

In the interpretation of the two-crystal data described in Sec. IV, use has been made of the quasi-elastic approximation. Because of the quantitative character of the information we wish to extract from the data, we examine in this section the general problem of the interpretation of two-crystal inelastic scattering and furnish estimates of the inelasticity corrections in the case of $RbMnF_3$.

A. Case of Perfect Resolution

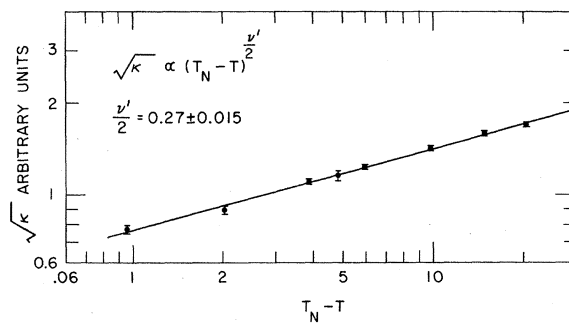We discuss here the case of perfect resolution,

FIG. 23. Log-log plot of $\sqrt{\kappa}$ vs $T_N - T$. Solid line is the result of least-squares analysis carried out using the five data points within the temperature range of 6 deg from T_N.

for which the analysis is simpler. A number of conclusions of a general nature are obtained, which are not substantially altered by finite resolution.

1. Formulation

Figure 24 shows a schematic diagram of the scattering geometry in reciprocal space for a two-crystal scattering arrangement. Since we are considering the case of perfect resolution, the only neutrons which are detected are those scattered through the
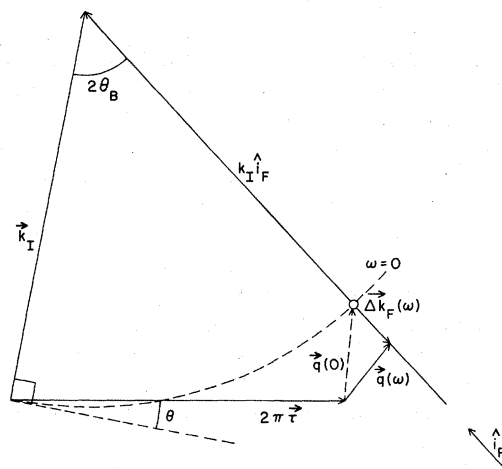
FIG. 24. Schematic diagram of the scattering geometry in reciprocal space for two-crystal inelastic scattering with perfect resolution. A process is represented which involves a definite energy transfer from the neutron to the sample. $\vec{k}_I$ is the wave vector of the incident neutrons and $\hat{i}_F$ is the direction of the scattered neutrons. All neutrons scattered in the direction $\hat{i}_F$ are detected. To every value of the energy transfer $\hbar\omega$ there corresponds a definite value of the final wave vector $\vec{k}_F$, determined by the conservation law $\hbar\omega = (\hbar^2/2m)(k_I^2 - k_F^2)$. $\Delta\vec{k}_F(\omega)$ is defined by the relation $\vec{k}_F = k_I \hat{i}_F - \Delta\vec{k}_F$. $\vec{q}(\omega)$ is the corresponding wave vector transfer measured with respect to the reciprocal lattice spot $2\pi\vec{\tau}$; namely, $\vec{q}(\omega) = \vec{k}_I - \vec{k}_F(\omega) - 2\pi\vec{\tau}$.

fixed scattering angle $2\theta = 2\theta_B$. Let $\hat{i}_F$ denote the direction defined by this constant-2θ condition. If $\vec{k}_I$ is the wave vector of the neutrons incident on the sample, then to every value $\hbar\omega$ of the neutron-to-sample energy transfer there corresponds a definite value of the final wave vector $\vec{k}_F$ given by $\vec{k}_F(\omega) = \hat{i}_F(k_I^2 - 2m\omega/\hbar)^{1/2}$. The momentum transfer is defined by $\vec{Q}(\omega) = \vec{k}_I - \vec{k}_F(\omega)$ and we denote by $\vec{q}(\omega)$ the momentum transfer relative to the reciprocal lattice spot $2\pi\vec{\tau}$; that is, $\vec{q}(\omega) = \vec{Q}(\omega) - 2\pi\vec{\tau}$. If we substitute $\vec{k}_F(\omega)$, $\vec{Q}(\omega)$, $\vec{q}(\omega)$ into the differential scattering cross section (6.10), we obtain

$$\frac{d^2\sigma}{d\Omega\,d\omega}\,(q(\omega),\,\omega)$$

$$= \text{const} \times \frac{k_F(\omega)}{k_I}\,|f(\vec{Q}(\omega))|^2 \frac{1}{1+e^{-\hbar\omega/kT}}\,C_\kappa(\vec{q}(\omega),\,\omega)\,.$$

(7.1)

This equation gives, for any value of energy transfer, the differential cross section for neutrons scattered with constant scattering angle $2\theta = 2\theta_B$. Note that this "constant-angle" cross section becomes, in the limit $E_i \to \infty$, a constant-$\vec{Q}$ cross section $[\vec{Q} = \vec{Q}(0)]$ as a consequence of the relation

$$k_I - k_F(\omega) = k_I\hbar\omega/2E_i + \text{higher-order terms}\,. \quad (7.2)$$

The observed intensity is obtained by integration of (7.1) over final neutron energies; namely,

$$I(\vec{q}(0)) \propto \frac{d\sigma}{d\Omega}\,(\vec{q}(0)) = \int d\omega\,\frac{d^2\sigma}{d\Omega\,d\omega}\,(\vec{q}(\omega),\,\omega)$$

$$= \text{const} \times \int_{-\infty}^{(\hbar/2m)k_I^2} d\omega$$

$$\times \frac{k_F(\omega)}{k_I}\,|f(\vec{Q}(\omega))|^2\,\frac{1}{1+e^{-\hbar\omega/kT}}\,C_\kappa(\vec{q}(\omega),\,\omega)\,.$$

(7.3)

This equation is a line integral in reciprocal space along the radial path that has origin in $0'$ and passes through the point $\vec{q}(0)$. We then formulate the quasi-elastic approximation for the intensity by the statement

$$\frac{d\sigma}{d\Omega}\,(\vec{q}(0)) = \int d\omega\,\frac{d^2\sigma}{d\Omega\,d\omega}\,(\vec{q}(\omega),\,\omega) \approx \text{const} \times C_\kappa(\vec{q}(0))\,.$$

(7.4)

Sufficient conditions on $\hbar\omega$ under which this equation

holds can be given as follows: If $\hbar\omega$ is sufficiently small compared to E_i so that, using Eq. (7.2), the "static approximation" conditions

$$\vec{k}_F(\omega) \approx \vec{k}_I\,, \quad (7.5a)$$

$$\vec{Q}(\omega) \approx \vec{Q}(0)\,, \quad (7.5b)$$

and

$$\vec{q}(\omega) \approx \vec{q}(0) \quad (7.5c)$$

are satisfied; and furthermore, if

$$\hbar\omega \ll kT\,, \quad (7.6)$$

then it follows from Eq. (7.3) that

$$I(\vec{q}(0)) \approx \text{const} \times \int d\omega\,C_\kappa(\vec{q}(0),\,\omega) \quad (7.7)$$

and, using the sum rule (6.3), that

$$I(\vec{q}(0)) \approx \text{const} \times C_\kappa(\vec{q}(0))\,. \quad (7.8)$$

This is the quasielastic approximation as formulated in Eq. (7.4). Note that condition (7.6) is quite a weak requirement since $C(\vec{q},\,\omega)$ is even in ω, and thus it follows from (7.3) that corrections to the quasielastic approximation are of order higher than the first in $\hbar\omega/kT$. The same, however, cannot be said for the "static approximation" (7.5); while $Q(0)$ and k_I can easily be large compared to $\Delta k_F(\omega) = k_I - k_F(\omega)$, this is hardly true of $q(0)$. In fact, in the case of two-crystal measurements, the constant-$\vec{q}$ approximation (7.5c) is rarely satisfied, so that the applicability of Eq. (7.4) to the measurement of the static parameters κ, ν, and η requires further justification.

2. Quasielastic Approximation in Region II ($q \gg \kappa$)

a. Failure of constant-$\vec{q}$ approximation. We are going to make use of the dynamical properties of the cross section in region II, as determined in the three-crystal measurements, in order to calculate the energy-dependent "constant-angle" cross sections (7.1) and, using these, the corresponding line integrals (7.3). These calculations are carried out with experimental parameters E_i and $2\pi\tau$ appropriate to our two-crystal experiment. Using the results of Sec. VIB for region II ($\kappa = 0$ and hence $q/\kappa = \infty$), we write

$$C_{\kappa=0}(\vec{q},\,\omega) = C_0(\vec{q})\,\frac{1}{\omega_0(\vec{q})}\,f_\infty\left(\frac{\omega}{\omega_0(\vec{q})}\right) \propto \frac{A}{q^{2-\eta}}\left(\frac{Cq^{1.4}}{C^2q^{2.8}+\omega^2} + \frac{BGq^{1.4}}{G^2q^{2.8}+(\omega+Dq^{1.4})^2} + \frac{BGq^{1.4}}{G^2q^{2.8}+(\omega-Dq^{1.4})^2}\right)\,,$$

(7.9)

where $\eta = 0.055$, $B = 1.82$, $C = 5.00$, $G = 9.66$, $D = 16.0$; and, in addition, $E_i = 48.0$ meV and $2\pi\tau = 1.2876$ Å^{-1}. The computed line integrals will be

compared with $C_0(\vec{q}(0))$ to determine to what extent the quasielastic approximation (7.4) is satisfied in our two-crystal measurements in region II. It
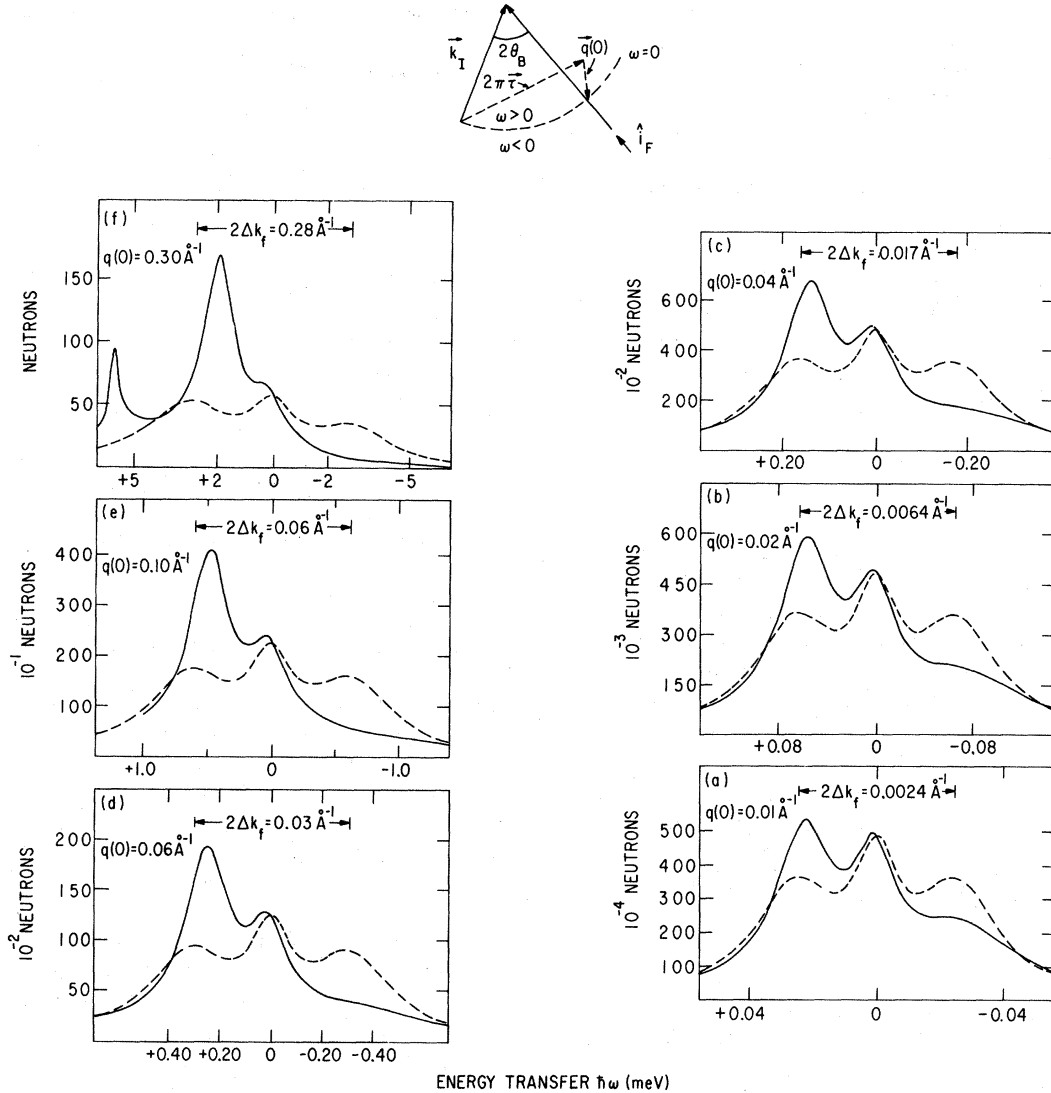
FIG. 25. Illustration of the failure of the constant-$\vec{q}$ approximation in a two-crystal ("constant-angle") experiment. Solid lines represent the "constant-angle" energy dependence of the cross section for the actual two-crystal experiment ($E_i = 48.0$ meV; $2\Delta k_f$ is the range of k_f covered over the indicated range of ω). Dashed lines show the corresponding energy dependence in the ideal case in which the constant-$\vec{q}$ requirement is satisfied; namely, in the limit $E_i \to \infty$. Two sets of curves are shown for several positive values of $q(0)$. A positive sign for $q(0)$ corresponds to the experimental arrangement shown at the top of the figure; namely, with the reciprocal lattice spot lying inside the $\omega = 0$ sphere.

should be noted (see Fig. 24) that the same value of $|\vec{q}(0)|$ can be obtained for two symmetric positions of $2\pi\vec{\tau}$ relative to the Bragg position $\theta = \theta_B$. We shall distinguish them by labelling as $- |q(0)|$, the arrangement in which the reciprocal lattice spot lies outside the $\omega = 0$ sphere, and as $+ |q(0)|$, the opposite one. With this convention, the calculated line integrals $d\sigma/d\Omega$ are functions $(d\sigma/d\Omega)(q(0))$, where $q(0)$ ranges from negative to positive values. The above distinction is necessary when discussing the quasielastic approximation because, for the calculated line integrals, one obviously has, in

general,

$$\frac{d\sigma}{d\Omega}\left(q(0)\right) \neq \frac{d\sigma}{d\Omega}\left(-q(0)\right) .$$

The first result of these calculations is that the "static" conditions (7.5), introduced in the preceding section to derive the quasielastic cross section, are far from fulfilled. This is shown in Fig. 25. The solid lines represent the "constant-angle" energy dependence of the cross section for the parameters used in the actual two-crystal experiment. The dashed lines show the corresponding energy
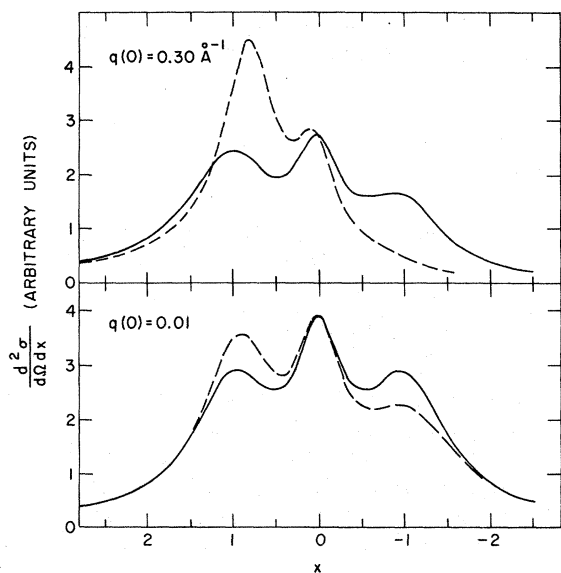
FIG. 26. Illustration of the "energy-averaging" mechanism, discussed in the text, compensating for the failure of the constant-$\vec{q}$ approximation. Plots represent the "constant-angle" cross sections $d^2\sigma/d\Omega\,dx$ defined by the relation $\int d\omega\, d^2\sigma/d\Omega d\omega = \int dx\, d^2\sigma/d\Omega\, dx$, where x is the variable defined by Eq. (7.11). Solid lines are calculated cross sections for the parameters used in the actual two-crystal experiment ($E_i = 48.0$ meV), while the dashed lines correspond to the ideal case in which the constant-q requirement is satisfied; namely, the limit $E_i \to \infty$. Difference in the areas under the solid and dashed curves is 1.6% for $q(0) = 0.01$ Å^{-1}, and 18% for $q(0) = 0.30$ Å^{-1}.

dependence in the limit $E_i \to \infty$, in which case the "static" conditions are obviously satisfied. Comparison of the paired curves shows that under the conditions of the actual experiment the "static approximation" breaks down. That this should be so in the present case, as in most two-crystal experiments, is apparent from the magnitudes of Δk_f, the "k inelasticity" of the scattering in reciprocal space. Δk_f can be estimated from Eq. (7.2) by replacing ω with the characteristic frequency $\omega_0(\vec{q}(0))$, giving

$$\Delta k_f \approx k_I\, \hbar\omega_0(\vec{q}(0))/2E_i \ . \qquad (7.10)$$

Thus one can see that the condition $\vec{q}(\omega) \approx \vec{q}(0)$ is hardly satisfied even for the most favorable case $[q(0) = 0.01$ Å$^{-1}]$ represented in Fig. 25, where $\Delta k_f = 0.0012$. Therefore, the breakdown of the "static" approximation actually is brought about by the failure of the constant-$\vec{q}$ condition (7.5c). In spite of this failure, however, the quasielastic approximation (7.4) remains satisfactory for many two-crystal experiments because of the existence of certain compensating mechanisms which are discussed below.

b. "Energy-averaging" mechanism compen-

sating for failure of constant-$\vec{q}$ condition. The quantity measured in the two-crystal experiment is the area under the curves in Fig. 25. If one compares the area under the "constant-angle" cross sections to the area under the corresponding constant-$\vec{Q}$ cross sections, one finds that a mechanism of compensation is operative, which tends to balance the discrepancy for $\hbar\omega > 0$ against that for $\hbar\omega < 0$. Further insight into the origin of the above mechanism is gained by introducing in the integration (7.3) the new dimensionless variable x, defined by the differential relation

$$dx = \frac{1}{\omega_0(\vec{q}(\omega))}\ d\omega \ . \qquad (7.11)$$

The characteristic property of the new variable thus defined is that equal intervals dx correspond to different energy intervals $d\omega$, depending on the point where they occur on the energy axis. Specifically, these intervals $d\omega$ are proportional to the width $\omega_0(\vec{q}(\omega))$ assigned to the shape function f_∞ at that point. Note that in general $x \neq \omega/\omega_0(\vec{q}(\omega))$ because ω_0 is not constant. In fact, by logarithmic differentiation of $\omega/\omega_0(\vec{q}(\omega))$ one obtains

$$d[\omega/\omega_0(\vec{q}(\omega))] - dx = - \frac{\omega}{\omega_0(\vec{q}(\omega))}\, d\ln\omega_0(\vec{q}(\omega))$$

$$\propto - \frac{\omega}{\omega_0(\vec{q}(\omega))}\ \frac{dq(\omega)}{q(\omega)} \quad . \qquad (7.12)$$

After changing variable in Eq. (7.3), the resulting integrands can be plotted as a function of x, and we obtain the curves of Fig. 26 for the two extreme cases $q(0) = 0.01$ and 0.30 Å^{-1}. Comparing constant-angle and constant-$\vec{Q}$ cross sections in Fig. 26, we see that the over-all area compensation results from a point-by-point compensation of equal and opposite contributions at $+x$, and $-x$. The difference in the two areas is only 1.6% in the $q(0) = 0.01$ Å^{-1} example and does not exceed 18% even in the extreme case $q(0) = 0.30$ Å^{-1}. The mechanism illustrated above by direct computation for the case of our particular experiment, actually arises from a general property of the integrand. In what follows, we present an analytical formulation of this property, leading to the definition of a parameter for estimating the inelasticity corrections to the quasielastic approximation.

Assuming for simplicity that, among the conditions (7.5) and (7.6), only the requirement $\vec{q}(\omega) \approx \vec{q}(0)$ is not met, we obtain from Eq. (7.3)

$$\frac{d\sigma}{d\Omega}\ (q(0)) \propto \int d\omega\ C_0(\vec{q}(\omega))\ \frac{1}{\omega_0(\vec{q}(\omega))}\ f_\infty\!\left(\frac{\omega}{\omega_0(\vec{q}(\omega))}\right) \ .$$

$$(7.13)$$

A measure of the difference between $\vec{q}(\omega)$ and $q(0)$ is given by Δk_f, the "k inelasticity" of the scattering in reciprocal space defined in Eq. (7.10). The

percentage difference of the integrand of (7.13) from its constant-$\vec{q}$ value is, in region II, proportional to

$$\varepsilon = \Delta k_f / q(0) \qquad (7.14)$$

and this is therefore a convenient parameter in terms of which to study the deviations from the "static approximation." Using Eq. (7.10), ε is given by

$$\varepsilon = \frac{m}{\hbar^2 k_I} \left(\frac{\hbar \omega_0(\vec{q}(0))}{q(0)} \right) . \qquad (7.15)$$

Since $\varepsilon = 0$ corresponds to the "static approximation," one has, setting $\vec{q}(\omega) = \vec{q}(0)$ in (7.11),

$$\omega = \omega_0(\vec{q}(0)) x . \qquad (7.16)$$

For general ε, Eq. (7.11) implicitly defines the change of variable, $\omega \to x$, as an ε-dependent transformation, because $q(\omega) - q(0)$ is a function of ε; thus, effectively, one has

$$\omega = \omega(x, \varepsilon) . \qquad (7.17)$$

The ε dependence of $q(\omega) - q(0)$ for $\varepsilon \to 0$ can be easily obtained as follows: From Fig. 24, one sees that $q(\omega) - q(0) \approx [k_I - k_F(\omega)] \cos\theta_B$ and hence, using (7.2) together with (7.16), one finds

$$\frac{q(\omega) - q(0)}{q(0)} \sim \text{const} \times x\varepsilon \quad (\varepsilon \to 0). \qquad (7.18)$$

Applying this result to (7.12), one obtains

$$d[\omega/\omega_0(\vec{q}(\omega))] - dx \sim \text{const} \times x \, d(x\varepsilon) \quad (\varepsilon \to 0) . \qquad (7.19)$$

Let us now introduce the new variable x into Eq. (7.13) by means of the transformation defined by Eq. (7.11) and formally represented by (7.17). Expansion of the integrand of (7.13) at constant x around $\varepsilon = 0$ then yields

$$\frac{d\sigma}{d\Omega}(q(0))$$

$$\approx \text{const} \times \int_{-\infty}^{\infty} dx \, C_0(\vec{q}(0)) \left[1 + \left(\frac{\partial \ln C_0}{\partial \varepsilon} \right)_{\varepsilon = 0} \varepsilon + \cdots \right]$$

$$\times f_\infty(x) \left[1 + \left(\frac{\partial \ln f_\infty}{\partial \varepsilon} \right)_{\varepsilon = 0} \varepsilon + \cdots \right], \qquad (7.20)$$

where the values of f_∞ and C_0 at the point $\varepsilon = 0$ have been obtained using $\vec{q}(\omega) = \vec{q}(0)$ together with Eq. (7.16). The partial derivatives in Eq. (7.20) are functions of x. In fact, one can show that they are odd functions of x as follows:

$$\left(\frac{\partial \ln C_0}{\partial \varepsilon} \right)_{\varepsilon = 0} = \left(\frac{d \ln C_0(\vec{q}(\omega))}{d \ln q(\omega)} \frac{\partial \ln q(\omega)}{\partial \varepsilon} \right)_{\varepsilon = 0}$$

$$= \frac{d \ln C_0(\vec{q}(0))}{d \ln q(0)} \left(\frac{\partial \ln q(\omega)}{\partial \varepsilon} \right)_{\varepsilon = 0} \qquad (7.21a)$$

and

$$\left(\frac{\partial \ln f_\infty}{\partial \varepsilon} \right)_{\varepsilon = 0}$$

$$= \left(\frac{d \ln f_\infty[\omega/\omega_0(\vec{q}(\omega))]}{d[\omega/\omega_0(\vec{q}(\omega))]} \frac{\partial [\omega/\omega_0(\vec{q}(\omega))]}{\partial \varepsilon} \right)_{\varepsilon = 0}$$

$$= \frac{d \ln f_\infty(x)}{dx} \left(\frac{\partial [\omega/\omega_0(\vec{q}(\omega))]}{\partial \varepsilon} \right)_{\varepsilon = 0} . \qquad (7.21b)$$

Equation (7.21a) is odd in x by virtue of (7.18), since $d \ln C_0(\vec{q}(0))/d \ln q(0)$ is a constant. As for (7.21b), one finds that it too is odd because $f_\infty(x)$ is even in x and so is $\{\partial[\omega/\omega_0(q(\omega))]/\partial\varepsilon\}_{\varepsilon=0}$ according to Eq. (7.19). Thus, if one compares values of the integrand of Eq. (7.20) at $+x$ and $-x$, one finds that corrections to the constant-$\vec{Q}$ cross section, $f(x) C_0(\vec{q}(0))$, cancel each other up to first order in ε.

As a consequence of the above analysis, one finds that

$$\frac{d\sigma}{d\Omega}(q(0)) \propto 2 \int_0^\infty dx \, f_\infty(x) \, C_0(\vec{q}(0)) [1 + O(\varepsilon^2)]$$

$$= C_0(\vec{q}(0)) \left(1 + 2 \int_0^\infty dx \, f_\infty(x) \, O(\varepsilon^2) \right), \qquad (7.22)$$

and thus that the inelasticity corrections to the quasielastic cross section are in general of order ε^2; that is,

$$\varepsilon^2 = \frac{m}{2\hbar^2 E_i} \left(\frac{\hbar \omega_0(\vec{q}(0))}{q(0)} \right)^2 . \qquad (7.23)$$

This is a convenient parameter for estimating the validity of the quasielastic approximation. For the two cases shown in Fig. 26, the values of ε^2 are 0.016 for $q(0) = 0.01$ Å^{-1} and 0.25 for $q(0) = 0.30$ Å^{-1}.

In order to have a quantitative picture of the applicability of the quasielastic condition (7.4) in our two-crystal experiment, we have made explicit calculations of the cross sections, $(d\sigma/d\Omega)(-|q(0)|)$ and $(d\sigma/d\Omega)(+|q(0)|)$, namely, the areas under the solid-line curves of the type shown in Fig. 25, and compared them to their quasielastic values, $1/|q(0)|^{2-\eta}$ ($\eta = 0.055$) for the range 0.01 Å$^{-1} < |q(0)| < 0.31$ Å^{-1}. The result of this comparison is shown in Fig. 27 together with the Ornstein-Zernike form $1/|q(0)|^2$. Calling any of the above four functions I, what is, in fact, plotted is $\ln(|q(0)|^{2-\eta}I)$, with I normalized to a fixed value at $q(0) = -0.01$ Å^{-1}. In this plot the deviations between any pair of curves gives directly the percentage difference between the corresponding functions. The departure of $d\sigma/d\Omega$ from the quasielastic value is small over a wide
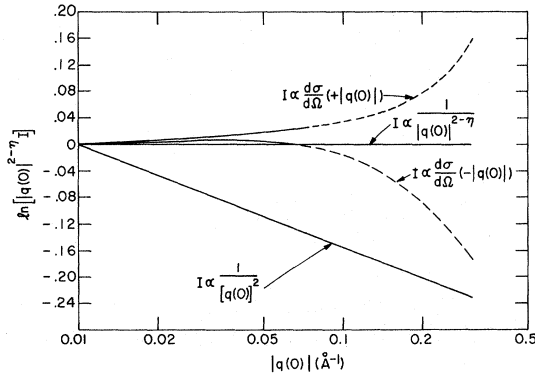
FIG. 27. Comparison of the two-crystal cross sections, $(d\sigma/d\Omega)[+|q(0)|]$ and $(d\sigma/d\Omega)[-|q(0)|]$, calculated using $\eta = 0.055$, with the quasielastic approximation to them, $1/|q(0)|^{2-\eta}$. In addition comparison is shown with the Ornstein-Zernike form $1/|q(0)|^2$. Calling any of the above four functions I, we have plotted $\ln[|q(0)|^{2-\eta}I]$, where I has been previously normalized to a fixed value at $q(0) = -0.01\,\text{Å}^{-1}$. In this plot the deviations between any pair of curves gives directly the percentage difference between the corresponding functions.

range of $|q(0)|$. Note, that if one wishes to determine η using the quasielastic approximation, the deviations of $d\sigma/d\Omega$ from the quasielastic value $1/|q(0)|^{2-\eta}$ must be small compared to $(1/|q(0)|^2 - 1/|q(0)|^{2-\eta})$. The curve for $I = 1/|q(0)|^2$ has been included in Fig. 27 to make this comparison possible. An important detail in Fig. 27 is that $(d\sigma/d\Omega) \times (+|q(0)|)$ and $(d\sigma/d\Omega)(-|q(0)|)$ are represented by solid lines, which go over into dashed lines for higher values of $|q(0)|$. Only a qualitative significance is to be attached to the curves over the range of $|q(0)|$ covered by the dashed lines. This caution is justified because, the larger $|q(0)|$ becomes, the greater is the inelasticity of the scattering and hence the larger is the range of q covered in the line

integration $d\sigma/d\Omega$. Going out in $|q(0)|$ thus brings us out of the range where either theoretical or experimental information on the dynamical properties of the cross section is available. In fact, we have verified that the line integrals do depend critically on such knowledge as the variation with q of the characteristic frequency $\omega_0(\vec{q})$. Therefore, when making actual use of calculated two-crystal cross sections in order to fit experimental two-crystal intensities (see Sec. VII B), we will restrict ourselves to the smaller $|q(0)|$ range covered by the solid lines in Fig. 27. The upper limit of this range has been conservatively set at $0.076\,\text{Å}^{-1}$. The range of q and ω which is involved in the line integration at $|q(0)| = 0.076\,\text{Å}^{-1}$ can be characterized in the following way: The line integral $\int d\omega\, d^2\sigma/d\Omega\, d\omega$ calculated between the $\hbar\omega$ limits -5.5 and $+5.5$ meV, converges to 99% of its total sum and the largest q in the above range is $0.35\,\text{Å}^{-1}$.

$c.$ *"q-averaging" mechanism compensating for failure of constant-$\vec{q}$ condition.* Inspection of Fig. 27 reveals immediately the presence of a second mechanism of compensation, in addition to the "energy-averaging" mechanism, which favors the quasielastic approximation. One sees there that, even though at higher values of $|q(0)|$ the *individual* constant-angle cross sections $(d\sigma/d\Omega)(+|q(0)|)$ and $(d\sigma/d\Omega)(-|q(0)|)$ differ appreciably from $1/|q(0)|^{2-\eta}$, nevertheless, the average values of each pair are consistently in very good agreement with the quasielastic cross section. This "q-averaging" mechanism results from a general property of the cross section and can be given the following analytic formulation. We have shown in the previous discussion that, if the integrand of Eq. (7.13) is expanded at constant x, around $\varepsilon = 0$, one finds that the coefficient of the first-order term is an odd function of x. If we denote this coefficient by $\mu(x)$, this equation can be rewritten as

$$\frac{d\sigma}{d\Omega}(q(0)) \propto \left[\frac{1}{2}C_0(\vec{q}(0))\left(1 + 2\int_0^\infty dx\, f_\infty(x)\,\mu(x)\,\varepsilon + \cdots\right)_{\omega>0} + \frac{1}{2}C_0(\vec{q}(0))\left(1 - 2\int_0^\infty dx\, f_\infty(x)\,\mu(x)\,\varepsilon + \cdots\right)_{\omega<0}\right].$$

$$(7.24)$$

In the previous discussion, the effect of the thermal factor was neglected. Inclusion of this factor up to first order in $\hbar\omega/kT$ yields

$$\frac{d\sigma}{d\Omega}(q(0)) \propto \left\{\frac{1}{2}C_0(\vec{q}(0))\left[\left(1 + 2\int_0^\infty dx\, f_\infty(x)\,\mu(x)\,\varepsilon + \cdots\right)(1 + \hbar\omega(x)/2kT + \cdots)\right]_{\omega>0}\right.$$

$$+ \frac{1}{2}C_0(\vec{q}(0))\left[\left(1 - 2\int_0^\infty dx\, f_\infty(x)\,\mu(x)\,\varepsilon + \cdots\right)(1 - \hbar|\omega(x)|/2kT + \cdots)\right]_{\omega<0}\right\}$$

$$= C_0(\vec{q}(0))\left(1 + \int_0^\infty dx\, f_\infty(x)\,\mu(x)\,\varepsilon\,\hbar|\omega(x)|/kT + \cdots\right),$$

$$(7.25)$$

where, as in the previous discussion, the term that is first order in ε and zeroth order in $\hbar\omega/kT$, drops out. Now, if we examine the "constant-angle" differential cross sections in a "$+|q(0)|$" arrangement, such as in Fig. 25, we note that the dominant contribution to the total area is shifted to the positive side ($\omega > 0$). This is due to the fact that, in a "$+|q(0)|$" arrangement, as ω runs from negative to positive values, $q(\omega)$ decreases in magnitude (see Fig. 24 and vector diagram in Fig. 25); this results in a corresponding enhancement of the positive side of the differential cross section and depression of the negative side because of the factor $1/(q(\omega))^{2-\eta}$ in the correlation function $C_0(\vec{q}(\omega))$. Thus, $\mu_{+|q(0)|}(x) > 0$. Exactly the opposite is true in the "$-|q(0)|$" arrangement; namely, the dominant contribution to the total area is shifted to the negative axis so that $\mu_{+|q(0)|}(x) = -\mu_{-|q(0)|}(x)$. Thus, one sees that on averaging $(d\sigma/d\Omega)(+|q(0)|)$ and $(d\sigma/d\Omega)(-|q(0)|)$ the leading correction term to the quasielastic cross section drops out. One can check by direct calculation that the thermal factor $1/(1 + e^{-\hbar\omega/kT})$ is the main source of the asymmetry between $+|q(0)|$ and $-|q(0)|$ which appears in Fig. 27. If the thermal factor is suppressed in the calculation, the difference between $(d\sigma/d\Omega)(+|q(0)|)$ and $(d\sigma/d\Omega)(-|q(0)|)$ drops from 33 to 6% at the largest value of $|q(0)|$, 0.31 Å^{-1}.

The immediate consequence of the averaging effect described above is that, if a least-squares fit of the calculated two-crystal intensities (Fig. 27) is carried out using the quasielastic cross section, the correct static correlation is obtained over the whole range, $|q(0)| \leq 0.31$ Å^{-1}, *provided both* "$+|q(0)|$" *and* "$-|q(0)|$" *intensities are simultaneously used in the fit.* Furthermore, Fig. 27 shows that the quasielastic approximation does not appreciably alter the value of η and that a cross section with $\eta = 0$ is clearly ruled out.

3. Quasielastic Approximation at a General Temperature

a. Compensation mechanisms for $T > T_N$. The analytical formulation of the two compensation mechanisms, which was carried out in the preceding section for the case of region II, can be easily extended to general temperatures by suitably generalizing the expansion parameter ε defined in Eq. (7.14). Renormalizing Δk_f by means of $q^*(\kappa)$ $= |q(0)|\,(1 + \kappa^2/|q(0)|^2)$ one obtains

$$\varepsilon^* = \Delta k_f / |q(0)| \,[1 + (\kappa/|q(0)|)^2] \,. \qquad (7.14')$$

The final result of this generalization can be summarized by the equation

$$\frac{1}{2}\left(\frac{d\sigma}{d\Omega}(+|q(0)|) + \frac{d\sigma}{d\Omega}(-|q(0)|)\right)$$

$$\propto C_\kappa(\vec{q}(0))\,[1 + O(\varepsilon^{*2}) + \cdots] \,. \qquad (7.26)$$

Thus, in general, the parameter that must be small compared to 1 in order for the quasielastic approximation to hold at a given instrumental setting $q(0)$ is

$$\varepsilon^{*2} = \frac{m}{2\hbar^2 E_i}\left(\frac{\hbar\omega_\kappa(\vec{q}(0))\,q(0)}{\kappa^2 + q^2(0)}\right)^2 \,. \qquad (7.27)$$

In a $q(0)$ scan at a given temperature, a representative value Γ_κ for the inelasticity of the scattering is the inelasticity associated with $q(0) = \kappa$, so that

$$\Gamma_\kappa = \omega_\kappa(\kappa) \,. \qquad (7.28)$$

In the same way one can define for such a scan a representative value α for the parameter ε^{*2}, that is,

$$\alpha = \frac{m}{8\hbar^2 E_i}\left(\frac{\hbar\,\Gamma_\kappa}{\kappa}\right)^2 \,. \qquad (7.29)$$

b. Inelasticity corrections to κ and ν. The use of the quasielastic approximation to determine the correlation range κ from two-crystal measurements gives rise to a systematic error $\delta\kappa/\kappa$ as a result of inelasticity. It is important, however, to note that the relative error $\delta\nu/\nu$ in the determination of ν over a range $d\kappa$, is related to *the change* $d(\delta\kappa/\kappa)$, in $\delta\kappa/\kappa$, through the relation $\delta\nu/\nu = d(\delta\kappa/\kappa)/d\ln\kappa$. Thus, the error in ν for a finite range of κ is given by

$$\frac{\delta\nu}{\nu} = \left(\frac{d(\delta\kappa/\kappa)}{d\ln\kappa}\right)_{av} \,. \qquad (7.30)$$

In order to estimate the magnitude of $\delta\kappa/\kappa$ (and therefore $\delta\nu/\nu$) we have used information on the dynamic correlation function $C_\kappa(\vec{q}, \omega)$ obtained from our three-crystal measurements. We put

$$C_\kappa(\vec{q}, \omega) \propto \frac{1}{(\kappa^2 + q^2)^{1-\eta/2}} \frac{\omega_\kappa(\vec{q})}{(\omega_\kappa(\vec{q}))^2 + \omega^2} \,, \qquad (7.31)$$

where $\omega_\kappa(\vec{q})$ is the experimentally determined q- and κ-dependent characteristic frequency (6.16), and calculate, for increasing values of κ, the two-crystal cross sections (7.3) for the experimental parameters used in our two-crystal experiment. Then, for each value of κ, a least-squares fit of the calculated "constant-angle" cross section, $(d\sigma/d\Omega)(q(0))$, is performed using the quasielastic expression $1/(\kappa'^2 + q^2(0))^{1-\eta/2}$ ($\eta = 0.055$) and a "best value" for κ' is determined. The error arising from the inelasticity ($\delta\kappa/\kappa = \kappa'/\kappa - 1$) is thus obtained. The result of the calculation described above is shown in Fig. 28, where the semilog plot of $\delta\kappa/\kappa$ vs κ corresponding to $E_i = 48.0$ meV, is represented by the full curve. The calculated error ranges from $+2.7\%$, at $\kappa = 2.45 \times 10^{-3}$ Å^{-1} ($T = 83.07$ °K), to $+12.5\%$ at $\kappa = 1.135 \times 10^{-1}$ Å^{-1} ($T = 93.02$). If we now apply Eq. (7.30), the resulting error in
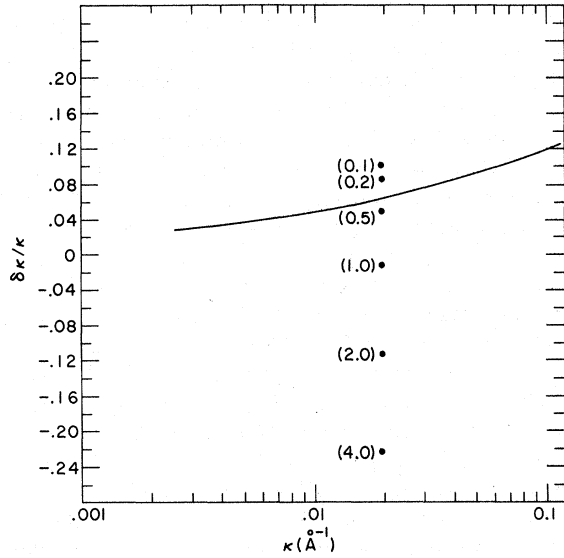
FIG. 28. Semilog plot of the calculated inelasticity correction $\delta\kappa/\kappa$ vs κ for $E_i = 48$ meV. Curve corresponds to the calculation carried out using the experimentally determined characteristic frequency function $d\kappa^E\Omega(q/\kappa)$. Points represent the results of model calculations for $\Omega(q/\kappa) = 1 + A(q/\kappa)^2$, for the indicated values of A. Each point is labelled by the corresponding A used in the calculation.

ν $(\delta\nu/\nu)$ over the given range of κ is 1.9%.

The function $\omega_\kappa(\vec{q})$ used in the above calculations is consistent with dynamic scaling, i.e., it is of the form $\omega_\kappa(0)\Omega(q/\kappa)$ and, as mentioned above, has been determined experimentally from our three-crystal measurements. We have also investigated the dependence of $\delta\kappa/\kappa$ on $\omega_\kappa(\vec{q})$ and have concluded that the inelasticity corrections depend critically on the specific function $\Omega(q/\kappa)$ applicable to the material. As an illustration of the effect of changing $\Omega(q/\kappa)$, we show in Fig. 28 results of calculations using functions of the form $1 + (q/\kappa)^2 A$ for various values of A. Note that while a function of this form is expected to provide a good representation of the characteristic frequency in the hydrodynamic region, it turns out that, with $A = 0.45$, it represents the experimental frequencies in RbMnF$_3$ very well up to $q/\kappa \approx 4$. Calculations such as these indicate clearly that adequate knowledge of $\Omega(q/\kappa)$, either experimental or theoretical, must be available in order to obtain reliable inelasticity corrections.

4. Two-Crystal Method for Minimizing Errors in ν Arising from Inelasticity

Equation (7.29) defines a parameter α that must be small compared to 1 in order for the quasielastic approximation to hold in a two-crystal measurement of κ. We now show that, if static and dynamic scaling are applicable to the material, then, under

very weak conditions, the dependence of the inelasticity correction $\delta\kappa/\kappa$ on Γ_κ, E_i, and κ is *all* contained in α; namely,

$$\frac{\delta\kappa}{\kappa} = \frac{\delta\kappa}{\kappa}(\alpha). \qquad (7.32)$$

We assume first that contributions to the cross section that are of second-order in $\hbar\omega/kT$ can be neglected[31] and secondly that, among the "static" conditions (7.5), only the requirement $\vec{q}(\omega) \approx \vec{q}(0)$ is not met. The two-crystal cross section (7.3) can then be taken to be

$$\frac{d\sigma}{d\Omega}(q(0)) \approx \text{const} \times \int d\omega\, C_\kappa(\vec{q}(\omega),\, \omega)$$

$$= \text{const} \times \int d\omega\, C_\kappa(\vec{q}(\omega))\frac{1}{\omega_\kappa(\vec{q}(\omega))}\, f_{q/\kappa}\left(\frac{\omega}{\omega_\kappa(\vec{q}(\omega))}\right). \qquad (7.33)$$

Making use of the static- and dynamic-scaling relations

$$C_\kappa(\vec{q}) = \kappa^y g(q/\kappa) \qquad (7.34a)$$

and

$$\omega_\kappa(\vec{q}) = \omega_\kappa(0)\,\Omega(q/\kappa) = \Gamma_\kappa \Omega(q/\kappa)/\Omega(1), \qquad (7.34b)$$

and introducing the dimensionless variables

$$\bar{q} = q/\kappa \qquad (7.35a)$$

and

$$\bar{\omega} = \omega/\Gamma_\kappa, \qquad (7.35b)$$

we obtain

$$\frac{d\sigma}{d\Omega}(\vec{q}(0))$$

$$\approx \text{const} \times \int d\bar{\omega}\, g(\bar{q}(\omega))\, \frac{1}{\Omega(\bar{q}(\omega))}\, f_{\bar{q}(\omega)}\left(\frac{\bar{\omega}\Omega(1)}{\Omega(\bar{q}(\omega))}\right), \qquad (7.36)$$

where κ^y has been absorbed in the constant. Following the sign conventions for $q(0)$ introduced in Sec. VII A 2, we have

$$(q(\omega))^2 = q(0)^2 + (k_I - k_F(\omega))^2 - 2\cos\theta_B\, q(0)\,(k_I - k_F(\omega)). \qquad (7.37)$$

If we now substitute for $k_I - k_F(\omega)$ its expansion to first order given by Eq. (7.2), we obtain

$$(q(\omega))^2 = q(0)^2 + \tfrac{1}{2}\omega^2\, m/E_i - \cos\theta_B\, q(0)\,\omega(2m/E_i)^{1/2}. \qquad (7.38)$$

Finally, switching to the dimensionless variables (7.35), we find

$$\bar{q}(\omega)^2 = \bar{q}(0)^2 + 4\alpha\bar{\omega}^2 - 4\cos\theta_B\, \bar{q}(0)\,\bar{\omega}\,(\alpha)^{1/2}, \qquad (7.39)$$

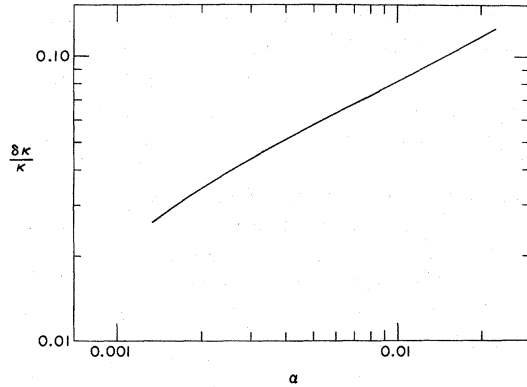where the expression (7.29) for α has been introduced. Equation (7.36) together with (7.39) gives

FIG. 29. Log-log plot of the inelasticity correction $\delta\kappa/\kappa$ vs $\alpha = (m/8\hbar^2 E_i)(\hbar\Gamma_\kappa/\kappa)^2$.

the two-crystal cross section. If the effect of the variation of $\cos\theta_B$ is neglected (and this is the third and final assumption in the present derivation), then the two-crystal cross section depends only on α. The quasielastic approximation to this cross section is given by $g(\vec{q}(0))$ and thus the difference between the two expressions, as well as the difference between the values of κ derived from them, depend on α alone. This is just the result contained in Eq. (7.32). Let us illustrate the dependence of $\delta\kappa/\kappa$ on the parameter α in the case of RbMnF$_3$. This function can be evaluated explicitly owing to the fact that the functions Ω and g have been experimentally determined. In the calculations which follow we have made none of the three approximations mentioned above. Thus $\delta\kappa/\kappa$ was evaluated following exactly the same procedures used to obtain the plot in Fig. 28, with E_i fixed at 48.0 meV, and α was obtained from κ using the definition (7.29) and the characteristic frequency function (6.16). A log-log plot of $\delta\kappa/\kappa$ vs α is shown in Fig. 29 and corresponds to the range of κ represented in Fig. 28. This diagram provides the inelasticity correction to κ, not only in RbMnF$_3$, but in all closely related systems, for example, MnF$_2$ in which a similar $\Omega(q/\kappa)$ is expected to apply.

The relation (7.32) implies that if, as the temperature (i. e., κ) is varied, the parameter α is maintained approximately constant, the *change* in $\delta\kappa/\kappa$, and therefore $\delta\nu/\nu$, can be made zero or minimal. This can be accomplished by suitably varying the incoming neutron energy E_i as a function of κ. A specific prescription for this variation, based on the dynamic scaling relationship $\Gamma_\kappa \propto \kappa^E$ is given by $\alpha = \text{const} \times \kappa^{2(E-1)}/E_i$. With this scaling assumption, the "constant-α" procedure thus provides a correct evaluation of ν in a two-crystal experiment in spite of the inelastic nature of the critical scattering and even in the absence of preliminary three-crystal data.

Again, let us illustrate the above procedure for the case of RbMnF$_3$. The lower limit of the range of κ covered in our two-crystal experiment is equal to 2.45×10^{-3} Å^{-1} (Fig. 28). In the actual measurement E_i was 48.0 meV, and this corresponds to $\alpha = 0.00134$. We could have chosen, for example, to set E_i equal to 6.6 meV which gives $\alpha = 0.00975$, and as κ increased, to increase E_i so as to keep α constant up to say $E_i = 87.1$ meV corresponding to $\kappa = 0.08$ Å^{-1}. In such a hypothetical "constant-α" experiment, $\delta\kappa/\kappa$ would be expected, on the basis of the plot in Fig. 29 and if Eq. (7.32) held exactly, to be a constant and equal to 7.5%. The dashed horizontal line in Fig. 30 represents this "ideal" case which would give $\delta\nu/\nu = 0$. The solid line in Fig. 30 represents the actual $\delta\kappa/\kappa$-vs-κ dependence calculated without introducing the three approximations on which Eq. (7.32) is based. Comparison of these two curves gives a measure of how effectively, in our practical example, Eq. (7.32) can be used and the "constant-α" procedure applied. In particular, by applying Eq. (7.30) we find that the inelasticity correction $\delta\nu/\nu$ associated with the "constant-α" procedure is down to 0.45%, in comparison to the 2.4% value associated with the constant E_i procedure over the same range [see dotted curve in Fig. (30)].

B. Case of Finite Resolution

1. *General*

a. Formulation of the quasielastic approximation for finite resolution. In the case of perfect resolution, the observed intensity is given by Eq. (7.3), which simply adds up all the contributions to the scattering coming from the different possible energy transfers; namely,

$$I = \text{const} \times \int d\omega \, \frac{d^2\sigma}{d\Omega \, d\omega} \, (\vec{q}(\omega), \omega). \qquad (7.40)$$
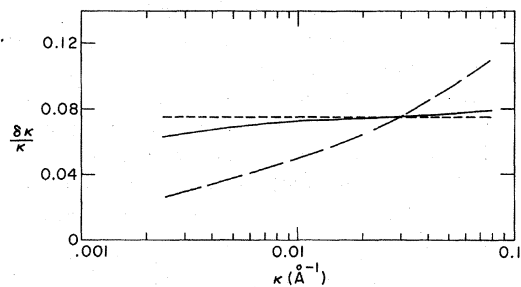

FIG. 30. Semilog plot of the correction $\delta\kappa/\kappa$ vs κ for the hypothetical experiment at constant α described in the text (solid line) and for the actual experiment at constant E_i (long-dashed line). Short-dashed horizontal line corresponds to the case of an "ideal" experiment at constant α.

The formulation of the quasielastic approximation is then contained in Eq. (7.4):

$$\int d\omega \; \frac{d^2\sigma}{d\Omega \, d\omega} \; (\vec{q}(\omega), \, \omega) \approx \text{const} \times C_\kappa(\vec{q}(0)). \quad (7.41)$$

However, in any real experiment, the observed intensity is given by a more complex integration than Eq. (7.40) (see Appendix for a general treatment of inelastic scattering in the two-crystal experiment). One must take into account that, for a general energy transfer $\hbar\omega$, the experimental arrangement allows not only the momentum transfer $\vec{k}_I - \vec{k}_F(\omega)$, but a spread of momentum transfers in $\vec{Q}$ space around the most probable one. The detection efficiency over the above region is described by the "inelastic two-crystal resolution function" $R(x, y, z, \omega)$ [Eq. (A9)] in terms of a set of coordinates (x, y, z) which, for given ω, defines the vector separation of a point in $\vec{Q}$ space from the position where the detection efficiency is maximum. Hence, the total observed intensity is obtained by summing up the scattering cross sections associated with the different scattering events, each one weighted with the proper value of the detection efficiency; namely, [Eq. (A8)],

$$I = \text{const} \times \int dx \, dy \, dz \, d\omega \, R(x, y, z, \omega)$$

$$\times \frac{d^2\sigma}{d\Omega \, d\omega} \; (\vec{q}_o(\omega) + x\hat{i}_F + y\hat{j}_F + z\hat{l}_F, \, \omega) \, , \quad (7.42)$$

where $\vec{q}_o(\omega) = \vec{k}_I - \vec{k}_F(\omega) - 2\pi\vec{\tau}$ is the most probable $\vec{q}$ associated with energy transfer $\hbar\omega$ and $(\hat{i}_F, \, \hat{j}_F, \, \hat{l}_F)$ is a set of orthogonal axes with origin at $\vec{q}_o(\omega)$ (Fig. 32). The quasielastic approximation for finite resolution, on the other hand, can be formulated as a convolution of the static correlation function with the elastic resolution function only; that is,

$$I \approx \text{const} \times \int dx_e \, dy_e \, dz_e$$

$$\times R(x_e, y_e, z_e, 0) \, C_\kappa(\vec{q}_o(0) + x_e \hat{i}_F + y_e \hat{j}_F + z_e \hat{l}_F) \, , $$
$$(7.43)$$

where the subscript e indicates that coordinates are referred to the axis system with origin at $\vec{q}_o(0)$, the nominal instrumental setting for elastic scattering.

We now examine the conditions under which the exact expression (7.42) can be replaced by the approximation (7.43). In the Appendix, we have derived an "elastic resolution function" approximation to Eq. (7.42). This result is expressed in terms of line integrals of the form

$$\int d\omega \; \frac{d^2\sigma}{d\Omega \, d\omega} \; (\vec{q}_o(0) + \Delta \vec{q}_e + (k_i - k_f) \hat{i}_f \, (\Delta\vec{q}_e, \, k_i, \, \delta_1), \, \omega) \, .$$

Figure 33 shows the integration path in reciprocal space associated with a general integral of this type. The vector $\hat{i}_f$ is the direction of the path and $\vec{q}_o(0) + \Delta \vec{q}_e$ is the point on the path where $k_f \equiv (k_i^2 - 2m\omega/\hbar)^{1/2}$ is equal to k_i (i.e., $\omega = 0$). We find that if

$$\int d\omega \frac{d^2\sigma}{d\Omega \, d\omega} \; (\vec{q}_o(0) + \Delta \vec{q}_e + (k_i - k_f) \hat{i}_f (\Delta\vec{q}_e, \, k_i, \, \delta_1), \, \omega) \; \approx \int d\omega \frac{d^2\sigma}{d\Omega \, d\omega} \; (\vec{q}_o(0) + \Delta\vec{q}_e + [k_I - k_F(\omega)] \hat{i}_f (\Delta\vec{q}_e, \, k_I, \, 0), \, \omega) \, ,$$
$$(7.44)$$

then Eq. (7.42) becomes [Eq. (A27)]

$$I \approx \int dx_e \, dy_e \, dz_e \, R(x_e, y_e, z_e, 0) \int d\omega \; \frac{d^2\sigma}{d\Omega \, d\omega} \; (\vec{q}_o(0) + \Delta\vec{q}_e + [k_I - k_F(\omega)] \hat{i}_f (\Delta\vec{q}_e, \, k_I, \, 0), \, \omega) \, . \quad (7.45)$$

Finally, in order to obtain (7.43) from (7.45), one must require in addition that

$$\int d\omega \; \frac{d^2\sigma}{d\Omega \, d\omega} \; (\vec{q}_o(0) + \Delta\vec{q}_e + [k_I - k_F(\omega)] \hat{i}_f (\Delta\vec{q}_e, \, k_I, \, 0), \, \omega) \approx C_\kappa(\vec{q}_o(0) + \Delta\vec{q}_e) \, . \quad (7.46)$$

Combining (7.44) and (7.46) we can state *the conditions for the quasielastic approximation in the case of finite resolution* in compact form:

$$\frac{d\sigma}{d\Omega} \, (\vec{q}_o(0) + \Delta\vec{q}_e, \, k_i, \, \delta_1) = \int d\omega \; \frac{d^2\sigma}{d\Omega \, d\omega} \; (\vec{q}_o(0) + \Delta\vec{q}_e + (k_i - k_f) \hat{i}_f(\Delta\vec{q}_e, \, k_i, \, \delta_1), \, \omega) \approx C_\kappa(\vec{q}_o(0) + \Delta\vec{q}_e) \, . \quad (7.47)$$

Equation (7.47) is the generalization of Eq. (7.4) to the case of finite resolution.

   b. *Practical method for applying "elastic resolution function" approximation to inelastic analysis of two-crystal data.* The intensity can in principle be calculated exactly from Eq. (7.42) in terms of $d^2\sigma/d\Omega \, d\omega$, by using the inelastic resolution function $R(x, y, z, \omega)$ derived in the Appendix. This is a formidable computational problem since the convolution requires that the resolution function be calculated at each point of $\vec{Q}$-ω space. Considerable simplification can be achieved by invoking the

"elastic resolution function" approximation (7.45) since only the $\omega = 0$ resolution function is required and this can generally be obtained directly from experiment. In spite of this simplification, however, Eq. (7.45) requires that for each point $\Delta\vec{q}_e$ in the elastic resolution volume, a *different* line integral $(d\sigma/d\Omega)(\vec{q}_o(0)+\Delta\vec{q}_e, k_I, 0)$ be calculated. A significant saving of computer time can be realized using a further approximation which relates the general line integral to the integral along the most probable path, but which is nevertheless still far weaker than the quasielastic approximation represented by (7.47). The approximation is the following:

$$\frac{d\sigma}{d\Omega}(\vec{q}_o(0)+\Delta\vec{q}_e, k_I, 0)\bigg/\frac{d\sigma}{d\Omega}(\vec{q}_o(0), k_I, 0)$$

$$\approx C_\kappa(\vec{q}_o(0)+\Delta\vec{q}_e)/C_\kappa(\vec{q}_o(0)), \quad (7.48)$$

that is, the ratio of the line integrals is approximately equal to the ratio of the quasielastic approximations to these integrals. A necessary and sufficient condition for (7.48) to hold is that the *change* in the quasielastic error over the elastic resolution volume be small compared to unity. To see this, let us introduce the notation $\sigma(\Delta\vec{q}_e)$ for the line integral $(d\sigma/d\Omega)(\vec{q}_o(0)+\Delta\vec{q}_e, k_I, 0)$ and $C(\Delta\vec{q}_e)$ for

the static correlation function $C_\kappa(\vec{q}_o(0)+\Delta\vec{q}_e)$. Equation (7.48) becomes

$$\frac{\sigma(\Delta\vec{q}_e)}{\sigma(0)} \approx \frac{C(\Delta\vec{q}_e)}{C(0)}. \quad (7.48')$$

Let us write

$$\sigma(\Delta\vec{q}_e) = C(\Delta\vec{q}_e)[1+(\delta\sigma/\sigma)(\Delta\vec{q}_e)], \quad (7.49a)$$

$$\sigma(0) = C(0)[1+(\delta\sigma/\sigma)(0)], \quad (7.49b)$$

where $\delta\sigma/\sigma$ represents the error introduced by the quasielastic approximation. Dividing (7.49a) by (7.49b), we obtain

$$\frac{\sigma(\Delta\vec{q}_e)}{\sigma(0)} = \frac{C(\Delta\vec{q}_e)}{C(0)}\left[1+d\left(\frac{\delta\sigma}{\sigma}(\Delta\vec{q}_e)\right)+\cdots\right],$$

where $d(\delta\sigma/\sigma)$ is the change in the quasielastic error over the resolution volume. Thus, Eq. (7.48) is equivalent to the condition

$$d(\delta\sigma/\sigma) \ll 1. \quad (7.50)$$

This condition is inherently less stringent than that for the quasielastic approximation itself and therefore one would expect the approximation (7.48) to have wide applicability. Inserting (7.48) in the intensity expression (7.45) leads to the final result

$$I(\vec{q}_o(0)) \approx \text{const} \times \frac{d\sigma}{d\Omega}(\vec{q}_o(0), k_I, 0)\int dx_e\, dy_e\, dz_e\, R(x_e, y_e, z_e, 0)\, C_\kappa(\vec{q}_o(0)+\Delta\vec{q}_e)/C_\kappa(\vec{q}_o(0)). \quad (7.51)$$

This formula provides a practical method for carrying out the inelastic analysis of two-crystal data. Note that $(d\sigma/d\Omega)(\vec{q}_o(0), k_I, 0)$ is identical with the line integral $(d\sigma/d\Omega)(q(0))$ defined for the case of perfect resolution in (7.3). Thus, Eq. (7.51) can be looked upon as a perfect-resolution intensity, corrected for the effect of finite resolution. The correction factor is the ratio of the quasielastic intensity expressions for finite and perfect resolution. An application of this method is presented in Sec. VII B 2.

2. Inelastic Analysis of Two-Crystal Data for RbMnF$_3$ in Region II $(q \gg \kappa)$

In Sec. IV A, we have described several determinations of the parameter η of the static correlation function, and have quoted results of an inelastic analysis of "Néel-temperature intermediate-q" data. This inelastic analysis was based on Eq. (7.51) and is described in detail in the present section. It is applied to data obtained in region II, where two-crystal measurements are most sensitive to η, and where the energy dependence of the scattering is known from three-crystal experiments.

The data were taken at $T = 83.055$ and with an in-

coming neutron energy equal to 48 meV. In the three-crystal experiment described in Sec. VI B, we have measured the differential scattering cross section $d^2\sigma/d\Omega\, d\omega$ under the conditions

$$q \gg \kappa, \quad (7.52a)$$

$$q \ll q_{ZB}, \quad (7.52b)$$

where q_{ZB} is the magnetic zone boundary which, for the (111) direction, is 0.64 Å^{-1}. This determination of the cross section does not distinguish between values of η in the range 0–0.1 because of the limited accuracy of three-crystal data, so the measured $d^2\sigma/d\Omega\, d\omega$ can be considered to contain η as an unknown parameter within that range. Using $d^2\sigma/d\Omega\, d\omega$, we can now compute the line integrals $(d\sigma/d\Omega)(\vec{q}_o(0))$ in Eq. (7.51) as a function of η. In order to satisfy condition (7.52b) over the range of these integrations, we limit the maximum value of $|q_o(0)|$ in this experiment to that obtained for line integrals of this type in Sec. VII A 2, where we investigated their convergence for the particular value of $\eta = 0.055$, and set a conservative upper limit for $|q_o(0)|$ of 0.076 Å^{-1}. The lower limit to $|q_o(0)|$ was set, in accord with (7.52a), as 0.018 Å^{-1}, which is approximately 10κ at this tempera-
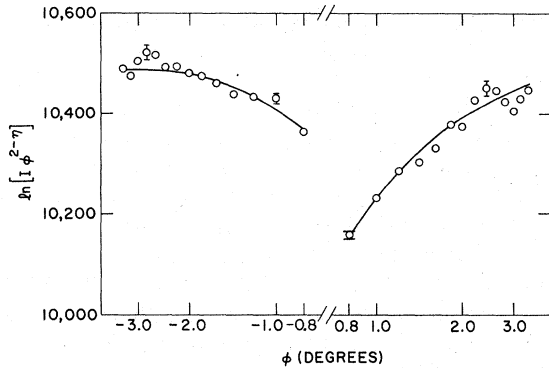
FIG. 31. Plot of $\ln(I\phi^{2-\eta})$ vs ϕ ($\eta = 0.044$). I is the total intensity and ϕ is the misset angle of the sample from the Bragg scattering position. ϕ scales are logarithmic. Solid curve is the result of a least-squares fit to the experimental points carried out using the practical method for inelastic analysis of two-crystal data discussed in the text (Eq. 7.51); the resulting value of η is 0.044. Note the asymmetry of the data. This asymmetry, as one can see, is fully reproduced by the calculated intensity curve obtained by means of the *experimentally* determined elastic resolution function.

ture. Thus, for the combined range $-0.076 < q_o(0) < -0.018$ Å^{-1}, $0.018 < q_o(0) < 0.076$ Å^{-1} we compute, in terms of η, the two-crystal intensity pattern (7.51) and perform a least-squares fit with η as a free parameter. The result of the fit is shown in Fig. 31, where the range of angles corresponds to the range of $q_o(0)$ indicated above. The best value is $\eta = 0.044 \pm 0.008$.

A conventional quasielastic fit of the same data has also been performed, giving $\eta = 0.060 \pm 0.008$. We conclude therefore that inelasticity causes an overestimation of the value of η determined in the quasielastic approximation. This conclusion is consistent with the result of direct inspection of Fig. 27. Here it is evident that if one tries to "fit" $(d\sigma/d\Omega)(\pm|q_o(0)|)$, for $|q_o(0)| < 0.076$ Å^{-1}, with a single quasielastic curve $|q_o(0)|^{\eta-2}$, with η as a free parameter, one will obtain a value of η greater than that which was originally fed into the calculation of $d\sigma/d\Omega$.

Finally we would like to point out that the data in Fig. 31 provide a rather direct determination of η. In the general case, κ and the background must also be determined, together with η, in order to fit the raw data. Unfortunately, these quantities are strongly correlated with η and therefore contribute additional uncertainty to the determination of its value. However, in the measurements we have just described, we see that (a) since $q \gg \kappa$, κ does not play any role (actually, we have verified that leaving κ as a free parameter does not alter the result); and (b) since we are essentially performing a small-q experiment ($q \ll q_{ZB}$), the intensities are

so high with respect to the background that it too does not play any role. (In fact, the background has been estimated to be of the order of 30 counts on the scale of Fig. 31.) Thus, the only free parameters used in the above fits were η, the zero shift, and the normalization factor.

APPENDIX: INELASTIC SCATTERING IN TWO-CRYSTAL EXPERIMENT

A. Definition of Two-Crystal Inelastic Resolution Function

Figure 32 is a diagram of the scattering geome-
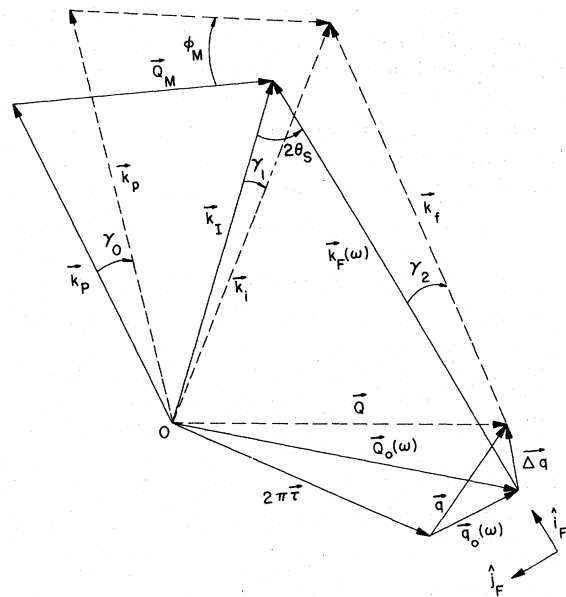
FIG. 32. Vector diagram in reciprocal space for a two-crystal inelastic scattering experiment. Figure shows processes involving a definite energy transfer $\hbar\omega$ from the sample to the neutrons. Vectors drawn with a dashed line represent a general event while the ones drawn with a full line represent the most probable process. $\vec{k}_P$ is the most probable wave vector in the in-Pile collimator, $\vec{k}_I$ the most probable wave vector in the monochromator to sample collimator, and $\vec{Q}_M$ the most probable scattering vector for the Bragg reflection in the monochromator; furthermore $\hat{i}_F$ is the optimum direction in the sample-to-detector collimator and $\hat{j}_F$ a direction orthogonal to it. We define $\vec{k}_F(\omega) = \hat{i}_F(k_I^2 - 2m\omega/\hbar)^{1/2}$. $\vec{Q}_o(\omega) = \vec{k}_I - \vec{k}_F(\omega)$ is the most probable among the wave vector transfers occurring in the sample with energy change $\hbar\omega$. Each k vector labelled with a lower-case subscript refers to a general process and its meaning is identical with the one defined above for the corresponding vector labelled with a capital subscript.

try in reciprocal space for a two-crystal scattering experiment in the neighborhood of the reciprocal lattice point $2\pi\vec{\tau}$. Neutrons passing through the in-Pile collimator (collimator 0) are scattered first from a monochromator (scattering angle $2\theta_M$); then, after passing through the monochromator-to-sample collimator (collimator 1), they are scattered through an angle $2\theta_S$ by the sample into the sample-to-detector collimator (collimator 2). $\vec{k}_p$, $\vec{k}_i$, and $\vec{k}_f$ are in-Pile, incident-on-sample, and final wave vectors, respectively, in a general scattering process. $\vec{k}_I$ is the most probable wave-vector incident on the sample and $\hat{i}_F$ is the optimum direction in collimator 2. γ_0, γ_1, and γ_2 are the horizontal divergence angles with respect to the

optimum directions in collimators 0, 1, and 2; δ_0, δ_1, and δ_2 are the corresponding vertical ones. In addition, we define $\Delta k_i = k_i - k_I$. $\vec{Q}_M$ is the most probable scattering vector for the Bragg reflection from the monochromator; ϕ_M and ϕ_M' measure the horizontal and vertical divergence angles, respectively, of the general scattering vector with respect to the optimum direction. Let $P_0(\gamma_0)$, $P_1(\gamma_1)$, $P_2(\gamma_2)$ be the horizontal transmission functions for the three collimators, and $P_0'(\delta_0)$, $P_1'(\delta_1)$, $P_2'(\delta_2)$ the corresponding vertical ones. Furthermore, let $P_M(\phi_M)$ and $P_M'(\phi_M')$ be the probability functions describing the horizontal and vertical mosaic spreads of the monochromator.[32] The total observed intensity is then given by

$$I = \int d\delta_0 \, dk_i \, d\delta_1 \, d\gamma_1 \, d\gamma_2 \, d\delta_2 \, dk_f \, (1/2 \sin\theta_M) \, P_0'(\delta_0) \, P_M' \, (k_I(\delta_1 - \delta_0)/Q_M) P_1'(\delta_1) P_2'(\delta_2) \, P_M((\Delta k_i/k_I) \tan\theta_M + \gamma_1)$$

$$\times P_0(2(\Delta k_i/k_I) \tan\theta_M + \gamma_1) P_1(\gamma_1) P_2(\gamma_2) \, (d\sigma/d\gamma_2 \, d\delta_2 \, dk_f) \, (\vec{k}_i - \vec{k}_f - 2\pi\vec{\tau}, \, (k_i^2 - k_f^2) \hbar^2/2m, \, k_i, \, \delta_1) \, , \qquad (A1)$$

where $d\sigma/d\gamma_2 \, d\delta_2 \, dk_f$ is the inelastic scattering cross section which is defined in terms of $d^2\sigma/\hbar d\Omega d\omega$ by the relation

$$\frac{d\sigma}{d\gamma_2 \, d\delta_2 \, dk_f} = -\frac{\hbar k_f}{m} \frac{d^2\sigma}{d\Omega \, d\omega} \, . \qquad (A2)$$

In order to define the resolution function we now introduce a new set of variables. If $\hbar\omega$ is the energy transfer $(\hbar^2/2m)(k_i^2 - k_f^2)$, we define the vector function $\vec{k}_F(\omega) = \hat{i}_F(k_I^2 - 2m\omega/\hbar)^{1/2}$ which is the most probable final wave vector for processes involving an energy transfer equal to $\hbar\omega$. Then, defining the wave-vector transfer in the sample as $\vec{Q} \equiv \vec{q} + 2\pi\vec{\tau} \equiv \vec{k}_i - \vec{k}_f$, the vector function $\vec{Q}_o(\omega) \equiv \vec{q}_o(\omega) + 2\pi\vec{\tau} \equiv \vec{k}_I - \vec{k}_F(\omega)$ will be the most probable wave-vector transfer associated with an energy transfer $\hbar\omega$. Let us put $\Delta\vec{q} = \vec{q} - \vec{q}_o(\omega)$ and consider the components of $\Delta\vec{q}$ with respect to the two horizontal axes $\hat{i}_F$ and $\hat{j}_F$, as well as the vertical axis $\hat{l}_F$.[33] We define x, y, and z by $\Delta\vec{q} \equiv x\hat{i}_F + y\hat{j}_F + z\hat{l}_F$. We now change variables in the integrand of Eq. (A1), from the set $(\delta_0, k_i, \delta_1, \gamma_1, \gamma_2, \delta_2, k_f)$ to the set $(\delta_0, k_i, \delta_1, x, y, z, \omega)$. If $\gamma_1, \gamma_2, \delta_1, \delta_2$ are small angles, so that contributions of order higher than the first can be neglected, then the equations which

transform one set into the other are

$$x = -\gamma_1 k_i \sin 2\theta_S + \Delta k_i \cos 2\theta_S - k_f(k_i, \omega) + k_F(\omega) \, ,$$

$$y = -\gamma_1 k_i \cos 2\theta_S - \Delta k_i \sin 2\theta_S + k_f(k_i, \omega)\gamma_2 \, ,$$

$$z = k_i \delta_1 - k_f(k_i, \omega) \delta_2 \, , \qquad (A3)$$

where

$$k_f(k_i, \omega) = (k_i^2 - 2m\omega/\hbar)^{1/2} \, .$$

Assume the inelasticities in the scattering to be small enough to satisfy the condition

$$\frac{2\Delta k_i}{k_I} \left(\frac{k_I}{k_F(\omega)}\right)^2 \ll 1 \, , \qquad (A4)$$

thus implying that $\Delta k_i/k_I \ll 1$ and allowing the substitution $k_F - k_f \approx -\Delta k_i \, k_I/k_F$. Then Eqs. (A3) become

$$x = -\gamma_1 k_I \sin 2\theta_S - \Delta k_i [k_I/k_F(\omega) - \cos 2\theta_S] \, ,$$

$$y = -\gamma_1 k_I \cos 2\theta_S - \Delta k_i \sin 2\theta_S + k_F(\omega)\gamma_2 \, , \qquad (A3')$$

$$z = k_I \delta_1 - k_F(\omega) \delta_2 \, .$$

Solving with respect to γ_1, γ_2, δ_2, we obtain

$$\gamma_1 = \{ -x - \Delta k_i [k_I/k_F(\omega) - \cos 2\theta_S] \}/k_I \sin 2\theta_S \equiv f_1(\Delta k_i, x, \omega) \, , \qquad (A5a)$$

$$\gamma_2 = \frac{y + \Delta k_i \sin 2\theta_S}{k_F(\omega)} + \frac{\cot 2\theta_S}{k_F(\omega)} \{ -x - \Delta k_i [k_I/k_F(\omega) - \cos 2\theta_S] \}$$

$$= [y - \cot(2\theta_S) x]/k_F(\omega) + [\Delta k_i/k_F(\omega)]\{\sin 2\theta_S - \cot 2\theta_S [k_I/k_F(\omega) - \cos 2\theta_S]\} \equiv f_2(\Delta k_i, x, y, \omega) \, , \qquad (A5b)$$

$$\delta_2 = (-z + k_I \delta_1)/k_F(\omega) \equiv f_2'(\delta_1, z, \omega) \, . \qquad (A5c)$$

Finally, if we put

$$(\Delta k_i/k_I)\tan\theta_M + f_1(\Delta k_i, x, \omega) \equiv f_M(\Delta k_i, x, \omega) \, , \qquad (A5d)$$

$$2(\Delta k_i/k_I)\tan\theta_M + f_1(\Delta k_i, x, \omega) \equiv f_0(\Delta k_i, x, \omega) , \qquad (A5e)$$

changing variables in the integrand of Eq. (A1) gives

$$I \propto \int d\delta_0\, dk_i\, d\delta_1\, dx\, dy\, dz\, d\omega\, (1/k_I \sin\theta_M \sin(2\theta_S)k_F^3(\omega))\, P_0'(\delta_0)\, P_M'(k_I(\delta_1 - \delta_0)/Q_M)\, P_1'(\delta_1)\, P_2'(f_2'(\delta_1, z, \omega))$$

$$\times P_M\big(f_M(\Delta k_i, x, \omega)\big)P_0\big(f_0(\Delta k_i, x, \omega)\big)P_1\big(f_1(\Delta k_i, x, \omega)\big)P_2\big(f_2(\Delta k_i, x, y, \omega)\big)\,(d\sigma/d\gamma_2\, d\delta_2\, dk_f)\,(\vec{q}_0(\omega) + \Delta\vec{q},\, \omega,\, k_i,\, \delta_1) .$$
$$(A6)$$

Now, if the cross section satisfies the condition

$$\frac{d\sigma}{d\gamma_2\, d\delta_2\, dk_f}\,(\vec{q},\, \omega,\, k_i,\, \delta_1) \approx \frac{d\sigma}{d\gamma_2\, d\delta_2\, dk_f}\,(\vec{q},\, \omega,\, k_I,\, 0) ,$$
$$(A7)$$

then, with the definition

$$\frac{d\sigma}{d\gamma_2\, d\delta_2\, dk_f}\,(\vec{q},\, \omega) \equiv \frac{d\sigma}{d\gamma_2\, d\delta_2\, dk_f}\,(\vec{q},\, \omega,\, k_I,\, 0) ,$$

Eq. (A6) becomes

$$I \propto \int dx\, dy\, dz\, d\omega$$

$$\times R(x, y, z, \omega)\,\frac{d^2\sigma}{d\Omega\, d\omega}\,(\vec{q}_0(\omega) + x\hat{i}_F + y\hat{j}_F + z\hat{l}_F,\, \omega) ,$$
$$(A8)$$

where we have used the relation (A2) and have defined the resolution function by

$$R(x, y, z, \omega) = \int d\delta_0\, dk_i\, d\delta_1\,\frac{1}{k_I \sin\theta_M \sin(2\theta_S)k_F^2(\omega)}\,P_0'(\delta_0)\, P_M'\big(k_I(\delta_1 - \delta_0)/Q_M\big)P_1'(\delta_1)$$

$$\times P_2'\big(f_2'(\delta_1, z, \omega)\big)P_M\big(f_M(\Delta k_i, x, \omega)\big)P_0\big(f_0(\Delta k_i, x, \omega)\big)\, P_1\big(f_1(\Delta k_i, x, \omega)\big)P_2\big(f_2(\Delta k_i, x, y, \omega)\big) .\ (A9)$$

The resolution function $R(x, y, z, \omega)$ represents the detection efficiency at a definite position in $\vec{Q}$-ω space. The set (x, y, z) gives the vector separation from the position of maximum detection efficiency for events occurring with the same energy transfer $\hbar\omega$.

B. Evaluation of Two-Crystal Inelastic Resolution Function

In order to evaluate the resolution function defined in Eq. (A9) we assume a Gaussian form for the probability distributions P_0, P_1, P_2, P_0', P_1', P_2', P_M, and P_M'; that is,

$$P_0(\gamma_0) \propto \exp[-\tfrac{1}{2}(\gamma_0/\alpha_0)^2] ,$$

$$P_0'(\delta_0) \propto \exp[-\tfrac{1}{2}(\delta_0/\alpha_0')^2] ,$$

$$P_1(\gamma_1) \propto \exp[-\tfrac{1}{2}(\gamma_1/\alpha_1)^2] ,$$

$$P_1'(\delta_1) \propto \exp[-\tfrac{1}{2}(\delta_1/\alpha_1')^2] ,$$

$$P_2(\gamma_2) \propto \exp[-\tfrac{1}{2}(\gamma_2/\alpha_2)^2] ,$$

$$P_2'(\delta_2) \propto \exp[-\tfrac{1}{2}(\delta_2/\alpha_2')^2] ,$$

$$P_M(\phi_M) \propto \exp[-\tfrac{1}{2}(\phi_M/\eta_M)^2] ,$$

$$P_M(\phi_M') \propto \exp[-\tfrac{1}{2}(\phi_M'/\eta_M')^2] . \qquad (A10)$$

The first six equations above define the characteristic horizontal and vertical angles, α_0, α_1, α_2 and α_0', α_1', α_2', of the corresponding collimators; the last two equations define the horizontal (η_M) and vertical (η_M') mosaic spread parameters of the monochromator. Substitution of Eqs. (A10) into Eq. (A9) gives, after integration over δ_0,

$$R(x, y, z, \omega) \propto C\int dk_i\, d\delta_1\,\frac{1}{k_I \sin(2\theta_S)k_F^2(\omega)}\,\exp\left\{-\frac{1}{2}\left[\left(\frac{f_M(\Delta k_i, x, \omega)}{\eta_M}\right)^2\right.\right.$$

$$\left.\left.+\left(\frac{f_0(\Delta k_i, x, \omega)}{\alpha_0}\right)^2 + \left(\frac{f_1(\Delta k_i, x, \omega)}{\alpha_1}\right)^2 + \left(\frac{f_2(\Delta k_i, x, y, \omega)}{\alpha_2}\right)^2 + \left(\frac{\delta_1^2}{4\,\eta_M'^2\sin^2\theta_M + \alpha_0'^2}\right) + \frac{\delta_1^2}{\alpha_1'^2} + \left(\frac{f_2'(\delta_1, z, \omega)}{\alpha_2'}\right)^2\right]\right\} ,$$
$$(A9')$$

where

$$C = \frac{1}{\sin\theta_M}\left(\frac{1}{\alpha_0'^2} + \frac{1}{4\,\eta_M'^2\sin^2\theta_M}\right)^{-1/2} . \qquad (A11)$$

The resolution function can be split into two factors, a horizontal one and a vertical one; namely,

$$R(x, y, z, \omega) = R_H(x, y, \omega) R_V(z, \omega) , \tag{A12}$$

where

$R_H(x, y, \omega)$

$$\propto \int dk_i \frac{1}{k_I \sin(2\theta'_S) k_F(\omega)} \exp\left\{-\frac{1}{2}\left[\left(\frac{f_M(\Delta k_i, x, \omega)}{\eta_M}\right)^2 + \left(\frac{f_0(\Delta k_i, x, \omega)}{\alpha_0}\right)^2 + \left(\frac{f_1(\Delta k_i, x, \omega)}{\alpha_1}\right)^2 + \left(\frac{f_2(\Delta k_i, x, y, \omega)}{\alpha_2}\right)^2\right]\right\} \tag{A13a}$$

and

$$R_V(z, \omega) \propto C \int d\delta_1 \frac{1}{k_F(\omega)} \exp\left\{-\frac{1}{2}\left[\frac{\delta_1^2}{4\eta_M'^2 \sin^2\theta_M + \alpha_0'^2} + \frac{\delta_1^2}{\alpha_1'^2} + \left(\frac{f_2'(\delta_1, z, \omega)}{\alpha_2'}\right)^2\right]\right\} . \tag{A13b}$$

Let us evaluate the horizontal term first. According to Eqs. (A5), the functions f_M, f_0, f_1, and f_2 are homogeneous and linear in x, y, and Δk_i; that is,

$$f_M(\Delta k_i, x, \omega) = \alpha_{M1}(\omega)\Delta k_i + \alpha_{M2} x , \tag{A14a}$$

$$f_0(\Delta k_i, x, \omega) = \alpha_{01}(\omega)\Delta k_i + \alpha_{02} x , \tag{A14b}$$

$$f_1(\Delta k_i, x, \omega) = \alpha_{11}(\omega)\Delta k_i + \alpha_{12} x , \tag{A14c}$$

$$f_2(\Delta k_i, x, y, \omega) = \alpha_{21}(\omega)\Delta k_i + \alpha_{22} x + \alpha_{23}(\omega) y , \tag{A14d}$$

where

$\alpha_{M1}(\omega)$

$$= \tan\theta_M/k_I - (1/k_I \sin2\theta_S)[k_I/k_F(\omega) - \cos2\theta_S] ,$$

$\alpha_{M2} = \alpha_{02} = \alpha_{12} = -1/k_I \sin2\theta_S ,$

$\alpha_{01}(\omega)$

$$= 2\tan\theta_M/k_I - (1/k_I \sin2\theta_S)[k_I/k_F(\omega) - \cos2\theta_S] ,$$

$$\alpha_{11}(\omega) = -(1/k_I \sin2\theta_S)[k_I/k_F(\omega) - \cos2\theta_S] ,$$

$\alpha_{21}(\omega)$

$$= [1/k_F(\omega)]\{\sin2\theta_S - \cot2\theta_S[k_I/k_F(\omega) - \cos2\theta_S]\} ,$$

$$\alpha_{22}(\omega) = -\cot2\theta_S/k_F(\omega) ,$$

$$\alpha_{23}(\omega) = 1/k_F(\omega) . \tag{A15}$$

If we substitute Eqs. (A14) into Eq. (A13a) we obtain

$$R_H(x, y, \omega) \propto \frac{1}{k_I \sin(2\theta_S)k_F(\omega)} \int dk_i \exp\left\{-1/2[\Delta k_i^2 L(\omega) + \Delta k_i M(x, y, \omega) + N(x, y, \omega)]\right\} , \tag{A16}$$

where

$$L(\omega) = \alpha_{M1}^2(\omega)/\eta_M^2 + \alpha_{01}^2(\omega)/\alpha_0^2 + \alpha_{11}^2(\omega)/\alpha_1^2 + \alpha_{21}^2(\omega)/\alpha_2^2 ,$$

$$M(x, y, \omega) = [2\alpha_{M1}(\omega)\alpha_{M2}/\eta_M^2 + 2\alpha_{01}(\omega)\alpha_{M2}/\alpha_0^2 + 2\alpha_{11}(\omega)\alpha_{M2}/\alpha_1^2 + 2\alpha_{21}(\omega)\alpha_{22}(\omega)/\alpha_2^2] x + [2\alpha_{21}(\omega)\alpha_{23}(\omega)/\alpha_2^2] y ,$$

$$N(x, y, \omega) = \alpha_{M2}^2(1/\eta_M^2 + 1/\alpha_0^2 + 1/\alpha_1^2) x^2 + (1/\alpha_2^2)[\alpha_{22}(\omega) x + \alpha_{23}(\omega) y]^2 . \tag{A17}$$

Finally, integration of Eq. (A16) gives

$$R_H(x, y, \omega) \propto \frac{1}{k_I \sin(2\theta_S) k_F(\omega)[L(\omega)]^{1/2}} \exp\left[-\frac{1}{2}\left(N(x, y, \omega) - \frac{M^2(x, y, \omega)}{4L(\omega)}\right)\right] . \tag{A18}$$

Let us now evaluate the vertical term $R_V(z, \omega)$. If we substitute Eq. (A5c) into Eq. (A13b) we obtain

$$R_V(z, \omega) \propto C \int d\delta_1 \frac{1}{k_F(\omega)} \exp\left\{-\frac{1}{2}[\delta_1^2 L'(\omega) + \delta_1 M'(z, \omega) + N'(z, \omega)]\right\} , \tag{A19}$$

where

$$L'(\omega) = \frac{1}{4\eta_M'^2 \sin\theta_M + \alpha_0'^2} + \frac{1}{\alpha_1'^2} + \frac{1}{\alpha_2'^2}\left(\frac{k_I}{k_F(\omega)}\right)^2 ,$$

$$M'(z, \omega) = -2zk_I/\alpha_2'^2 k_F(\omega) ,$$

$$N'(z, \omega) = z^2/\alpha_2'^2 k_F^2(\omega) . \tag{A20}$$

Integration of Eq. (A19) gives

$$R_V(z, \omega) \propto \frac{C}{k_F(\omega)[L'(\omega)]^{1/2}}$$

$$\times \exp\left[-\frac{1}{2}\left(N'(z, \omega) - \frac{M'^2(z, \omega)}{4L'(\omega)}\right)\right] . \quad (A21)$$

The complete inelastic resolution function is given by (A12) using (A18) and (A21). It is a hypersurface in $\vec{Q}$-ω space whose constant-ω sections are ellipsoids in x, y, and z.

C. "Elastic Resolution Function" Approximation

Equation (A8) permits the calculation of the expected intensity pattern in the general case in which inelastic scattering is observed with a two-crystal arrangement. Such a calculation makes use of the assumption of a Gaussian mosaic spread for the monochromator and Gaussian transmission functions for the three collimators. We now derive, dropping the Gaussian assumption, and retaining only the symmetry properties of the probability functions, a simplified form of Eq. (A8) which, under certain conditions, will allow the intensity to be expressed in terms of the elastic resolution function, which can be measured directly.

Let us consider Eq. (A3) for the case of elastic scattering, that is, ω equal to zero, thus defining three functions of k_i, δ_1, γ_1, γ_2, δ_2 which we shall call x_e, y_e, and z_e, given by

$$x_e = -\gamma_1 k_i \sin 2\theta_S + \Delta k_i(\cos 2\theta_S - 1) ,$$

$$y_e = \gamma_1 k_i \cos 2\theta_S - \Delta k_i \sin 2\theta_S + k_i \gamma_2 , \quad (A22)$$

$$z_e = k_i(\delta_1 - \delta_2) .$$

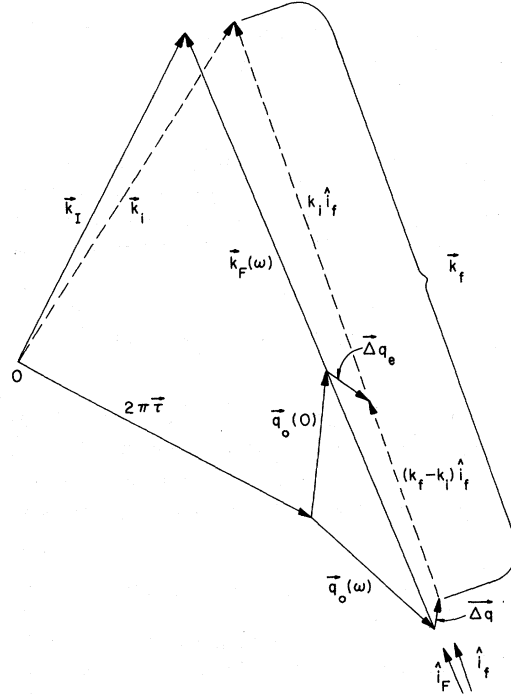We now change variables, in the integrand of Eq.

FIG. 33. Representation of the integration path in reciprocal space associated with a general energy integral of the type defined in Eq. (A23). Vector $\hat{i}_f$ is the direction of the path and $\vec{q}_o(0) + \Delta\vec{q}_e$ is the point on the path where $k_f = k_i$ (i.e., $\omega = 0$). From the figure one sees that $\vec{q}_o(\omega) + \Delta\vec{q} = \vec{q}_o(0) + \Delta\vec{q}_e + (k_i - k_f)\hat{i}_f$.

(A1) from the set $(\delta_0, k_i, \delta_1, \gamma_1, \gamma_2, \delta_2, k_f)$ to the set $(\delta_0, k_i, \delta_1, x_e, y_e, z_e, \omega)$ and obtain, using (A7),

$$I \propto \int d\delta_0 \, dk_i \, d\delta_1 \, dx_e \, dy_e \, dz_e \, \frac{1}{k_I^3 \sin\theta_M \sin(2\theta_S)} \, P_0'(\delta_0) \, P_M'\big(k_I(\delta_1 - \delta_0)/Q_M\big) P_1'(\delta_1) \, P_2'\big(f_2'(\delta_1, z_e, 0)\big) P_M\big(f_M(\Delta k_i, x_e, 0)\big)$$

$$\times P_0\big(f_0(\Delta k_i, x_e, 0)\big) P_1\big(f_1(\Delta k_i, x_e, 0)\big) P_2\big(f_2(\Delta k_i, x_e, y_e, 0)\big) \int d\omega \, \frac{d^2\sigma}{d\Omega \, d\omega} \big(\vec{q}_o(\omega) + \Delta\vec{q}, \omega\big) , \quad (A23)$$

where $\Delta\vec{q}$ is, of course, a definite function of k_i, δ_1, x_e, y_e, z_e, ω whose components are

$$x = x_e + \Delta k_i + k_F(\omega) - k_f(k_i, \omega) ,$$

$$y = [k_f(k_i, \omega)/k_i] \, y_e$$
$$- [k_f(k_i, \omega)/k_i - 1] \, (x_e \cot 2\theta_S - \Delta k_i \tan\theta_S) ,$$

$$z = [k_f(k_i, \omega)/k_i] \, z_e - [k_f(k_i, \omega) - k_i] \, \delta_1 . \quad (A24)$$

These equations, taken together with $\vec{q}_o(\omega)$, describe parametrically, as a function of ω, the path in reciprocal space over which the integral with respect

to energy is to be performed. This path is a straight line that, for $\omega = 0$, passes through the point $\vec{q}_o(0) + \Delta\vec{q}_e$ (where $\Delta\vec{q}_e \equiv x_e \hat{i}_F + y_e \hat{j}_F + z_e \hat{l}_F$) in a direction $\hat{i}_f(\Delta\vec{q}_e, k_i, \delta_1)$ (see Fig. 33). Δk_i and δ_1 cause $\hat{i}_f$ to deviate from the value corresponding to $\Delta k_i = \delta_1 = 0$ by an amount $(\Delta\gamma_2, \Delta\delta_2)$ which can be obtained from Eqs. (A22), giving

$$\Delta\gamma_2 = \tan(\theta_S)\Delta k_i/k_i ,$$
$$\Delta\delta_2 = \delta_1 . \quad (A25)$$

We now assume that this dependence of the integration path on Δk_i and δ_1 can be neglected, so that

$$\int d\omega \, \frac{d^2\sigma}{d\Omega \, d\omega} \, (\vec{q}_o(0) + \Delta\vec{q}_e + (k_i - k_f)\,\hat{i}_f(\Delta\vec{q}_e, k_i, \delta_1), \omega) \approx \int d\omega \, \frac{d^2\sigma}{d\Omega \, d\omega} \, (\vec{q}_o(0) + \Delta\vec{q}_e + [k_I - k_F(\omega)]\,\hat{i}_f(\Delta\vec{q}_e, k_I, 0), \omega) \, .$$

$$(A26)$$

Here we have used the relation $\vec{q}_o(\omega) + \Delta\vec{q} = \vec{q}_o(0) + \Delta\vec{q}_e + (k_i - k_f)\,\hat{i}_f$ (Fig. 33). [Note that in the case in which the quasielastic approximation holds, in the sense defined by Eq. (7.4), the condition (A26)

is satisfied automatically since both integrals are given by $C_\kappa(\vec{q}_o(0) + \Delta\vec{q}_e)$.] Finally, if we consider Eq. (A23) and remove the dependence of the energy integral on k_i and δ_1 by means of (A26), we obtain

$$I \propto \int dx_e \, dy_e \, dz_e \, R(x_e, y_e, z_e, 0) \int d\omega \, \frac{d^2\sigma}{d\Omega \, d\omega} \, (\vec{q}_o(0) + \Delta\vec{q}_e + [k_I - k_F(\omega)]\,\hat{i}_f(\Delta\vec{q}_e, k_I, 0), \omega) \, , \qquad (A27)$$

where we have applied Eq. (A9), with ω set equal to zero, to define the *elastic* resolution function. The vector $\hat{i}_f$, which gives the direction of the path in reciprocal space over which the energy integration

is performed, can be obtained directly from Eqs. (A22) by setting Δk_i and δ_1 equal to zero. We shall refer to Eq. (A27) as the "elastic resolution function" approximation.

---

†Work performed under the auspices of the U.S. Atomic Energy Commission.

*Present address: CSN Casaccia CNEN Rome, Italy.

‡Present address: Centre d'Etudes Nucleaires, Grenoble, France.

[1]M. J. Cooper and R. Nathans, Acta Cryst. **23**, 357 (1967); **A24**, 481 (1968); **A24**, 619 (1968).

[2]S. J. Pickart, H. A. Alperin, and R. Nathans, J. Phys. **25**, 565 (1964).

[3]D. T. Teaney, V. L. Moruzzi, and B. E. Argyle, J. Appl. Phys. **37**, 1122 (1966).

[4]C. G. Windsor and R. W. H. Stevenson, Proc. Phys. Soc. (London) **87**, 501 (1966).

[5]D. T. Teaney, M. J. Freiser, and R. W. H. Stevenson, Phys. Rev. Letters **9**, 212 (1962).

[6]R. Nathans, F. Menzinger, and S. J. Pickart, J. Appl. Phys. **39**, 1237 (1968).

[7]L. Van Hove, Phys. Rev. **95**, 1374 (1954); J. Als-Nielsen, O. W. Dietrich, W. Marshall, and P. A. Lindgård, Solid State Commun. **5**, 607 (1967).

[8]See, for example, W. Marshall, in *Critical Phenomena*, edited by M. S. Green and J. V. Sengers (U. S. GPO, Washington, D. C., 1966).

[9]H. Y. Lau, L. M. Corliss, A. Delapalme, J. M. Hastings, R. Nathans, and A. Tucciarone, Phys. Rev. Letters **23**, 1225 (1969); J. Appl. Phys. **41**, 1384 (1970).

[10]B. I. Halperin and P. C. Hohenberg, Phys. Rev. **177**, 952 (1969). See also R. A. Ferrell, N. Menyhard, H. Schmidt, F. Schwabl, and P. Szepfalusy, Phys. Rev. Letters **18**, 891 (1967); Ann. Phys. (N. Y.) **47**, 565 (1968).

[11]P. Résibois and C. Piette, Phys. Rev. Letters **24**, 514 (1970).

[12]D. L. Huber and D. A. Krueger, Phys. Rev. Letters **24**, 111 (1970).

[13]M. E. Fisher and R. J. Burford, Phys. Rev. **156**, 583 (1967).

[14]D. Jasnow and M. Wortis, Phys. Rev. **176**, 739 (1968).

[15]We are indebted to D. Cox and J. Hurst of Brookhaven National Laboratory for carrying out the plastic deformation.

[16]D. R. Beaucage, M. A. Kelley, D. Ophir, S. Rankowitz, R. J. Spinrad, and R. van Norton, Nucl. Instr.

Methods **40**, 26 (1966).

[17]B. O. Loopstra, Nucl. Instr. Methods **44**, 181 (1966).

[18]Center for Materials Science and Engineering, Massachusetts Institute of Technology, Cambridge, Mass.

[19]Designed by R. L. Chase, Brookhaven National Laboratory.

[20]See, for example, O. W. Dietrich and J. Als-Nielsen, in *Critical Phenomena*, edited by M. S. Green and J. V. Sengers (U. S. GPO, Washington, D. C., 1966).

[21]Cooper and Nathans have chosen the opposite convention for $\vec{Q}$, namely, $\vec{Q} = \vec{k}_f - \vec{k}_i$. Note that in spite of the change in definition, *with the present choice of axes X_n* the expressions given by these authors for M_{kl} remain formally unchanged, both for the two-crystal elastic case and for the three-crystal case.

[22]M. J. Cooper, Acta Cryst. **A24**, 624 (1968).

[23]V. L. Sailor, H. L. Foote, Jr., H. H. Landon, and R. E. Wood, Rev. Sci. Instr. **27**, 26 (1956).

[24]The reason for making the high-q measurements on the minus side is that the next (111) reflection is farther away when rotating the sample in the negative direction than when the rotation is made in the opposite direction [see Fig. 3(b)].

[25]We are indebted to B. Dorner for pointing out that the expression for P_0 given in Ref. 1 is in error and must be multiplied by the factor $1/(4\sin\theta_M \sin\theta_A)$. This point will be discussed in a forthcoming publication by Dorner.

[26]We use $\vec{q}$ and κ in place of $\vec{k}$ and ξ^{-1} for wave-vector and inverse-range parameter in order to conform to usage in neutron scattering. The superscript A, indicating the operator to which the correlation function refers, will henceforth be omitted for simplicity; in the present paper this operator is always the staggered magnetization. It is to be noted, also, that $\hbar$ has been set equal to unity throughout.

[27]$C_k(\vec{q}, \omega)$ can be related to the Fourier transform $S(\vec{q}, \omega)$ of the unsymmetrized pair-correlation function appearing in Eq. (2.1) by the expression $S(\vec{q}, \omega) = 2C_k(\vec{q}, \omega)/(1 + e^{-\hbar\omega/kT})$ [L. P. Kadanoff and P. C. Martin, Ann. Phys. (N. Y.) **24**, 419 (1963)].

[28]B. I. Halperin and P. C. Hohenberg, Phys. Rev. **188**, 398 (1969).

[29]M. De Leener and P. Résibois, Phys. Rev. **178**, 819

(1969).

[30]M. Helm, Phys. Letters 33A, 513 (1970).

[31]It has been shown in the discussion of the "q-averaging" mechanism in Sec. VII A 2 that the first-order term in $\hbar\omega/kT$ does not contribute to the average of $(d\sigma/d\Omega)$ $(+|q(0)|)$ and $(d\sigma/d\Omega)$ $(-|q(0)|)$, and is therefore omitted here.

[32]In this Appendix we use a notation which is a natural extension of that employed in Ref. 1 for the *elastic* two-crystal case.

[33]We adopt the convention that $\hat{i}_F$, $\hat{j}_F$, and $\hat{l}_F$ form a right-handed system and that positive rotations of the angles δ_n give rise to positive components along $\hat{l}_F$.